

**POLITECNICO DI MILANO**

Polo Regionale di Lecco

Facoltà di Ingegneria Industriale

Master of Science in  
Mechanical Engineering



Testing and optimization of the tunable damping system for  
vibration control of a space devoted instrument

Relatore: Prof. Bortolino SAGGIN

Co-relatore: Ing. Diego SCACCABAROZZI

Master thesis of:

Can ÖZER  
Matr. 722899

Anno Accademico 2009 - 2010

# Acknowledgements

*I owe my deepest gratitude to Prof Saggin and Diego; this thesis would not have been possible without them.*

*Furthermore it is a great pleasure to thank everyone in the Measurements Lab especially Marco (thanks for all the support!!) and Gerardo.*

*Special thanks to,*

*my wonderful, ever caring brother, Ceyhun,*

*my loving mother and father,*

*all my friends and family. Together we've been "there and back again"*

# Abstract

In this work the testing and the optimization of the vibration damping system designed for a space application is performed. The damping system consists of three versatile and adjustable dampers whose main objective is to control the vibrations transmitted to the Mars Infrared MApper (MIMA) through its mounting interface during its launch and landing on Mars surface. This is essential in order to assure the survival of the main instrument parts and especially of the brittle optics, which has to overcome a random loading with an RMS acceleration of  $150 \text{ m/s}^2$  in a frequency range encompassing the main structure resonances.

The environmental conditions have been simulated through shaker tests on a single individual damper to characterize its dynamic properties and finally achieving its optimal tuning. Further shaker tests were performed on an inertially equivalent mockup of the instrument with the aim to investigate the performance of the full dampers system and predict the instrument transmitted vibrations. Alongside the experimental procedures, a computational model of the test setup is also established and this model is validated with feedback from the mockup tests at the expected vibration levels. Finally an optimized damper configuration is conceived by minimization of the transmissibility in the frequency regions of “dangerous random” evaluated on the instrument optics.

**Keywords:** damping, vibration control, Finite Element methods

## Sommario

Lo scopo del presente lavoro è la sperimentazione e l'ottimizzazione di un sistema di smorzamento per impiego spaziale. Il sistema consiste di tre "damper" con l'obiettivo di controllare i livelli di eccitazione trasmessi allo spettrometro MIMA, durante le fasi di lancio e di atterraggio su Marte. Tale sistema deve garantire il superamento degli elevati livelli di accelerazione attesi per la missione, in particolare, le ottiche dello strumento devono superare senza danneggiamento, un'eccitazione di tipo "random" che interessa un ampio intervallo di frequenze e il cui valore RMS è pari a  $150 \text{ m/s}^2$ .

I livelli di eccitazione previsti per la missione sono stati simulati utilizzando un eccitatore elettrodinamico e i parametri dinamici di ogni singolo damper sono stati definiti ed ottimizzati. La progettazione di un modello dinamico equivalente dello strumento ha reso possibile l'analisi delle prestazioni dei dampers attraverso la valutazione delle vibrazioni trasmesse allo strumento. Parallelamente all'attività sperimentale, un modello ad elementi finiti del mockup dello strumento è stato sviluppato e validato in seguito al confronto con i risultati sperimentali ottenuti. La configurazione ottimale del sistema di smorzamento è stata quindi definita, minimizzando la trasmissibilità dell'eccitazione "random" nel campo di frequenze in cui risulta essere particolarmente gravosa per lo strumento.

**Parole chiave:** smorzamento, controllo delle vibrazioni, elementi finiti

<b>CHAPTER 1: INTRODUCTION</b>	<b>11</b>
<b>1.1 Mars Infrared Mapper (MIMA)</b>	<b>11</b>
<b>1.2 MIMA environmental conditions</b>	<b>12</b>
1.2.1 Sine Environment	13
1.2.2 Random environment	14
1.2.3 Pyroshocks	14
<b>1.3 The need for a vibration damping system</b>	<b>15</b>
<b>1.4 The dampers</b>	<b>18</b>
<b>1.5 Objectives</b>	<b>19</b>
<b>CHAPTER 2: DESIGN AND MANUFACTURING OF A DUMMY MODEL FOR TESTING</b>	<b>22</b>
<b>2.1 Necessity of a dummy model</b>	<b>22</b>
<b>2.2 Computer modeling of the prototype</b>	<b>22</b>
2.2.1 Part design	22
2.2.2 Assembly	23
<b>2.3 Modification of the dummy prototype to achieve an optimum model</b>	<b>25</b>
2.3.1 The problem and the requirements	25
2.3.2 The method of optimization	26
<b>2.4 Validity of the dummy model for testing purposes</b>	<b>28</b>
<b>CHAPTER 3: TUNING OF THE DAMPERS WITH ONE DEGREE-OF-FREEDOM TESTING</b>	<b>30</b>
<b>3.1 The need for damper tuning</b>	<b>30</b>
<b>3.2 Test methodology</b>	<b>30</b>
3.2.1 Experimental equipment	31
3.2.2 Experimental Modal Analysis techniques	36
3.2.3 Test setup	37
3.2.4 Vibration stimulus for the single degree-of-freedom tests	42
<b>3.3 Tuning of the dampers</b>	<b>43</b>
3.3.1 Objectives of the tuning procedure	43

3.3.2	Excitation amplitude and damper non-linearity	45
3.3.3	Damper response and tightening preload	47
3.3.4	Radial behavior of dampers	49
3.3.5	Damper Response Synchronization	51
3.3.6	Configurational modifications of damper assembly	54
<b>3.4</b>	<b>Dampers in their final tuning and configuration</b>	<b>58</b>
<b>3.5</b>	<b>Results and discussion</b>	<b>60</b>
	<b>CHAPTER 4: DAMPER PROPERTIES ESTIMATION</b>	<b>62</b>
<b>4.1</b>	<b>Excitation amplitude and linear modal parameters</b>	<b>62</b>
<b>4.2</b>	<b>Analytical formulation of the test setup</b>	<b>64</b>
<b>4.3</b>	<b>Estimating linear parameters from test data</b>	<b>66</b>
4.3.1	Modal parameters from resonance	66
4.3.2	Extracting modal parameters by curve fitting	70
<b>4.4</b>	<b>Estimating torsional properties from test data</b>	<b>74</b>
<b>4.5</b>	<b>Estimated properties of the final damper configuration</b>	<b>77</b>
4.5.1	Axial stiffness coefficient, $k_1$	77
4.5.2	Radial stiffness coefficients, $k_2$ & $k_3$	78
4.5.3	Rotational stiffness coefficient, $k_{\theta,1}$	78
4.5.4	Rotational stiffness coefficients $k_{\theta,2}$ & $k_{\theta,3}$	78
<b>4.6</b>	<b>Results &amp; Discussion</b>	<b>79</b>
	<b>CHAPTER 5: FINITE ELEMENT ANALYSIS OF THE DAMPER – MOCKUP SYSTEM</b>	<b>80</b>
<b>5.1</b>	<b>The need for a Finite Elements Analysis</b>	<b>80</b>
<b>5.2</b>	<b>Verification of the structural modes of the mockup using FEM</b>	<b>81</b>
5.2.1	Finite Element Modeling	81
5.2.2	Meshing	83
5.2.3	Results and discussion	84
<b>5.3</b>	<b>Analysis of the Damper-Mockup system using linear spring elements</b>	<b>87</b>
5.3.1	Modeling of the dampers as spring elements	87
5.3.2	Defining Virtual Spring stiffness coefficients	88

5.3.3 Resulting behavior of the system	89
5.3.4 Evaluation of the results for the ultimate damper configuration	94
<b>5.4 Results and discussion</b>	<b>95</b>
<b>CHAPTER 6: TESTING OF THE DUMMY MODEL</b>	<b>97</b>
<b>6.1 Test methodology</b>	<b>97</b>
6.1.1 Test setup	97
6.1.2 Reference stimulus	101
<b>6.2 Mockup testing and results</b>	<b>105</b>
6.2.1 Z axis testing	105
6.2.2 X axis testing	109
6.2.3 Y axis testing	112
<b>6.3 Evaluation of the damping system characteristics from the test results</b>	<b>115</b>
6.3.1 Performance in Z axis	115
6.3.2 Performance in X axis	116
6.3.3 Performance in Y axis	117
<b>6.4 Results and discussion</b>	<b>118</b>
<b>CHAPTER 7: FINITE ELEMENT METHODS FOR THE RESPONSE IMPROVEMENT OF THE DAMPERS</b>	<b>120</b>
<b>7.1 Introduction</b>	<b>120</b>
<b>7.2 Objectives of response improvement</b>	<b>121</b>
<b>7.3 Response improvement by modifying the axial spring properties of the dampers</b>	<b>122</b>
7.3.1 Initial damper tuning	122
7.3.2 Effects of individual dampers on the overall system response	123
7.3.3 Combination of different axial stiffnesses to achieve an optimum response (Opt 1)	124
<b>7.4 Response optimization of the system with theoretical dampers</b>	<b>126</b>
7.4.1 Effect of the radial stiffness coefficient	126
7.4.2 Effect of axial stiffness coefficient	127
7.4.3 Resulting modes of vibration of the optimal system (Opt 2)	128
<b>7.5 Performance comparison of the damper tunings using FE methods</b>	<b>129</b>
7.5.1 Method of performance assessment	129
7.5.2 Assessment of the test configuration	130

7.5.3 Assessment of the optimization performed through changing axial stiffnesses (Opt 1)	135
7.5.4 Assessment of the optimization performed through changing both the axial and the radial stiffnesses (Opt 2)	139
7.5.5 Performance comparison of the optimal damper tunings	144
<b>7.6 Results and discussion</b>	<b>145</b>
<b>CHAPTER 8: CONCLUSION AND FINAL REMARKS</b>	<b>147</b>
<b>REFERENCES</b>	<b>150</b>
<b>APPENDIX A</b>	<b>152</b>
<b>APPENDIX B</b>	<b>159</b>

# List of Figures

Figure 1-1: The Rover Module equipped with the MIMA	12
Figure 1-2: Positioning of the MIMA on the rover and the defined axis system	13
Figure 1-3: Weighing factor on the MIMA as a function of excitation frequency	15
Figure 1-4: FRF <sup>2</sup> profiles of <i>System 1</i> and <i>System 2</i>	16
Figure 1-5: Weighed FRF <sup>2</sup> profiles of <i>System 1</i> and <i>System 2</i>	17
Figure 1-6: Outside view of a tightly packed damper	19
Figure 1-7: The diagram representing the objectives of the study	21
Figure 2-1: Some of the components making up the model assembly	23
Figure 2-2: Exploded view of the model assembly	24
Figure 2-3: Dummy model created and assembled in CATIA	24
Figure 2-4: Local reference frame on the prototype	26
Figure 2-5: Modified final model of the MIMA	27
Figure 2-6 - Final up-to-date mockup to be tested	27
Figure 3-1: Dummy mass used for the single damper testing	32
Figure 3-2: Vibration generators (shakers) used in the tests performed	33
Figure 3-3: ENDEVCO 27A11 accelerometer used for vibration measurement	34
Figure 3-4: Data flow from the accelerometer to the PC	35
Figure 3-5: Data acquisition system	35
Figure 3-6: The basic Frequency Response Function used	36
Figure 3-7: The convention used for the directional parameters of the damper	37
Figure 3-8: Mechanical testing setup schematics for the single damper vertical direction	38
Figure 3-9: A fine measurement setup with four accelerometers	39
Figure 3-10: Mechanical testing setup schematics for the single damper radial direction	40
Figure 3-11: Accelerometer configuration used for the radial testing of the dampers.	41
Figure 3-12: A sample sweep sine with amplitude equal to 33g and increasing frequency	42
Figure 3-13: The critical sine and the random vibration environment	44
Figure 3-14: FRF comparison of the same damper response to a 0.5g sweep and a 5g sweep sine	45
Figure 3-15: FRF comparison of the same damper response to a 20g sweep and a 33g sweep sine	46
Figure 3-16: FRF comparison of the damper responses at different preloads.	48
Figure 3-17: Placement of the accelerometers on the mass for the transversal testing.	50
Figure 3-18: FRF of the three accelerometers versus the reference sweep sine	50
Figure 3-19: Comparison of the FRFs of the three fully closed dampers to a 20g sweep	52
Figure 3-20: The three dampers synchronized in terms of response.	53
Figure 3-21: Comparison of FRFs of the dampers in three different configurations.	55
Figure 3-22: Low level Resonance Search response of the damper in Config 2 and in Config 3.	56
Figure 3-23: Time-frequency plot for the damper channel in the testing of Config 2	57
Figure 3-24: Axial sweep sine test at 20g in the range 20-1000 Hz.	59

Figure 4-1: Formulation of a linear model	63
Figure 4-2: The actual damper-mass assembly	64
Figure 4-3: Identification of the natural frequency using the FRF from a sweep sine test at 5g.	67
Figure 4-4: FRF Magnitude and Phase plots comparison	69
Figure 4-5: FRF from 20g sweep sine test of a damper in Config 3.	70
Figure 4-6: Comparison of the mathematical and experimental FRF	72
Figure 4-7: The mathematical FRF fit with the adjusted modal parameters	73
Figure 4-8: The rotational motion at the tip of the damper.	75
Figure 4-9: Accelerometer configuration for an axial low level sweep sine test.	76
Figure 4-10: Low level sweep sine FRF in the region of the rotational resonance of the damper.	76
Figure 5-1: The CAD mockup assembled in CATIA.	81
Figure 5-2: Mockup CAD model with the necessary connections defined.	82
Figure 5-3: The model with fastened connection properties	83
Figure 5-4: The linear tetrahedron	83
Figure 5-5: A course mesh compared to a fine mesh.	84
Figure 5-6: Structural modes of vibration of the mockup	86
Figure 5-7: Spring Virtual Parts connected at three point on the mockup.	87
Figure 5-8: Clamped boundary condition for the spring elements.	88
Figure 5-9: Stiffness coefficients estimated from single degree of freedom tests	89
Figure 5-10: First three modes of vibration at (a) 131 Hz (b) 151 Hz (c) 264 Hz.	91
Figure 5-11: Displacement Vector plot of the vibration mode 1 at 131 Hz.	92
Figure 5-12: Displacement Vector plot of the vibration mode 2 at 151 Hz.	92
Figure 5-13: The axes of rotation for the first two modes of vibration.	93
Figure 5-14: Displacement Vector plot of the vibration mode 3 at 264 Hz.	94
Figure 5-15: Mockup COG position vs. Damper Triangle Moment Center.	95
Figure 6-1: The three testing directions shown on the mockup and damper designations.	98
Figure 6-2: Signal acquisition and feed schematics for the dummy model testing.	98
Figure 6-3: Z axis testing setup with the accelerometer positions.	99
Figure 6-4: X axis testing setup with the accelerometer positions.	100
Figure 6-5: Y axis testing setup with accelerometer positions.	101
Figure 6-6: Resonance search reference input profile plot.	102
Figure 6-7: Sweep sine reference input profile plot.	103
Figure 6-8: Random reference input profile plot.	104
Figure 6-9: Z axis sweep sine test time history.	106
Figure 6-10: Z axis FRFs	107
Figure 6-11: Z axis random test time history.	108
Figure 6-12: Z axis random FRF plot.	108
Figure 6-13: X axis sweep sine test time history.	109
Figure 6-14: X axis sweep sine FRF plot.	110
Figure 6-15: X axis random test time history.	111
Figure 6-16: X axis random FRF plot.	111
Figure 6-17: Y axis sweep sine test time history.	112
Figure 6-18: Y axis sweep sine FRF plot.	113
Figure 6-19: Y axis random test time history.	114

Figure 6-20: Y axis random FRF plot.	114
Figure 6-21: FRF Magnitude plot	116
Figure 6-22: FRF Magnitude plot for the Y axis testing	117
Figure 7-1: Damper name designation given.	121
Figure 7-2: Vibration mode shapes clockwise at (a) 101 Hz (b) 112 Hz (c) 175 Hz	128
Figure 7-3: Weighing profile plotted.	130
Figure 7-4: Evaluated FRF <sup>2</sup> profile for the three axes in X loading	131
Figure 7-5: Weighed FRF <sup>2</sup> profiles for X loading	131
Figure 7-6: FRF <sup>2</sup> profile for the three axes in Y loading	132
Figure 7-7: Weighed FRF <sup>2</sup> profiles for Y loading	133
Figure 7-8: Evaluated FRF <sup>2</sup> profile for the three axes in Z loading	134
Figure 7-9: Weighed FRF <sup>2</sup> profiles for Z loading	134
Figure 7-10: FRF <sup>2</sup> profile measured for the three axes in X loading	135
Figure 7-11: Weighed FRF <sup>2</sup> profile for X loading	136
Figure 7-12: FRF <sup>2</sup> profile measured for the three axes in Y loading	137
Figure 7-13: Weighed FRF <sup>2</sup> profile for Y loading	137
Figure 7-14: FRF <sup>2</sup> profile measured for the three axes in Z loading	138
Figure 7-15: Weighed FRF <sup>2</sup> profile for Z loading	139
Figure 7-16: FRF <sup>2</sup> profile measured for the three axes in X loading	140
Figure 7-17: Weighed FRF <sup>2</sup> profile for X loading	140
Figure 7-18: FRF <sup>2</sup> profile measured for the three axes in Y loading	141
Figure 7-19: Weighed FRF <sup>2</sup> profile for Y loading	142
Figure 7-20: FRF <sup>2</sup> profile measured for the three axes in Z loading	143
Figure 7-21: Weighed FRF <sup>2</sup> profile for Z loading	143
Figure B-1: Time history of out-of-plane vibrations for the Z sweep sine testing	159
Figure B-2: FRF of out-of-plane vibrations for the Z sweep sine testing	160
Figure B-3: Time history of out-of-plane vibrations for the Z random testing	161
Figure B-4: Time history of out-of-plane vibrations for the Z random testing	161

# List of tables

Table 1-1: Sine environment profile acting on the MIMA.	13
Table 1-2: Random environment plot	14
Table 1-3: Pyroshock profile	14
Table 2-1: Initial and desired properties of the model	25
Table 2-2: Properties of the final model versus those of the desired	28
Table 3-1: Comparison of damper modal parameters corresponding to different preloads	48
Table 3-2: Preload distances on the dampers	53
Table 4-1: Summary of the stiffness coefficients estimated for the final damper configuration.	79
Table 5-1: Comparison of the advantages and the disadvantages involved in experimental methods of a shaker test to those of Finite Elements methods.	80
Table 5-2: Summary of the results of the FEM analysis for the structural modes of the mockup.	85
Table 5-3: Natural frequencies of the system corresponding to the first three modes of vibration.	90
Table 6-1: Resonance search profile properties.	102
Table 6-2: Sweep sine excitation profile.	103
Table 6-3: Random reference excitation	104
Table 6-4: Experimental modes compared to those of the FEM analysis.	119
Table 7-1: Computed first three natural frequencies of the FE model	121
Table 7-2: Stiffness values estimated and used in the FE model	123
Table 7-3: Results of the various FE analysis runs with different damper properties.	124
Table 7-4: Systematic study of the effect of damper stiffnesses and the results	125
Table 7-5: Various analyses changing the radial stiffness and the results	127
Table 7-6: Various analyses changing the axial stiffness for a given radial stiffness	127
Table 7-7: Weighing profile to be multiplied by the FRF squared profile	129
Table 7-8: RMS values for the weighed FRF <sup>2</sup> profiles for the X loading condition	132
Table 7-9: RMS values for the weighed FRF <sup>2</sup> profiles for the Y loading condition	133
Table 7-10: RMS values for the weighed FRF <sup>2</sup> profiles for the Z loading condition	135
Table 7-11: RMS values for the weighed FRF <sup>2</sup> profiles for the X loading condition	136
Table 7-12: RMS values for the weighed FRF <sup>2</sup> profiles for the Y loading condition	138
Table 7-13: RMS values for the weighed FRF <sup>2</sup> profiles for the Z loading condition	139
Table 7-14: RMS values for the weighed FRF <sup>2</sup> profiles for the X loading condition	141
Table 7-15: RMS values for the weighed FRF <sup>2</sup> profiles for the Y loading condition	142
Table 7-16: RMS values for the weighed FRF <sup>2</sup> profiles for the Z loading condition	144
Table 7-17: Results of the performance assessment summarized	144
Table 7-18: Suggested optimum spring properties and the resulting modes of vibration.	146

# Chapter 1: Introduction

## 1.1 Mars Infrared Mapper (MIMA)

The Mars Infrared Mapper (MIMA) is a miniaturized FT-IR spectrometer which is being developed for the ESA ExoMars Pasteur mission. MIMA has been designed to provide remote measurements of mineralogy and atmosphere of the scene surrounding a Martian rover and guide it to key targets for detailed in site measurements by other rover experiments.<sup>[1]</sup> The MIMA is capable of measurements typically a few tens of meters away searching for evidence of water and of water-related processes like carbonates sulfates clay minerals and possibly, organics.<sup>[2]</sup>

The design is based on the scheme of the double pendulum with corner cubes which has been successfully implemented in similar instruments (PFS) designed and qualified for Mars Express and Venus Express.<sup>[3]</sup>

The Descent Module of the ExoMars mission will carry a 210 kg mobile Rover to the surface of Mars equipped with a drill, a sample preparation and distribution system (SPDS) and the 16.5 kg Pasteur Payload of remote-sensing, in-situ and analytical instruments, including the MIMA.<sup>[4]</sup>

The rover payload, PASTEUR, with its 12 instruments mounted on it, including the MIMA, is shown in Figure 1-1.

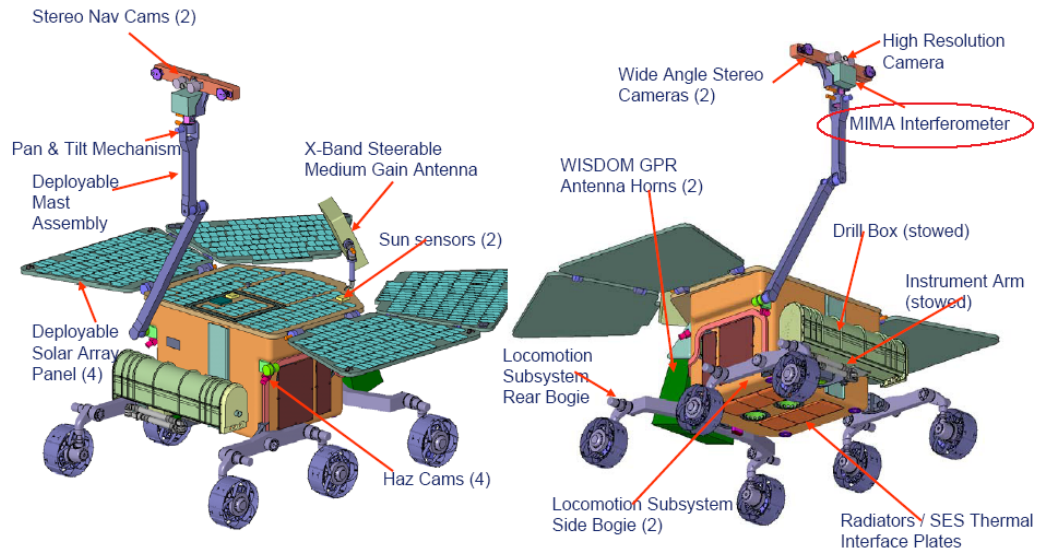


Figure 1-1: The Rover Module equipped with the MIMA designed for the ESA ExoMars Mission<sup>[5]</sup>

## 1.2 MIMA environmental conditions

The MIMA has to cope with several vibration environments acting during launch and landing. The instrument mounted on the rover with the given axis system notation is shown below in Figure 1-2.

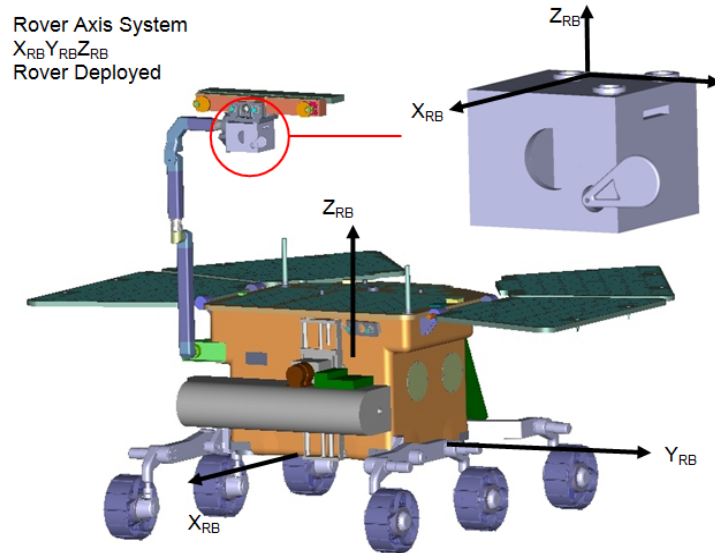


Figure 1-2: Positioning of the MIMA on the rover and the defined axis system (*source: MIMA testing documents*)

The mechanical excitations acting on the MIMA are identified as mainly the sine and the random vibration environment and the pyroshocks which are explained in detail in the following sections. [6]

### 1.2.1 Sine Environment

There is a specific sine profile acting on the MIMA during launch based on the defined axis system given as

Table 1-1: Sine environment profile acting on the MIMA.

Frequency [Hz]	Amplitude [g]	
	X, Y axes	Z axis
5	1	1
20	33	33
100	33	33

### 1.2.2 Random environment

The random vibrations acting on the MIMA are given in terms of Power Spectral Density (PSD) [ $\text{g}^2/\text{Hz}$ ] defined for different directions as

Table 1-2: Random environment plot

Frequency [Hz]	PSD [ $\text{g}^2/\text{Hz}$ ]	
	X, Y axes	Z axis
20	0.007	0.0174
100	0.1720	0.43
400	0.1720	0.43
2000	0.007	0.0174

### 1.2.3 Pyroshocks

Pyroshocks are the excitations generated by the explosive devices that allows the separation of different parts of assembly. The content of the excitation is commonly given as Shock Response Spectrum (SRS), the maximum of the decaying, oscillatory response of a structure to the high-amplitude and high frequency of the mechanical excitation. The frequencies that comprise this oscillatory response can extend to thousands of Hertz and beyond. They are a subset of the resonant frequencies of the structure. [7]

The pyroshock profile given in terms of Shock Response Spectrum (SRS) is shown in the table below

Table 1-3: Pyroshock profile

Frequency [Hz]	SRS [g]
100	25
300	400
2000	1500
10000	1500

### 1.3 The need for a vibration damping system

Having discussed the environmental conditions acting on the instrument, here the necessity of implementing a vibration damping system is addressed. The random environment that the MIMA is subjected to, acts within a wide frequency band resulting in dangerous excitations of the instrument resonances. The optics of the MIMA is the most critical part and it becomes even more vulnerable at high frequency excitations due to the presence of natural frequencies above 500 Hz. This phenomenon can be modeled using an appropriate weighing function for the dynamic response as shown in Figure 1-3.

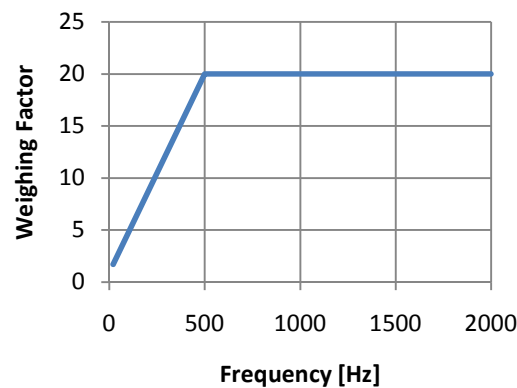


Figure 1-3: Weighing factor on the MIMA as a function of excitation frequency

This plot suggests that accelerations on the MIMA at frequencies above 500Hz are almost 20 times more effective than accelerations at lower frequency. The maximum gain is the typical amplification of low damped structures. To show the effect of such a function, a typical Frequency Response Function (FRF) of a simple first order system is considered.

Assuming two systems with the given natural frequencies

$$f_{0,1} = 150Hz$$

$$f_{0,2} = 250Hz$$

and identical damping ratio

$$\zeta = 0.3$$

The FRF of a first order system is given by the mathematical relation

$$H(j\omega) = \frac{\omega_0^2 + j2\omega\zeta\omega_0}{(\omega_0^2 - \omega^2) + j2\omega\zeta\omega_0}$$

And so the FRF squared profiles of these two systems can be plotted as (see Appendix A for the complete procedure)

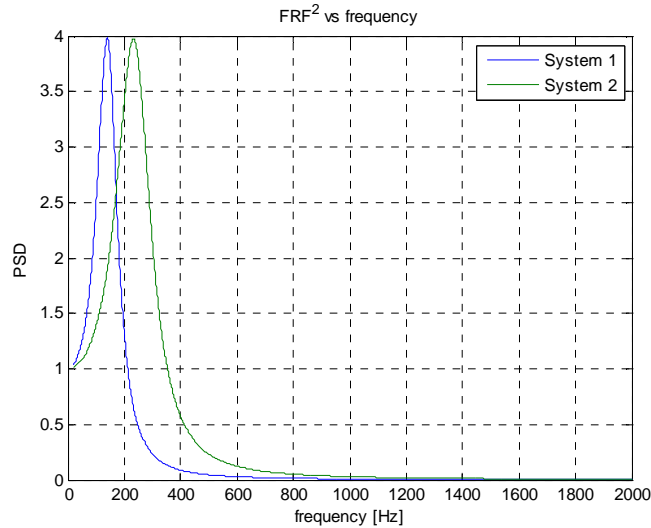


Figure 1-4: FRF<sup>2</sup> profiles of *System 1* and *System 2*

From this plot it can be observed that the FRF<sup>2</sup> profiles of the two described systems are only shifted in the frequency domain with respect to each other with more or less similar amplification trends.

However when the weighing function given in Figure 1-3 is applied to these profiles, the plot becomes

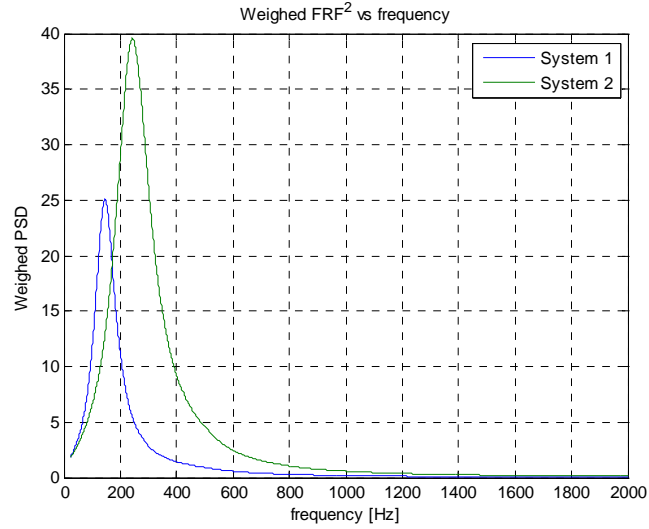


Figure 1-5: Weighed FRF<sup>2</sup> profiles of *System 1* and *System 2*

If a uniform Power Spectral Density [ $\text{m}^2\text{s}^{-4}\text{Hz}^{-1}$ ] is applied to the systems, the computed RMS values are given as

$$RMS_1 = 4.8 \text{ m}^2\text{s}^{-4}$$

$$RMS_2 = 9.7 \text{ m}^2\text{s}^{-4}$$

Clearly, now there is a significant difference between the behavior of these two systems when the conditions of the MIMA are considered. As the amplifications in the response are shifted to higher frequencies, their effect on the MIMA becomes even more dramatic. This conclusion emphasizes the necessity of implementing a damping system to optimize the resonances of the system to achieve a certain cutoff frequency, above which the amplifications of the response are dampened down to low levels, thereby protecting the MIMA optics from high frequency excitations.

## 1.4 The dampers

Due to the previously explained environmental conditions acting at MIMA-Rover interface, the necessity of a damping system arises in order to reduce the vibrations transmitted to the instrument internal components and mostly to the optical elements.

The dampers were developed and manufactured by the MIMA team with the help of the experience gained from the previous PFS dampers, which utilized a somewhat similar concept.

The damping elements are Silicon rubber O-rings, held in place and separated by plastic spacers. The principal elements housing the silicon and nylon rings are made of titanium to minimize the heat exchange between MIMA and the rover. There are basically three such titanium parts including an inner element supporting the rings from the inside. An outer element covers the periphery of the rings and a threaded element is used to tighten the ring assembly, packing them closer.

By acting on the threaded cap, the damper characteristics can be partially changed. Increasing the tightening of the cap, the ring elements are packed closer and closer, thereby resulting in an increase of the overall stiffness of the damper. On the other hand, loosening the tightening torque, the ring elements are relieved and a less stiff damper can be obtained. This is a great advantage since it allows the optimization of the damper behavior to meet the mechanical behavior objectives.

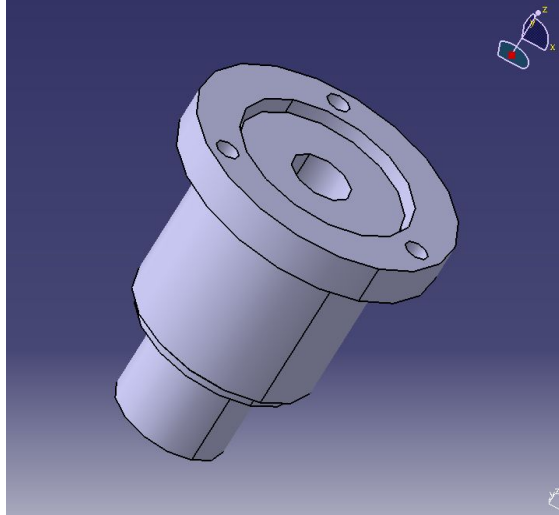


Figure 1-6: Outside view of a tightly packed damper

## 1.5 Objectives

The main objective of this study is to perform a complete analysis including the optimization and verification of the MIMA–Damper system in terms of mechanical vibrations it is subjected to, and to suggest further improvements regarding this matter. In this scope, a detailed work will be performed regarding:

- the modification and creation of the dummy model that is being used as a replacement for the actual instrument for experimental purposes. The modified model will account for the changes occurred recently in the MIMA and provide a satisfactory representation of the actual instrument. A computer model and several software tools will be used to obtain the modified dummy.

- the testing of the dampers individually on the shaker in a single degree of freedom setup in various orientations. The dampers will be tested and then tuned with respect to the dynamic response by changing the preload on them. Furthermore, the damper configuration may be modified by adding or subtracting certain components if the requirements cannot be met with only the preload change.
- the modeling of the dummy inertial equivalent with FEM software. The model should be consistent with the behavior of the dummy in the testing conditions. The dampers must be represented as proper elements having adjustable directional parameters like the actual components.
- testing of the dummy in order to visualize the frequency response of the actual dynamic system. Besides providing invaluable information about the actual behavior of the MIMA, the results of these tests will be used to check the accuracy of the Finite Elements model.
- identifying the changes in the tuning of the dampers allowing to achieve improvements of the dummy response, by using the parametric analysis with the Finite Elements model.
- testing of the dummy - if possible - with the optimally tuned dampers, verifying the behavior of the optimal system and thus validating the numerical analysis.

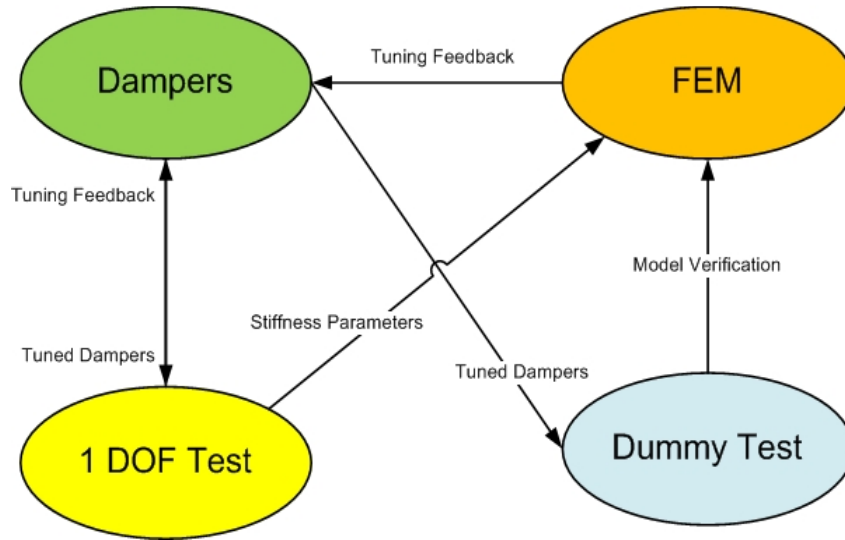


Figure 1-7: The diagram representing the objectives of the study

# **Chapter 2: Design and manufacturing of a dummy model for testing**

## **2.1 Necessity of a dummy model**

During the course of this work numerous tests will be performed, some of which are quite strong and potentially dangerous to the subject of the test. Therefore using the actual MIMA for all these testing purposes is out of question. This results in the necessity of an appropriate substitute that can be tested instead of the actual instrument.

In order to represent the inertial properties of the actual interferometer, a dummy model of the instrument has been designed to explore the basic size, feel and mechanics of the instrument without simulating the actual function or exact visual appearance.

## **2.2 Computer modeling of the prototype**

The design and the optimization of the dummy prototype is performed using software tools. For this purpose, CATIA v5 is chosen for its simplicity and powerful computational capabilities.

### **2.2.1 Part design**

The CAD design is performed by first providing accurate dimensions of the model and with respect to these, creating the individual parts making up the complete dummy (see Figure 2-8).

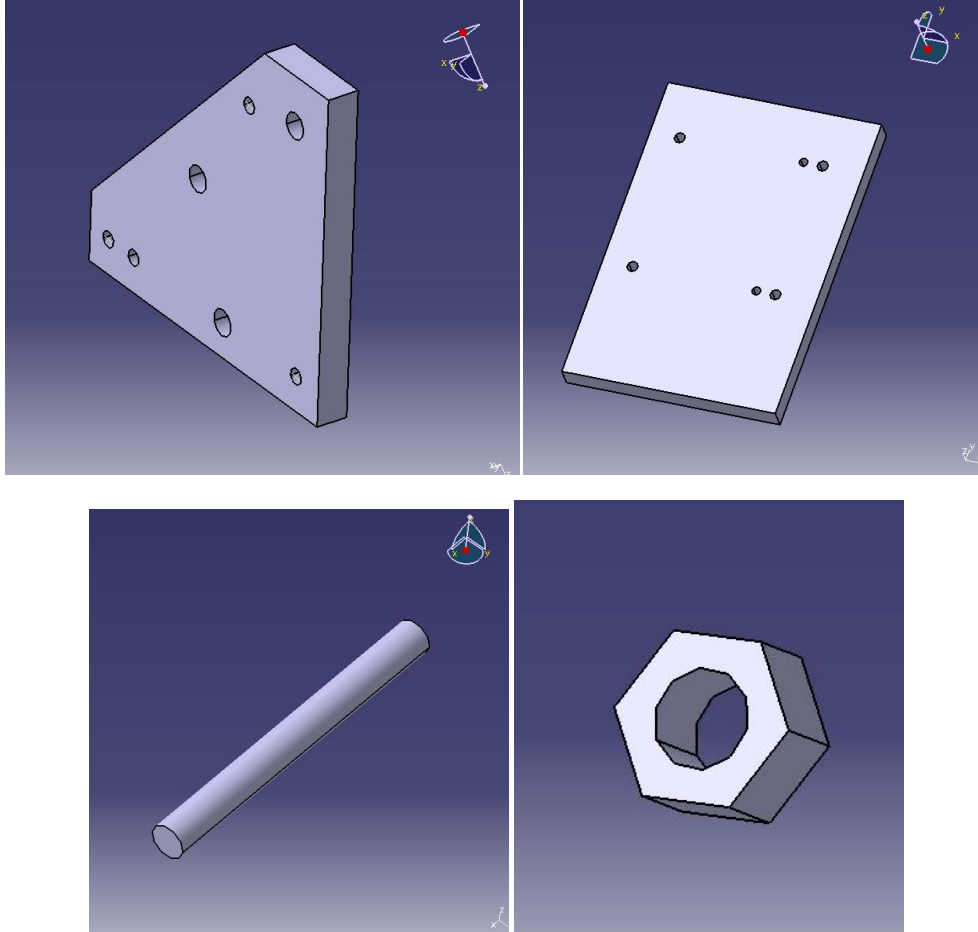


Figure 2-8: Some of the components making up the model assembly

### 2.2.2 Assembly

Once all the components are modeled in CATIA, one by one they are assembled together in a rigid fashion paying attention to the geometrical requirements. Figure 2-9 shows an exploded view demonstrating the assembly process. This procedure makes use of coincidence and offset constraints that will result in the correct assembly representing the dummy prototype (see Figure 2-10).

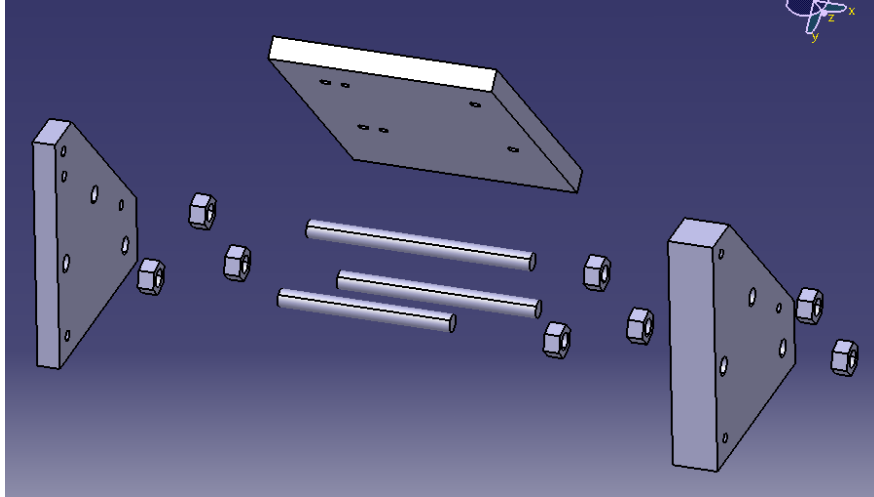


Figure 2-9: Exploded view of the model assembly

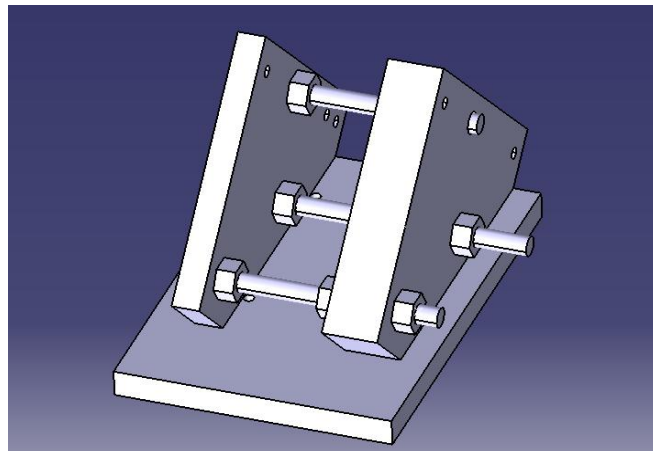


Figure 2-10: Dummy model created and assembled in CATIA

## 2.3 Modification of the dummy prototype to achieve an optimum model

### 2.3.1 The problem and the requirements

Previous studies on the damper-MIMA system utilized a dummy model made up of three aluminum plates bolted together in a rigid way. However recent changes in the MIMA device calls for an update on the dummy model.

The initial prototype, shown in Figure 2-10, must be modified to obtain an up-to-date model with the new inertial characteristics to have a behavior during experimentation similar to that of the actual device.

The most significant parameters that should be set for the model are its mass, center of gravity and moments of inertia. These desired values are listed in Table 2-4 along with the initial properties that the prototype possesses with respect to a reference frame shown in Figure 2-11.

Table 2-4: Initial and desired properties of the model

	Initial Prototype			Desired Model		
Mass [kg]	1.14			1.3		
	X	Y	Z	X	Y	Z
Center of Gravity [mm]	33.5	26.3	12.5	57.2	35.9	19.0
Inertia Matrix [kgxmm <sup>2</sup> *10 <sup>-3</sup> ]	x	y	z	x	y	z
I <sub>x</sub>	3.14	-0.93	-0.49	5.47	-2.32	-1.22
I <sub>y</sub>	-0.93	3.30	-0.78	-2.32	6.51	-0.71
I <sub>z</sub>	-0.49	-0.78	4.22	-1.22	-0.71	8.03

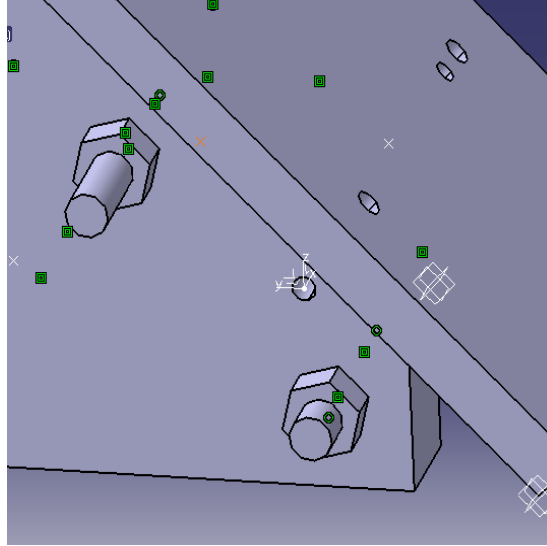


Figure 2-11: Local reference frame on the prototype

### 2.3.2 The method of optimization

There are numerous ways to achieve the desired values such as translating, swapping or modifying the components and adding or subtracting of masses. The most significant restriction is the mass, which should be 1.3 kg, suggesting a total added mass of 0.16 kg. Since there are infinitely many ways to do this, a systematic approach is implemented in which certain parameters are modified in a trial-and-error fashion keeping in mind the center of gravity and inertia requirements.

After various attempts, a simple but yet effective approach is found in which the thick vertical aluminum plate is replaced by a similar plate made of steel. This change allows the desired increasing of 0.15 kg in the model mass. Therefore the mass of the model is equal to that of the desired model. Finally, swapping the vertical plates the center of mass and the inertia matrix is improved. The resulting model is shown below in Figure 2-5.

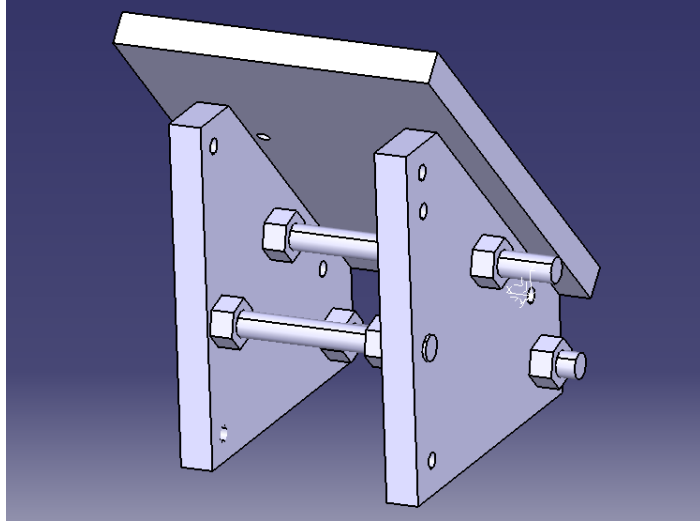


Figure 2-12: Modified final model of the MIMA

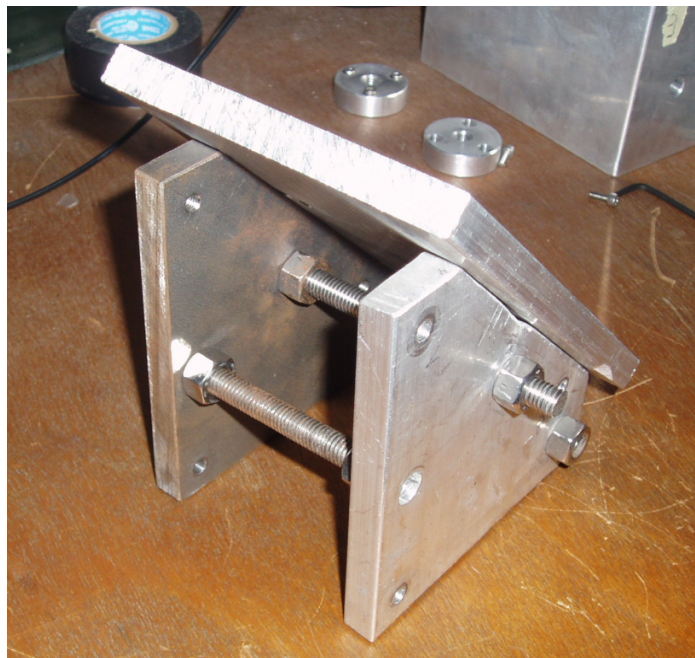


Figure 2-13 - Final up-to-date mockup to be tested

Once analyzed, it is seen that the final model decided upon has the following properties listed in Table 2-5.

Table 2-5: Properties of the final model versus those of the desired

	Final Model			Desired Model		
Mass [kg]	1.3			1.3		
	X	Y	Z	X	Y	Z
Center of Gravity [mm]	46.8	35.8	19.1	57.2	35.9	19.0
Inertia Matrix [kgxmm <sup>2</sup> *10 <sup>-3</sup> ]	x	y	z	x	y	z
I <sub>x</sub>	4.61	-2.22	-1.06	5.47	-2.32	-1.22
I <sub>y</sub>	-2.22	5.92	-1.41	-2.32	6.51	-0.71
I <sub>z</sub>	-1.06	-1.41	6.68	-1.22	-0.71	8.03

## 2.4 Validity of the dummy model for testing purposes

A close comparison of the properties of the dummy model and the desired values is required in order to decide whether this model can be used as a substitute for the simulation of the real instrument.

As previously stated, the most significant properties to be optimized were the mass, center of gravity and the moments of inertia around a certain axis. As seen from Table 2-5, with the help of the added mass, now the model has exactly the same mass as that of the device. However this criterion is not enough on its own since not only the mass but also

the shape of the model influences significantly the dynamical behavior. Because of this, the center of gravity and the moments of inertia with respect to the given reference frame must be compared. As seen from Table 2-5, the center of gravity and the moments of inertia are quite close to the desired values with some small deviations. The maximum error in the cog position is 18% and it occurs in the X direction and similarly for the moments of inertia the maximum deviation is 0.7 [kgxmm<sup>2</sup>\*10<sup>-3</sup>] and is present in the term  $I_{yz}$ . These result are acceptable for the purposes of this analysis. In the light of all these facts, this model is said to be good enough and it can be implemented as an experimental substitute of the MIMA instrument with expectations of similar dynamic behavior.

# **Chapter 3: Tuning of the dampers with one degree-of-freedom testing**

## **3.1 The need for damper tuning**

The dampers are by design adjustable and versatile elements since they include modular internal elements which can be tightened together variably with the help of the threaded damper cap. This specific characteristic allows for the modifications of damper properties such as stiffness and damping capabilities in a wide range.

This unique characteristic brings forth the task of tuning the dampers in order to achieve an optimum dynamic behavior. This objective will be accomplished mainly by adding (or subtracting) internal ring elements to the assembly as necessary and also by determining the optimum preload, that is the amount of closure of the damper, through a series of tests.

The MIMA will be mounted on three such dampers and therefore an optimal adjustment for each of them is required. The first approach for this study was to tune identically the dampers in order to obtain the same dynamical behavior. However this is not the only possible solution as will be shown at the end of this work.

## **3.2 Test methodology**

In order to characterize the mechanical properties of the dampers, a mechanical testing procedure was followed using a single damper and an appropriate dummy mass.

The design of the testing procedure includes the selection of the setup facility and sensors and the decisions upon the methods that are implemented. These decisions are made considering the objectives and the requirements of the mechanical testing. The various components used and the procedure followed are described in detail in the following sections.

### **3.2.1 Experimental equipment**

The mechanical testing setup is designed in order to assure a good performance regarding the results with a feasible cost.

The fundamental components of the setup are the inertial mass, the damper, the shaker, the sensors and the data acquisition system, some of which require further attention.

#### ***3.2.1.1 The mass***

The actual MIMA device is supported by three dampers mounted on certain points. Such a model cannot be used to test the behavior of a single damper. Thus a representative dummy mass is designed and implemented in the tests. This mass is of 0.35kg, which is approximately one-third of the actual MIMA, and is thus suitable for the testing of a single damper instead of three. As seen on Figure 3-14, the geometry is designed such that it is axisymmetrical and ideally it has the center of gravity along the damper axis and close to the damper tip.

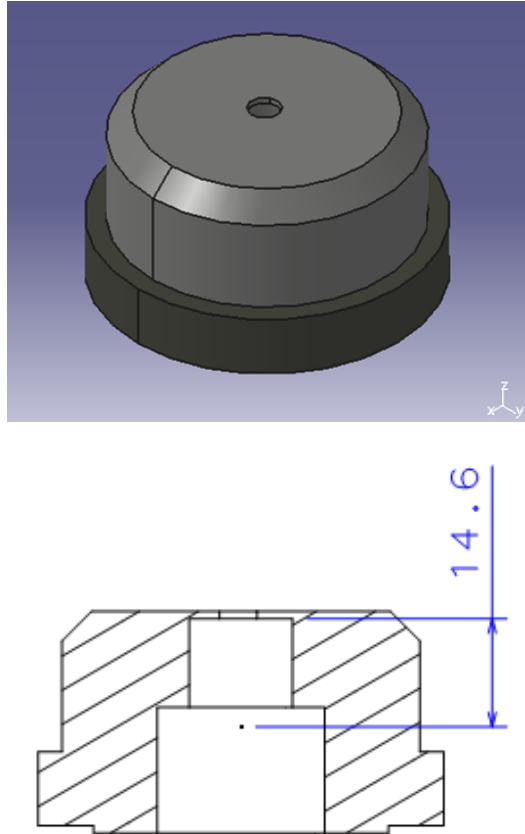


Figure 3-14: Dummy mass used for the single damper testing and section view showing its center of mass

### **3.2.1.2 Shaker**

A shaker is an electrodynamic exciter that is used to generate certain vibrations to produce the desired environmental conditions. For the scope of this work, they are used to simulate the probable vibrations that may act on the MIMA during its take-off and landing on the surface of Mars.

Two different shakers will be used for the purposes of this analysis, the decision being done on their simplicity versus their capabilities. The most significant properties of these shakers are their force, acceleration,

velocity and displacement limits. The smaller TIRAvib vibration generator will be used for the single-damper testing procedures that include a smaller mass being excited. On the other hand for the full model testing, a larger and more capable shaker will be used (see Figure 3-15).



Figure 3-15: Vibration generators (shakers) used in the tests performed

Both of these vibration generators are capable of producing the high level and high frequency sine and random vibrations that will be present in the environmental conditions of the MIMA and therefore are appropriate for the testing of the dampers.

### ***3.2.1.3 Sensors***

The stimulus for the testing of the dampers is in terms of acceleration and the response is measured using accelerometers. For this purpose, very small accelerometers designed specifically for measuring vibration on mini-structures and small objects are implemented (see Figure 3-16).

These accelerometers offer high resonance frequency and wide bandwidth with their light weight eliminating mass loading.<sup>[8]</sup>



Figure 3-16: ENDEVCO 27A11 accelerometer used for vibration measurement

For the single degree of freedom case several accelerometers are employed for each test with appropriate voltage sensitivity and dynamic performance.

#### ***3.2.1.4 Data Acquisition System***

The electrical signal coming from the accelerometers have to be conditioned and transformed into meaningful data before it can be useful. To achieve this goal, a data acquisition system is necessary.

The signal coming from the accelerometer cannot be acquired immediately but needs to be conditioned into a signal easy to read by conventional instrumentation. Therefore the use of a signal conditioner is critical unless it is already mounted inside the data acquisition board. The data acquisition board samples the signal and sends it to the PC where it is stored for further processing. Such a flow of data is shown schematically in Figure 3-17. The actual system involving these elements is shown in Figure 3-18.

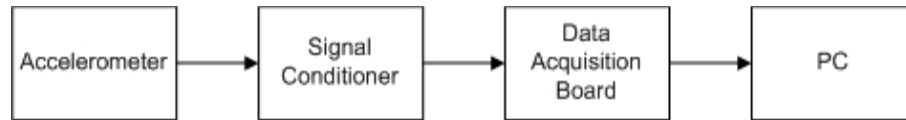


Figure 3-17: Data flow from the accelerometer to the PC



Figure 3-18: Data acquisition system involving the signal conditioner, data acquisition board and the PC.

### 3.2.2 Experimental Modal Analysis techniques

Experimental Modal Analysis is a methodology that enables a structure's modal properties (natural frequencies, modal damping factors and mode shapes) to be determined from experimental observations of its dynamic response under test conditions.<sup>[9][10]</sup> The main objective of experimental modal analysis is the construction of a mathematical model. However, as far as this study is concerned, construction of a Finite Elements Model is by far more critical.

Nowadays, the vast majority of practical applications of experimental modal analysis provide the measured data in the form of Frequency Response Functions (FRF). Frequency Response Functions are normally used to describe the input-output relationship of any system. It is with the help of these response functions that the modal parameters can be determined.

The study of the damper dynamics is performed mostly using these techniques that will be detailed further on. However the main idea is always the same, using an FRF describing the input-output relationship.

$$H(\omega) = \frac{Y(\omega)}{X(\omega)}$$

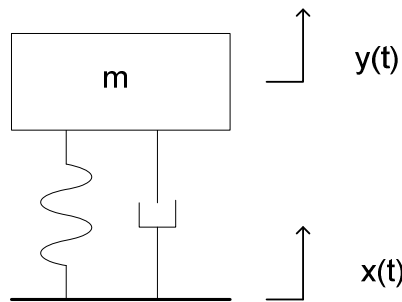


Figure 3-19: The basic Frequency Response Function used throughout the study as a ratio of measured accelerations.

### 3.2.3 Test setup

There are three significant physical properties of the damper, which are the stiffness in the axial direction, stiffness in the radial direction and the rotational stiffness. The sense of these directions is given below in Figure 3-20.

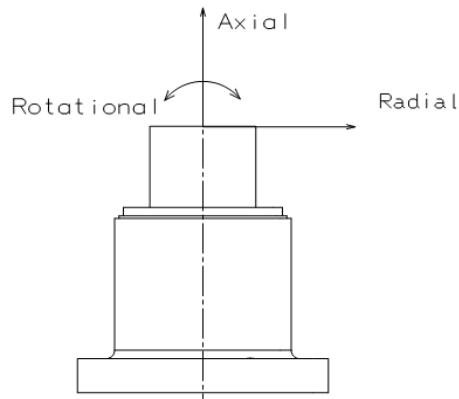


Figure 3-20: The convention used for the directional parameters of the damper

In order to assess, quantify and tune these three directional properties of the damper, reliable test methods are designed for each case generating a one degree of freedom motion.

#### 3.2.3.1 Axial stiffness testing

First of all the dampers must be tested along their axis to see if they satisfy a certain behavior in the axial direction. For this purpose, a single damper is mounted on the shaker and the mass is bolted on top of the damper such that deformations other than the ones in the axial direction are restraint as well as possible. Accelerometers measuring the reference stimulus and the resulting response are placed and fixed along with their cables to assure no interference with the dynamics of the system. Schematics of such a setup can be seen in Figure 3-21.

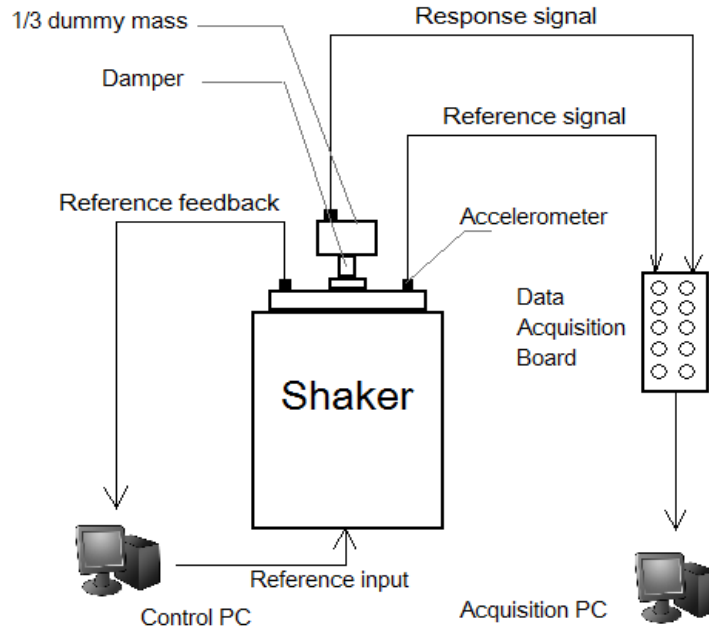


Figure 3-21: Mechanical testing setup schematics for the single damper vertical direction

As seen from the above schematics the stimulus, i.e. the reference vibration that the shaker imposes on the damper, is created with the help of the Control PC. The control action is a closed-loop feedback system that utilizes the signal from the reference feedback accelerometer. Simultaneously, another accelerometer measures the same reference acceleration and feeds it to the Acquisition PC for late signal processing tasks. Other sensors located at the top of the dummy mass are used to measure the response.

Considering that ideally the dummy mass has its center of mass along the axis of the damper and that the damper and the mass are fixed together restraining any undesired motion, the only motion that can occur is in the axial direction and is due to the deformation of the damping elements. However this expectation is not so close to the reality. In practice, it is wise to account for a small offset in the dummy's center of mass due to poor manufacturing tolerances. This fact may lead

to other non-restrained displacements, causing some rotation of the mass. Therefore it is reasonable to use two accelerometers on top of the dummy mass (see Figure 3-22) in order to measure the axial displacements as well as any undesired rotations.

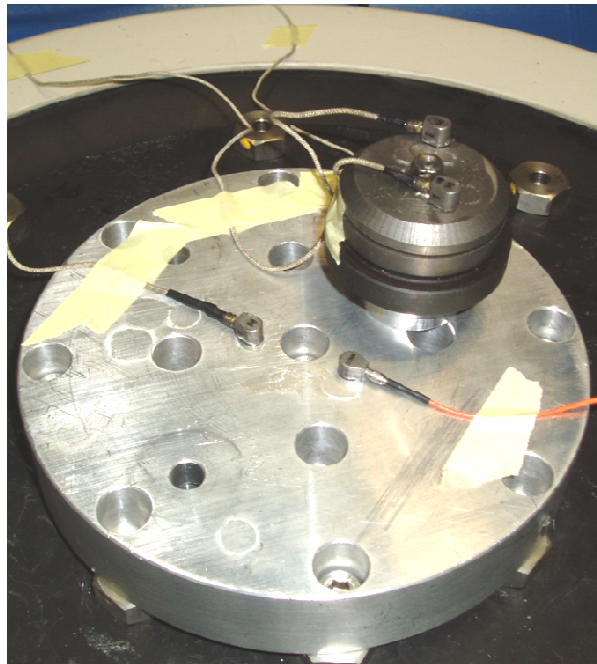


Figure 3-22: A fine measurement setup with four accelerometers including one for feedback, one to measure the reference and two for measuring the response.

### ***3.2.3.2 Radial stiffness testing***

Due to the environmental conditions, the dampers are strained not only in their axial direction but also in their radial direction. These vibrations acting radially are as critical as the axial ones and thus the dampers must be tested in this axis and their corresponding radial stiffness must be assessed and optimized.

The setup for this procedure is quite similar to that of the axial stiffness tests. The main difference in this case is that the stimulus must be in

the direction to amplify the deformations straining the radial stiffness. For this purpose a large metallic block is used and the damper-mass assembly is mounted on it with the damper axis being horizontal (see Figure 3-23 for schematics).

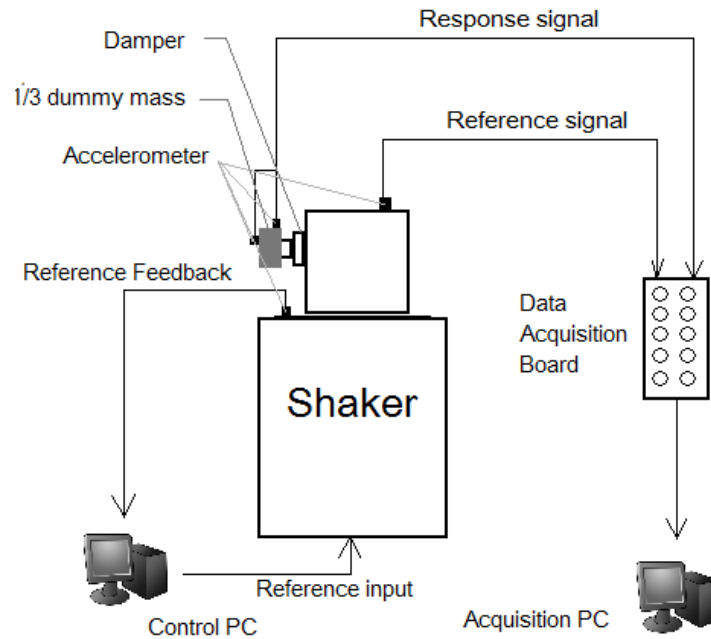


Figure 3-23: Mechanical testing setup schematics for the single damper radial direction

As seen from the above, the acquisition and the flow of data is similar to the setup discussed before. One particular point to be noted is the placing of accelerometers for the optimal analysis of the damper response. Figure 3-24 shows the positions of the three response accelerometers on the dummy mass and two reference accelerometers of the metallic block, one for storage and one for control feedback.

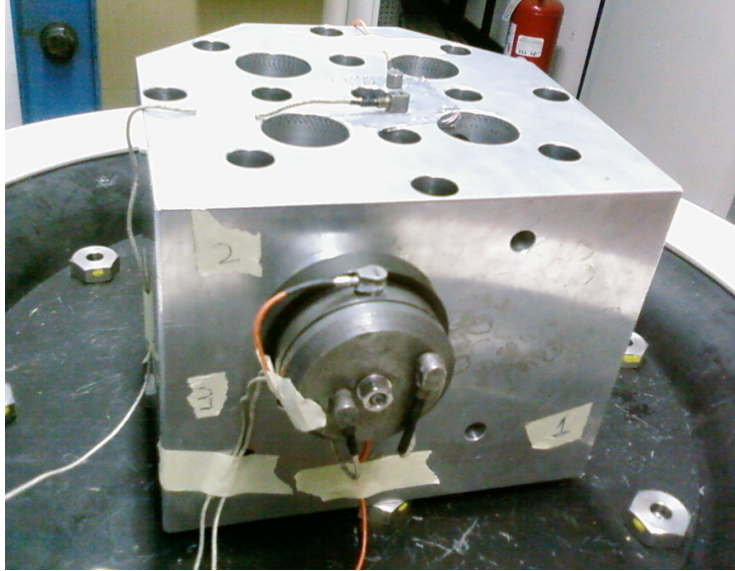


Figure 3-24: Accelerometer configuration used for the radial testing of the dampers.

Due to the fact that the center of mass of the dummy mass is not at the damper center, the expected response is a combination of radial translation as well as some rotations. Therefore three accelerometers are required to analyze the behavior correctly. The accelerometer on the top circular edge of the dummy mass measures the response in the direction of excitation while the other two measure the axial accelerations and also account for various rotations of the mass.

### ***3.2.3.3 Rotational stiffness testing***

The final property that the dampers must be assessed for is the rotational stiffness. This parameter accounts for the small rotations at the damper tip that the translational stiffness parameters cannot explain.

The method for the estimation of rotational stiffness is to check the Frequency Response Function from the various single degree-of-freedom tests on the damper. With the help of an accelerometer couple, rotational resonances can be identified and the stiffness estimation can be performed accordingly.

### 3.2.4 Vibration stimulus for the single degree-of-freedom tests

The testing and the characterization of the dampers require a determined stimulus that is the foreknown reference input. Therefore a signal driving the shaker is generated and controlled in a closed loop feedback manner by the control PC.

The environmental conditions of the MIMA include vibrations that are sinusoidal, random or shocks by nature. However for the characterization of single dampers, only the sweep sine will be used it.

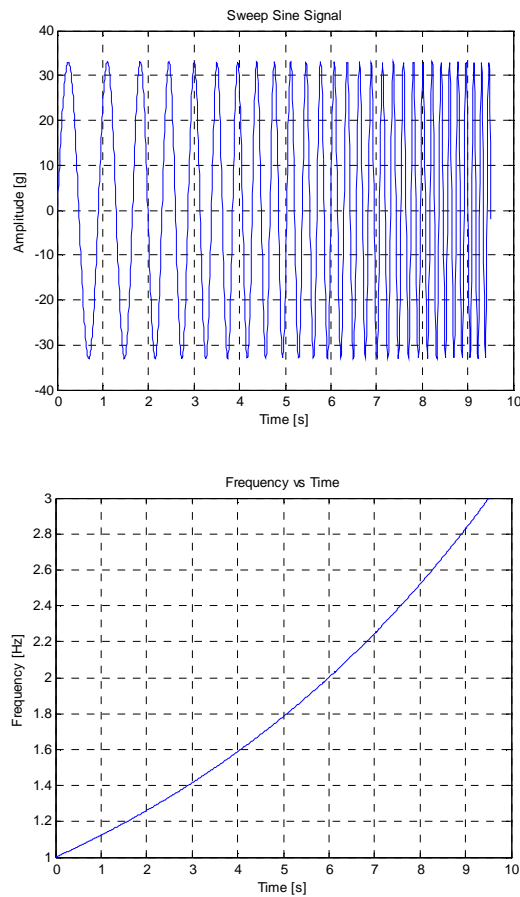


Figure 3-25: A sample sweep sine with amplitude equal to 33g and increasing frequency

As seen in the above figure, the sweep signal is a sine with constant amplitude and increasing frequency at a constant logarithmic rate (usually defined in octaves/min). This provides a good method to excite a wide band of frequency in a small amount of time.

The environmental conditions suggest a sinusoidal excitation with amplitude of 33g. Therefore the dampers must be tested and their parameters characterized at this vibration level. Characterization at any other level may lead to some errors due to the high non-linearity of the dampers. However this level is quite high and repeated applications may result in the damaging of the internal ring elements. Therefore alternate signals with lower amplitudes are implemented as well, such as at 0.5g, 5g, 20g, etc...

### **3.3 Tuning of the dampers**

The tuning procedure includes numerous tests performed on the dampers in a trial and error fashion varying each time some certain parameter, the testing orientation and even the damper configuration until an acceptable dynamic behavior is achieved. The most significant factors involved in the tuning process are the effect of closing torque on the dampers, the effect of excitation amplitude and the different behaviors associated with different configurations of damping ring elements.

#### **3.3.1 Objectives of the tuning procedure**

The main objective of the damper tuning procedure is to test the dampers to see if they satisfy the dynamic response requirements and if not, modify them in some manner to achieve the desired response.

The MIMA environmental conditions suggest two types of vibrations acting on the instrument, the sine and the random vibration environment. From these, the sine environment is more significant at

low frequencies (below 100 Hz) while the random one is more critical above 100 Hz (see Figure 3-26).

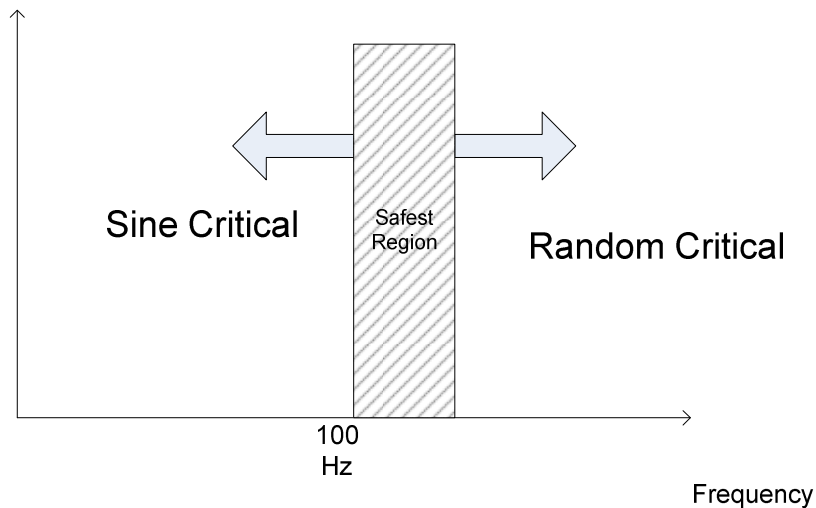


Figure 3-26: The critical sine and the random vibration environment

In the light of these considerations, it is desired that no resonance occurs below 100 Hz where the sine vibrations are critical. The resonance should preferably be above 100 Hz, but not so high as to cause suffering from the strong random vibration environment. The safe area can be identified within the 120-170 frequency range.

An important outcome of the single damper tuning tests is the estimation of the damper stiffness parameters so that they can be used further on in computational applications, such as the Finite Element Model development.

The mounted MIMA has three such dampers and due to some manufacturing tolerances and imperfections, they are not identical. As previously stated, the final objective of the tuning process is to test each damper and tune them with respect to each other to obtain three identical dynamic responses.

### 3.3.2 Excitation amplitude and damper non-linearity

As previously mentioned, the dampers are highly non-linear elements. This means that their behavior is strongly dependent on the magnitude of the incoming stimulus and therefore a formulated linear model is only valid for a certain level of excitation.

To demonstrate this effect, various tests can be performed on the same damper with different levels of excitation. This is a critical phenomena of the single damper testing and qualification since the actual high level vibrations cannot be applied on a frequent basis due to damage-prevention concerns.

Below, in Figure 3-27, are plotted two Frequency Response Functions corresponding to the damper response for a given reference excitation. These plots represent two different tests performed on the same damper, one test with a sweep sine at a constant 0.5g level and the other with a sweep sine at 5g level, i.e. 10 times stronger than the previous one.

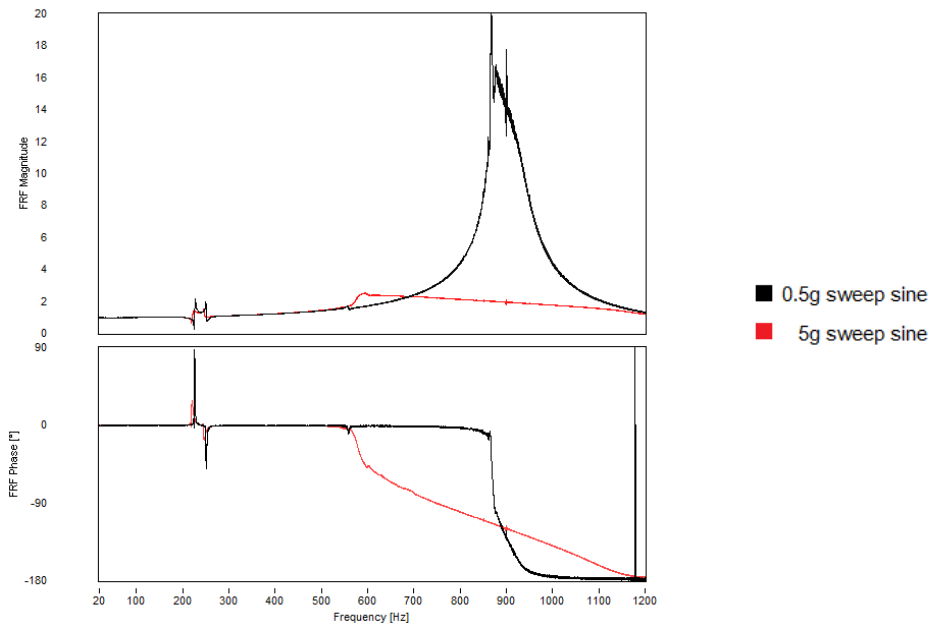


Figure 3-27: FRF comparison of the same damper response to a 0.5g sweep and a 5g sweep sine.

There are obvious differences between the two responses of the same damper. One significant difference is the decreasing of the natural frequency at the higher level excitation. This fact is apparent from the shift of the resonant peak to the left in the magnitude plot and also the shift of the phase fall in the phase plot. The fact that the natural frequency is adversely affected by the excitation amplitude is a phenomenon that must be taken into consideration throughout the course of this study. Another obvious difference is the increase of damping at the 5g test. In this test, the resonant peak is significantly reduced and the phase fall is rotated unlike the steep fall at low excitation level.

Another test performed at higher excitation levels but within a smaller frequency band exhibit similar results (see Figure 3-28). At 100 Hz the 33g plot has a greater increase in magnitude and a larger fall in terms of phase, which suggests the shift of the natural frequency to a lower value.

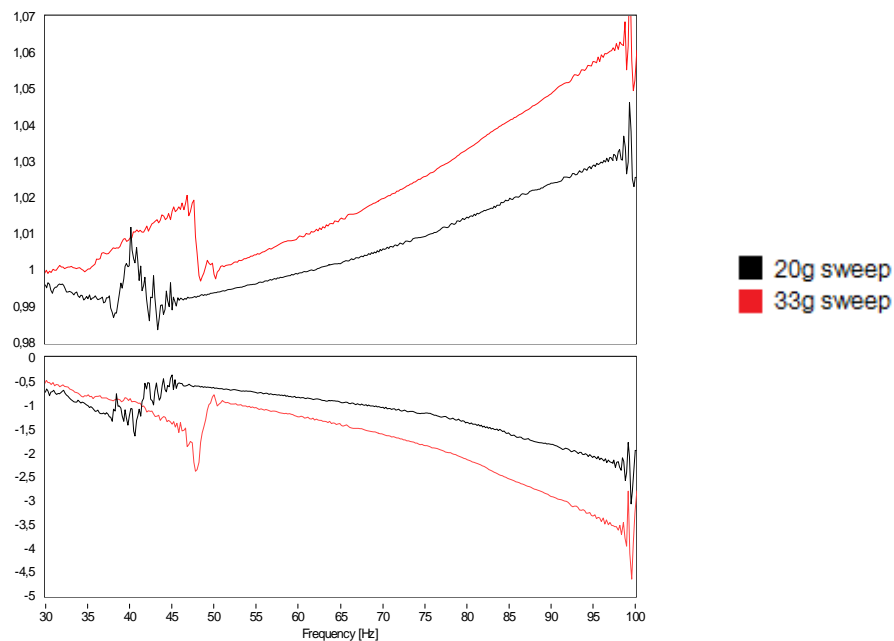


Figure 3-28: FRF comparison of the same damper response to a 20g sweep and a 33g sweep sine.

### **3.3.3 Damper response and tightening preload**

The dampers are by design adjustable elements so that their dynamic response can be modified by simply increasing or decreasing the preload on the ring elements with the help of the threaded cap acting against the inner element. This preload can be measured accurately with the help of a micrometer, thus allowing a systematic study of the effect of tightening or loosening the dampers. However this preload cannot be extremely small in order to prevent any opening during operation and it cannot be too large as there is a limit to this preload due to the limited travel of the regulation screw.

The effect of preload has been studied by testing the same damper configuration with a certain excitation profile, gradually increasing the preload and comparing the damper response. The following figures and tables show a comparison of four different tests, run with the same damper that was gradually loosened. The excitation profile is a sweep sine with a **5g** amplitude within a frequency band 20-1000Hz.

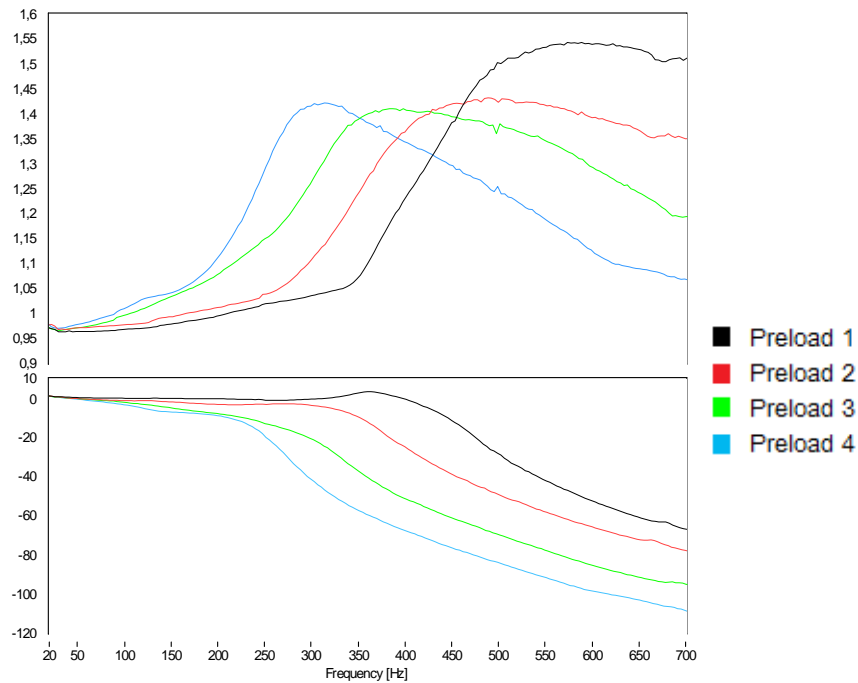


Figure 3-29: FRF comparison of the damper responses at different preloads.

Table 3-6: Comparison of damper modal parameters corresponding to different preloads

	<b>Preload [mm]</b>	<b>Natural Frequency <math>f_o</math> [Hz]</b>	<b>Peak Magnitude</b>
<b>Preload 1</b>	30.3	850	1.6
<b>Preload 2</b>	30.5	800	1.4
<b>Preload 3</b>	30.7	650	1.4
<b>Preload 4</b>	30.9	550	1.4

A close examination of the above test results reveals the obvious effect of damper preload on the damper response and naturally, its dynamic properties. The gradual loosening of the damper shifts the phase plot to the left resulting from the lower natural frequency and thus indicating a

lower stiffness. Conversely increasing the preload will increase the natural frequency and the stiffness of the damper. On the other hand a look at the peak magnitudes and the phase slopes suggests that the damping is not so significantly altered by the different preloads.

This aspect of the dampers, i.e. the possibility to vary its stiffness and thus its dynamic response, is a key advantage and is utilized to achieve the damper tuning objectives discussed previously.

### **3.3.4 Radial behavior of dampers**

Besides all the previously investigated factors affecting the damper response, there is another significant consideration, which is the directional properties acting on the response of the dampers. Two different stiffness parameters are defined to represent this directional behavior, the axial and the radial stiffness (recall Fig 3.7).

The translational stiffness in the radial direction is tested and evaluated using the setup described previously in Section 3.2.3.2. This system basically provides an excitation of the damper-mass assembly causing deformations that are mainly driven by this stiffness parameter.

For the purposes of this test, three accelerometers are used to measure motion of the dummy mass in a complete way since the motion is a combination of the axial and radial deformations (see Figure 3-30 for the visualization of the accelerometer positioning).

The FRF given below in Figure 3-31 demonstrates the behavior of the damper when the stimulus acts in the transversal direction.

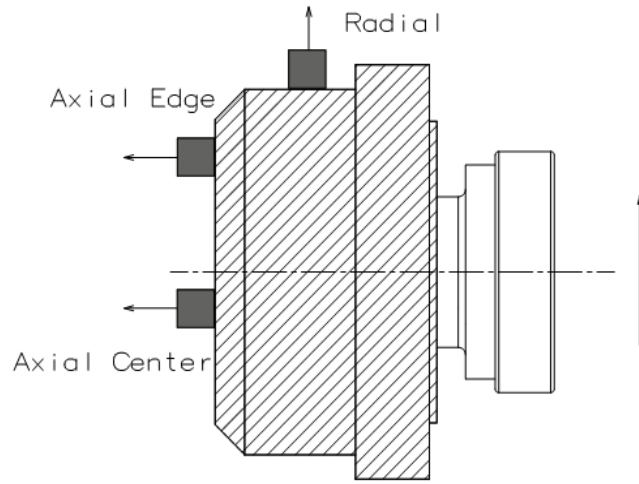


Figure 3-30: Placement of the accelerometers on the mass for the transversal testing.

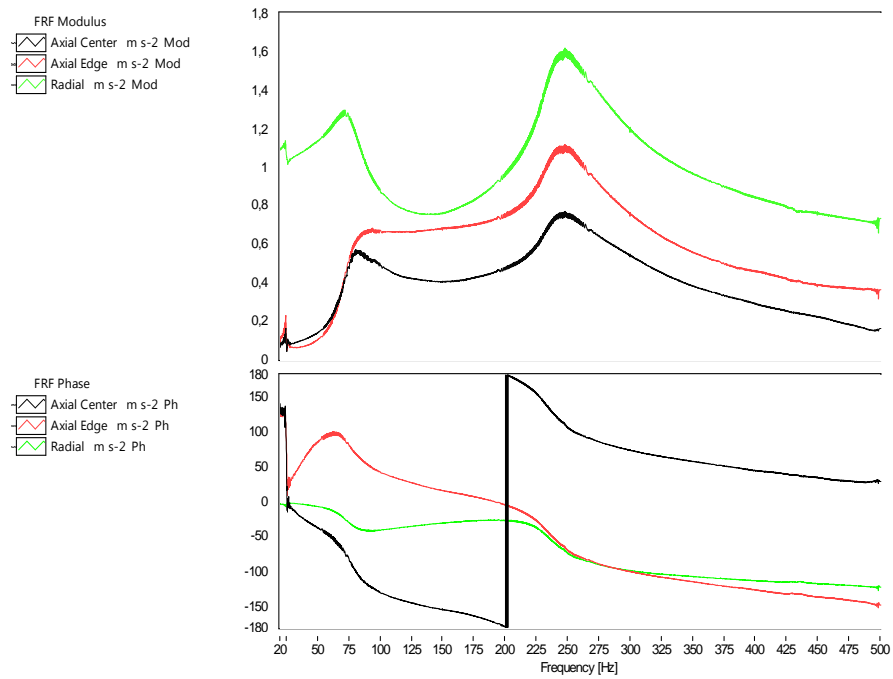


Figure 3-31: FRF of the three accelerometers versus the reference sweep sine acting in the transversal direction.

This FRF requires a close examination in order to deduct some useful conclusions from it. The first observation would be the existence of two resonance regions from the magnitude plot. However from the phase plot it is apparent that the motion around these regions is of a completely different nature. At first peak, the response of the two axial accelerometers diverge and they become out-of-phase. This suggests a rotational mode rather than the deformation of the damper in the radial direction. Later on in the frequency range, around 250 Hz, a resonance in the radial direction is observed while in the axial one the accelerometers continue to behave the same (constantly out-of-phase). This fact suggests the existence of a purely transversal mode at that frequency.

All the results obtained from the numerous tests in the transversal direction are of critical importance and will later on be used for the characterization of the damper elastic parameters (see Chapter 4).

### **3.3.5 Damper Response Synchronization**

The first approach to get the desired instrument dynamic response was based on providing three equally tuned dampers. However to achieve this is not so straightforward since the equal configuration and the equal preload on the dampers does not necessarily guarantee an equal response. This is due to the manufacturing tolerances of internal elements of the damper. Therefore, if an equal tuning is required, this must be performed through a trial-and-error procedure slightly varying the preload on the dampers and comparing the resulting responses.

A procedure such as this one was performed to obtain three dampers with equal stiffness parameters, i.e. similar natural frequencies. Initially all the dampers were closed at the same preload distance and were tested in this configuration to have some initial idea about the internal elements' differences. For the testing, a 20g Sweep Sine was used. The Frequency Response Function was calculated between the reference stimulus and the damper response. A comparison of the results is given below in Figure 3-32.

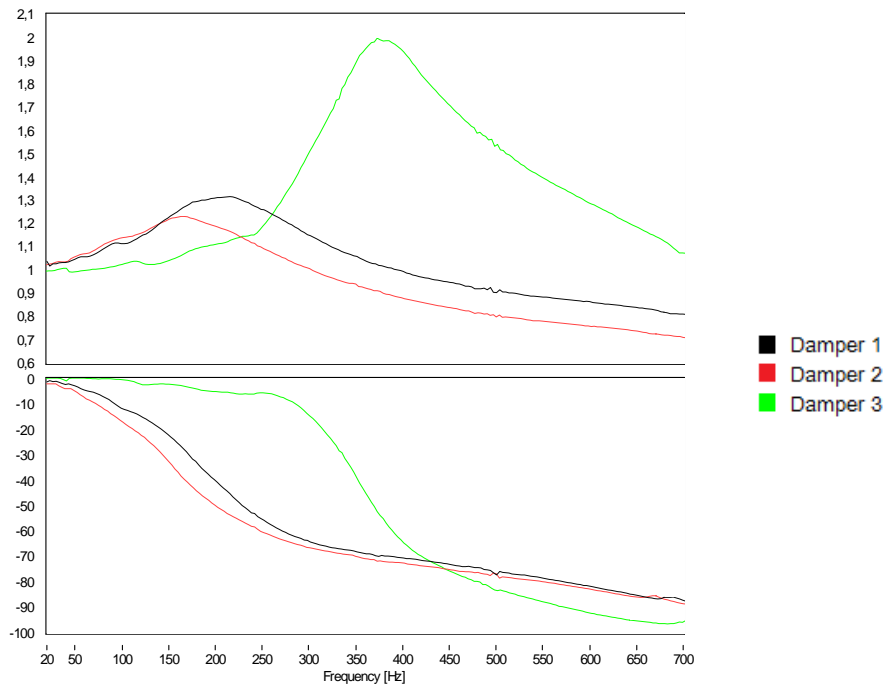


Figure 3-32: Comparison of the FRFs of the three dampers to a 20g sweep in their fully closed state.

Investigating the above plot, it is obvious that the components of the three dampers are not identical due to some deviations within the tolerances in manufacturing. While dampers 1 and 2 are acceptably similar, Damper 3 is much more stiff with respect to the other and most be loosened. Therefore a tuning session is required in which the responses of the three dampers can be synchronized. By varying the preload distance slightly a better combination can be achieved such as the one in Figure 3-33.

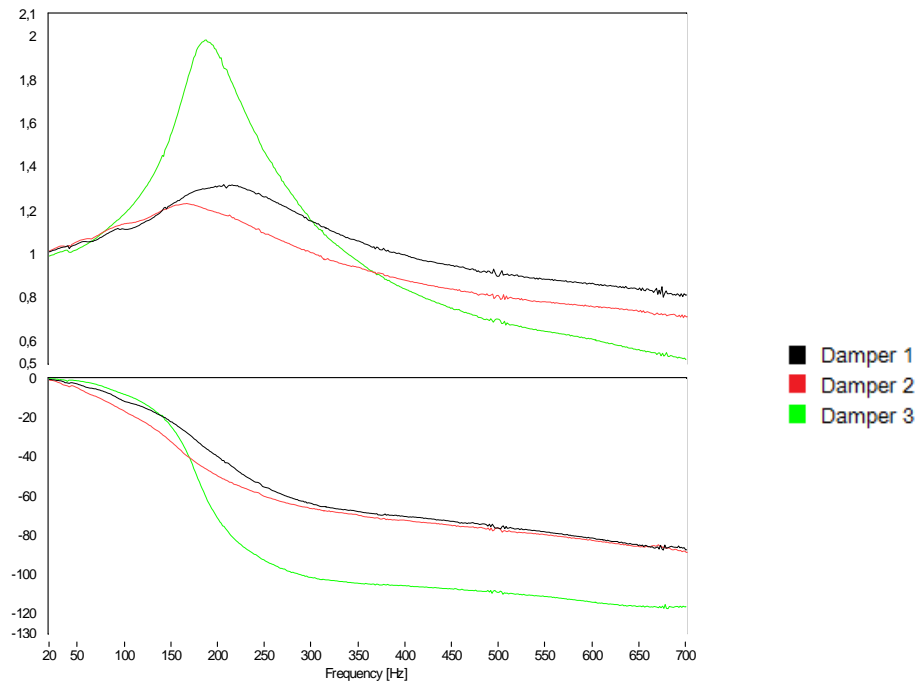


Figure 3-33: The three dampers synchronized in terms of response.

The preload on the dampers in terms of distances that result in the response shown above is given below.

Table 3-7: Preload distances on the dampers

	<b>Preload [mm]</b>
Damper 1	29.2
Damper 2	29.2
Damper 3	30.2

In this case the dampers are quite similar in terms of natural frequencies and thus have similar stiffness parameters. However looking at the peak magnitudes and the phase fall slopes it is apparent that they have different damping ratios. Clearly Damper 3 has a lower damping than the others. This phenomenon can be explained considering the effect of several factors including the tolerances on the nylon ring

spacers and the rubber elements being forced against the titanium producing friction. Unfortunately this behavior cannot be modified by changing the preload and therefore it has been accepted as it is and the tuning process is concluded.

### **3.3.6 Configurational modifications of damper assembly**

The damper elements are, by design, adjustable elements made up of small modular rings assembled together and tightened with a certain preload. The fact that the ring elements are interchangeable allows for the formation of different assembly configurations that might have some advantages with respect to the others. This property is several times taken advantage of throughout this study as it is considered necessary.

#### ***3.3.6.1 Changes to the damper assembly***

The initial assembly of the damper ring elements included four silicon rings separated and supported by 4 nylon spacers (two small in between, two large at the tips).

A more closely-packed damper configuration can be achieved by adding some extra ring elements into the assembly. This results in a stiffer damper. Besides increasing the stiffness, a tightly closed damper is favorable since the chances of having some free motion before the actual elastic deformation is eliminated significantly.

To achieve a tightly-packed damper, the first step was to add a small nylon ring that is half as thick as the ones already present in the assembly. This element is then inserted between the rigid damper structure and the silicon ring to achieve the damper configuration called Config 2.

The above configuration is definitely more packed than the initial one. However, it is possible to obtain an even tighter assembly (Config 3) within the damper's mechanical limits by adding another half nylon ring similar to the previous one on the opposite side.

### 3.3.6.2 Effects of the insertion of additional rings on the damper response

The configurations described above were all tested on the shaker with the one degree-of-freedom single-mass setup to compare the differences in the response and thereby describe the effect of introducing additional ring elements into the damper assembly.

The comparison was again performed in terms of FRFs between the reference stimulus and the damper response. In Figure 3-34 below, three such FRFs corresponding to the three configurations described previously are plotted within a frequency band of 40-100 Hz as a response to a 33g sweep excitation.

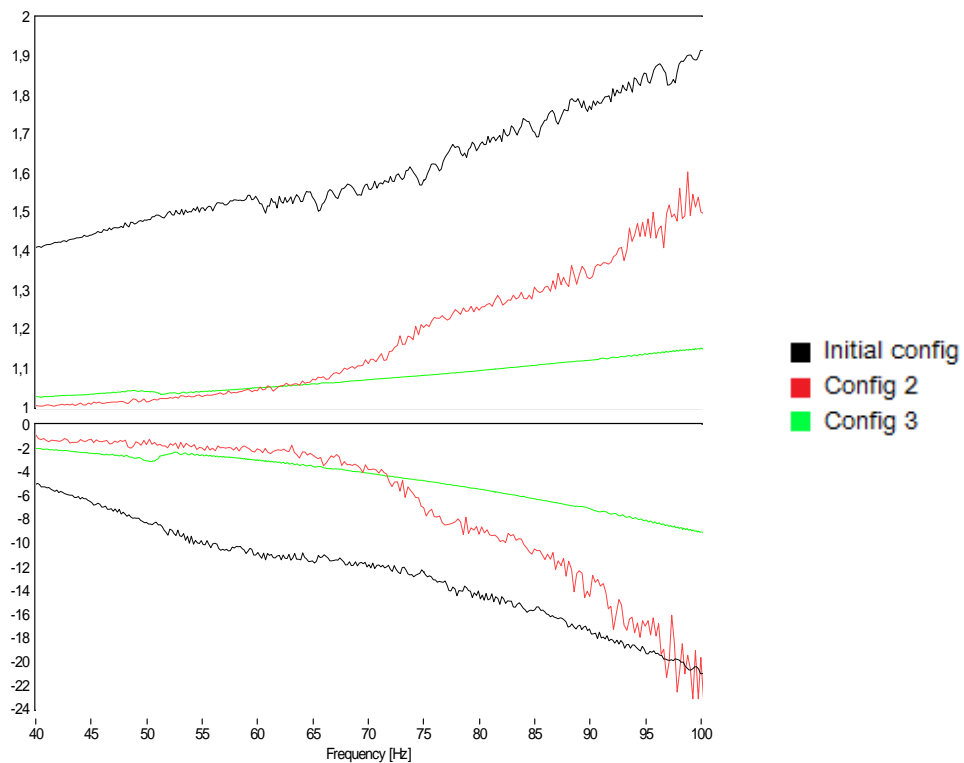


Figure 3-34: Comparison of FRFs of the dampers in three different configurations.

The above figure verifies all the expectations from the configurational modifications on the dampers. Looking at the phase trend, it can be

stated that the natural frequency increases as additional elements are inserted into the assembly, thus increasing its stiffness. On the other hand, the FRF Magnitude plot reveals another useful information, which is the increase in the damping caused by the presence of extra rings. The rings which are fitted into the metallic damper structure cause friction and dissipate energy. Therefore the increase in number of such elements induces a higher damping ratio on the system.

The effect of the additional ring on the natural frequency of the damper can be better visualized from the Figure 3-35, where a low level sine-sweep (Resonance Search, 0.5g sweep sine) is performed within a large frequency band.

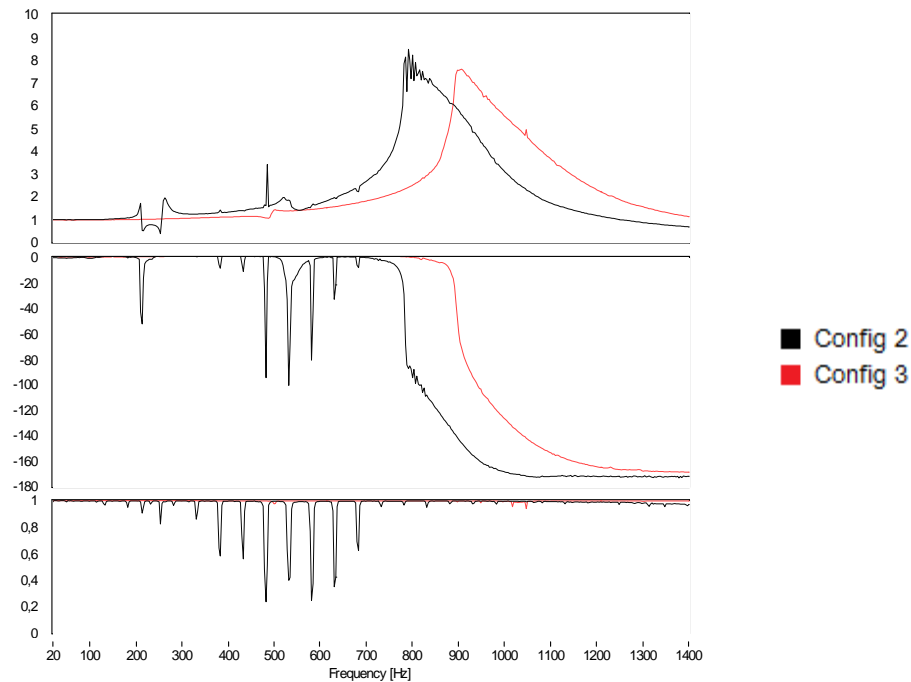


Figure 3-35: Low level Resonance Search response of the damper in Config 2 and in Config 3.

The above plot gives a comparison of the response of the two given configurations of the dampers. The initial observation from the FRF of *Config 2* is the presence of periodic peaks in the spectrum which are not

actually evident in the time history. In order to investigate the nature of these peaks, the time-frequency plot corresponding to the data obtained with this configuration is given

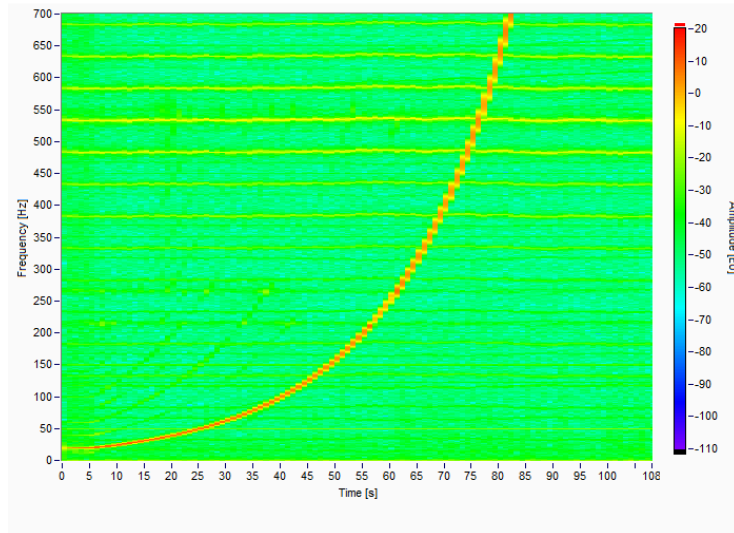


Figure 3-36: Time-frequency plot for the damper channel in the testing of Config 2

Examining the above plot and the coherence function, it is concluded that these peaks are in fact constant frequency incoherent components in the signal caused by some electrical noise whose source has not been identified, but that was present in this specific test run. The region of interest of the FRF however is not affected dramatically and by excluding the frequencies of the disturbances, the obtained test results can be used for comparison.

As the above plot suggests, adding another nylon ring results in a stiffer damper with a higher natural frequency (in this case almost 100 Hz higher). Still there is a physical limit to the number of additional rings that can be added to the damper assembly. With Config 3, i.e. with two small half nylon rings included, the damper is in the maximum packing configuration, no additional element can be added without changing the design of the metallic parts.

#### ***3.3.6.4 Energy dissipation of spacers***

The environmental conditions that the dampers face during the actual operation are quite harsh and so must be the testing procedure for their qualification. The sweep environment foresees excitations up to 33g in amplitude while the random environment imposes vibrations with RMS value of 16 g. Provided that the friction is one of the phenomena exploited for the dissipation of the vibrations power, some wearing can take place.

The dampers using nylon elements have, in some cases, shown a change in performance that was not negligible after the high level sine test. For this reason a different material has been adopted, being the wearing related to the local temperature increase, a material with high operating temperature such as the polyimide resins would have been the best choice. A glass fiber reinforced nylon was eventually adopted because of its immediate availability. This proposed change proved to solve the wearing issue.

### **3.4 Dampers in their final tuning and configuration**

After numerous tests performed on the dampers, trying over and over changing several parameters and modifying the configurations as described in detail in the previous sections, a satisfactory final damper tuning is achieved.

This damper configuration has two additional nylon spacers in the middle of the assembly with respect to the initial one in order to achieve a more tightly closed damper. Moreover, one of the large nylon rings at the tip of the assembly is replaced with a dimensionally identical one made of glass fiber reinforced nylon to avoid the problem of melting due to high energy dissipation.

The damper's preload is adjusted so that the damper is tightly packed. The measured preload is around  $h \cong 29.2mm$ , almost fully-closed. With

this approach, a quite stiff and stable (no free translation of inner elements) damper is obtained.

Results in terms of FRF to sweep sine tests performed on this specific final damper are given in the following figure below.

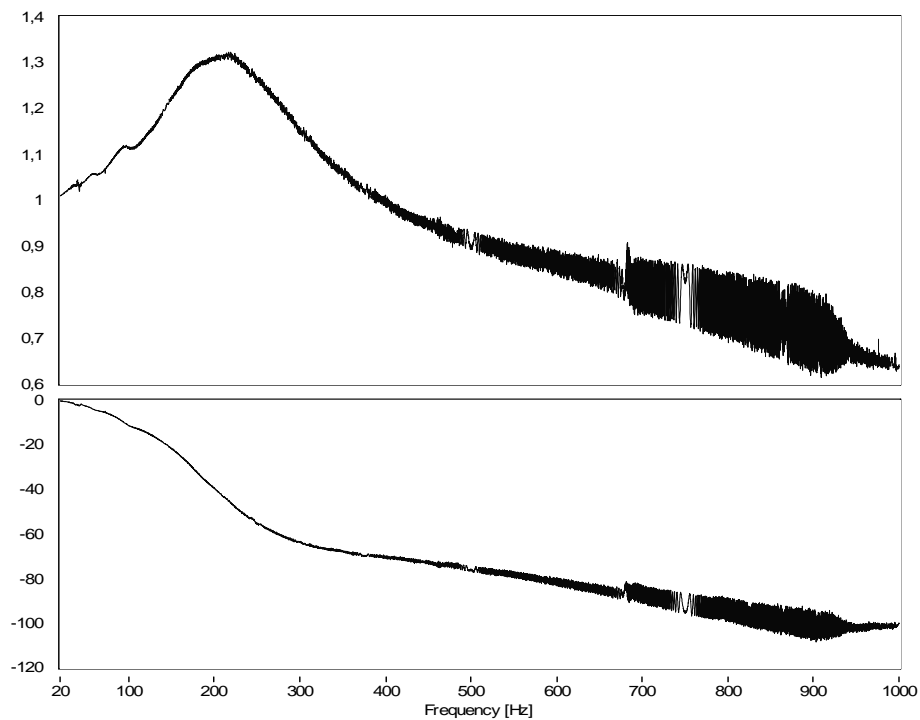


Figure 3-37: Axial sweep sine test at 20g in the range 20-1000 Hz.

The above plot demonstrates only the response of Damper 1 previously shown on Figure 3-33 along with the other dampers. This single FRF can be accepted as a representative behavior for all the identically tuned dampers and used in the following analyses accordingly.

Recalling the MIMA environmental conditions, the behavior of this single damper seems to be acceptable. The natural frequency seems to be around 300-400 Hz which is well above 100 Hz but still not so high, as to reduce the advantages for the random environment. In addition,

the overall FRF does not have a very high amplification (1.3 maximum). This is also a positive result suggesting this damper configuration might as well be the final one.

### **3.5 Results and discussion**

As mentioned before the damper design is adjustable and quite versatile, in the sense that it is possible to tune the dampers in order to obtain a desired response for a given excitation. For this purpose, many experiments were performed to test each and every aspect of the various possibilities of the dampers.

All the tests were performed with a representative dummy mass one-third of the original instrument to test a single damper each time, in a one degree-of-freedom system. The setup and the procedures were designed to comply with Experimental Modal Analysis techniques that allow the characterization of the system through its modal parameters, such as natural frequency, damping ratio and the vibration modes.

Three test setups were used to test and evaluate the three directional properties of the dampers. Even though this procedure was quite straightforward for the axial direction, evaluation of the radial properties required transversal excitations which resulted in combined modes. These modes had to be distinguished in the FRF by using several accelerometers to visualize the motion completely.

The dampers had to be tuned in order to get the optimum tightening preload and the best inner assembly. During this procedure numerous tests were performed in all orientations, varying the parameters to be optimized in a trial-and-error fashion, until finally a satisfactory damper response is achieved.

Surely the decision upon the optimum damper cannot be made just by looking at the single damper-single mass tests. This is a method for the characterization and provides a good insight. The dampers should then act satisfactorily when the three of them are used together with the

MIMA. Once the damper parameters are extracted from the single degree-of-freedom tests, also the FEM analysis of the system can be a resourceful and fast tool. All these steps to achieve the final system will be explained in detail in the following chapters.

## CHAPTER 4: Damper properties estimation

The behavior of the dampers, as previously discussed, are highly nonlinear. Their response is strictly dependent on the amplitude of excitation applied on them. Even though for experimental purposes this is not really significant, in order to make a computational analysis, be it analytical or finite elements, this condition imposes some problems. Therefore it is convenient to describe the dampers with linear modal parameters.

### 4.1 Excitation amplitude and linear modal parameters

The conclusion reached before from the single degree-of-freedom testing was that the natural frequency of the damper varied with the amplitude of the incoming excitation (recall Figure 3-17). It is known that for a linear single degree of freedom system the stiffness and the natural frequency are correlated with the expression:

$$\omega_o = \sqrt{\frac{k}{m}}$$

where  $\omega_o$  is the natural frequency in [rad/s],  $k$  the stiffness coefficient and  $m$  the mass of the system connected to the spring. Therefore with the mass being constant, a measured increase in the natural frequency means that an increase of the stiffness occurred and vice versa. Finally it can be said that the system acts in a less stiff way to a stronger excitation while it appears to be stiffer when the excitation levels are lowered.

From the previously obtained FRFs, magnitude levels of the resonant peaks and the change in the slope of the phase plot suggest a variation of the damping ratio with different excitation levels. As the result of the experience gained from numerous tests, it can be stated that the damping characteristics become more pronounced as the excitation level is increased while the damping is greatly reduced at low levels.

Since all the properties associated to the experimental modal analysis are dependent on the incoming excitation, defining a single linear model describing every possible response of the dampers is not possible. A single model describes only the excitations using which it has been formulated, as described by the diagram below.

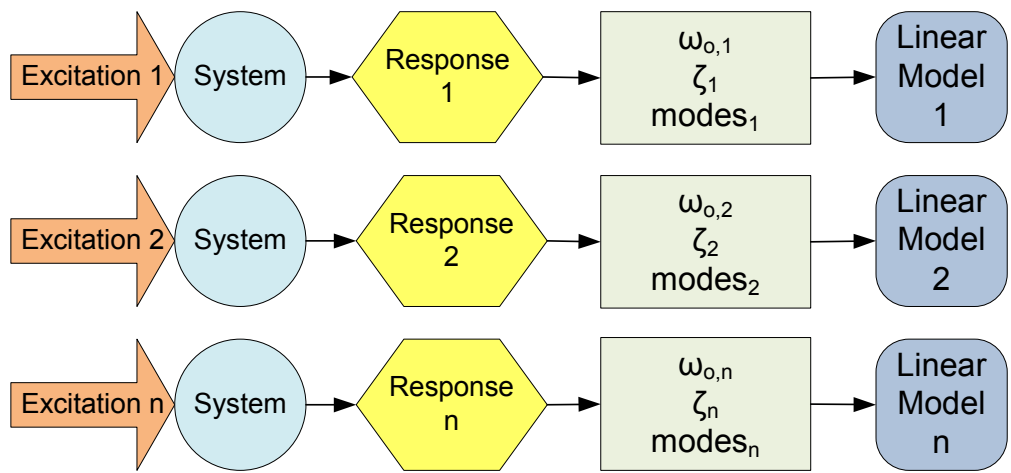


Figure 4-38: Formulation of a linear model with the linear modal parameters valid only for a certain kind of excitation.

## 4.2 Analytical formulation of the test setup

The single damper – single mass test setup is a simple one, aimed at achieving a one degree of freedom system with given mass  $m$ , stiffness coefficient  $k$  and damping coefficient  $c$ . The equivalent system with these properties representing the test setup is shown in Figure 4-39.

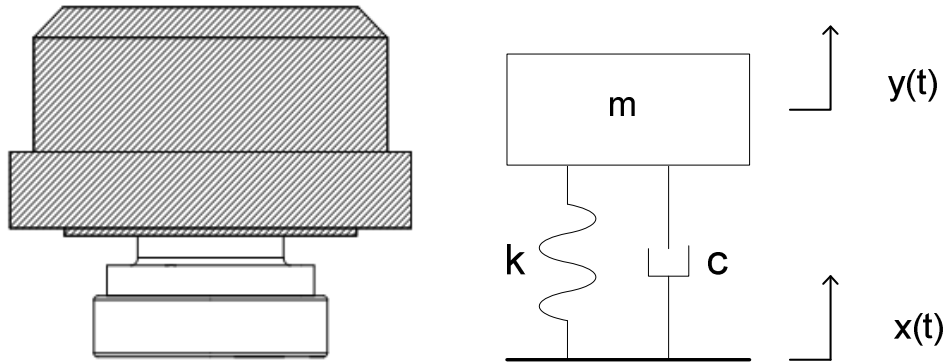


Figure 4-39: The actual damper-mass assembly represented by the linear one degree of freedom system.

Here  $x(t)$  denotes the known displacement of the support while  $y(t)$  denotes the absolute displacement of the mass. The equation of motion governing such a system is then given by <sup>[11]</sup>

$$m\ddot{y} + c\dot{y} + ky = c\dot{x} + kx$$

Then in order to describe a relation between the input and the output of the system, the frequency response must be defined <sup>[12]</sup>

$$H(j\omega) = \frac{Y}{X}$$

To express the frequency response, the time variables are transformed into frequency domain

$$y(t) = Ye^{j\omega t}$$

$$\dot{y}(t) = j\omega Y e^{j\omega t}$$

$$\ddot{y}(t) = -\omega^2 Y e^{j\omega t}$$

$$x(t) = X e^{j\omega t}$$

$$\dot{x}(t) = j\omega X e^{j\omega t}$$

Replacing these into the equation of motion and simplifying

$$m(-\omega^2 Y e^{j\omega t}) + c(j\omega Y e^{j\omega t}) + k(Y e^{j\omega t}) = c(j\omega X e^{j\omega t}) + k(X e^{j\omega t})$$

$$(-\omega^2 m + j\omega c + k) Y e^{j\omega t} = (j\omega c + k) X e^{j\omega t}$$

Finally the frequency response describing the relationship between the input and the output of the system can be written as

$$H(j\omega) = \frac{Y}{X} = \frac{j\omega c + k}{-\omega^2 m + j\omega c + k}$$

The frequency response function is a complex function which can also be described in terms of its magnitude and phase

$$G(\omega) = |H(j\omega)| = \left| \frac{j\omega c + k}{-\omega^2 m + j\omega c + k} \right|$$

$$\varphi(\omega) = \arg(H(j\omega)) = \arg\left(\frac{j\omega c + k}{-\omega^2 m + j\omega c + k}\right)$$

Here  $Y/X$  is calculated as the ratio of the absolute displacement of the mass to displacement of the base. However, multiplying the numerator and denominator of this ratio by  $\omega^2$  shows that  $H(j\omega)$  also represents the ratio of the absolute acceleration of the mass to the acceleration of the base. This result is critical since for all the tests regarding this study, the reference input and the measured output is in terms of acceleration and the Frequency Response Function is calculated using these measurements.

### 4.3 Estimating linear parameters from test data

The single damper one degree-of-freedom tests provide reference stimulus and response acceleration measurements which then can be used to calculate FRFs. These FRFs are useful tools in the extraction of modal parameters from the test data.

The most straightforward method in estimating linear modal parameters is to check for resonance and then use the values around this region to calculate the desired parameters. However, this approach is not always feasible since when strong excitation levels are involved, at the resonance the response becomes dangerously critical and damage to the dampers is probable. Therefore for such tests an alternative approach is used in which the frequencies in a safe region are excited and the dynamic properties are then extrapolated from the measured FRF.

#### 4.3.1 Modal parameters from resonance

If for any test with the single damper, the frequency band of the excitation is large enough to cause the excitation of the natural frequency, resonance occurs. Then this resonance can easily be identified using the Frequency Response Function and the modal parameters can be extracted with this information.

The stiffness coefficient  $k$  [N/m], for the damper for any test is simply given by

$$k = \omega_o^2 m$$

where  $\omega_o$  is the natural frequency in rad/s and  $m$  is the mass in kg connected to the damper.

Below in Figure 4-40 is given the FRF of a sweep sine test at 5g within the frequency band of 20-1000 Hz. An examination of this plot clearly

shows that the damper undergoes resonance between this frequency range.

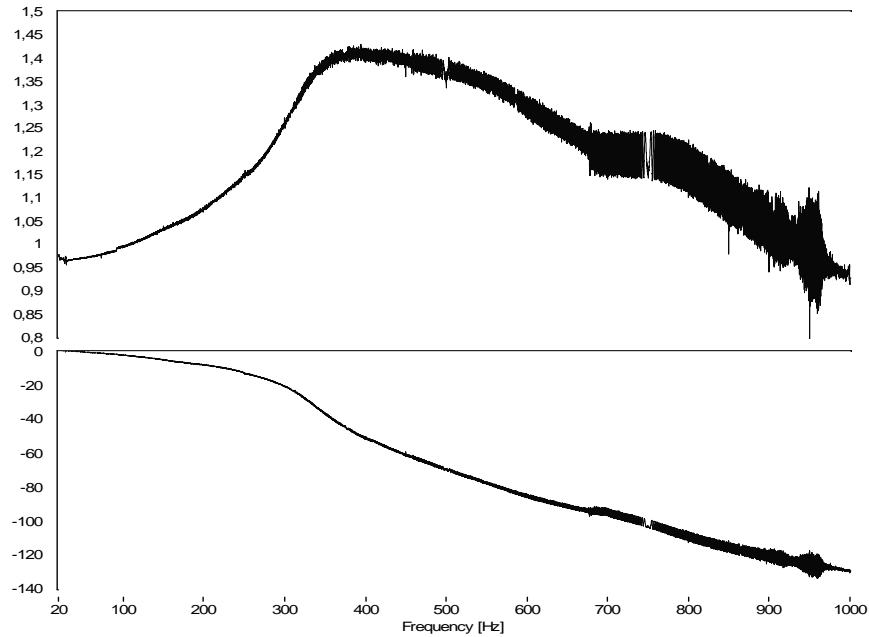


Figure 4-40: Identification of the natural frequency using the FRF from a sweep sine test at 5g.

Then the next step is to identify the modal properties of the damper. This is not so straightforward due to the presence of damping and therefore the resonance is not observed at the  $-90^\circ$  crossing of the phase but is shifted a slightly to lower frequencies.

Previously, a mathematical expression for the FRF was calculated as

$$H(j\omega) = \frac{j\omega c + k}{-\omega^2 m + j\omega c + k}$$

This expression can be arranged written in terms of the damping ratio

$$\zeta = \frac{c}{c_{cr}} = \frac{c}{2\sqrt{km}}$$

$$H(j\omega) = \frac{\omega_0^2 + j2\omega\zeta\omega_0}{(\omega_0^2 - \omega^2) + j2\omega\zeta\omega_0}$$

Now, adjusting  $\omega_0$  and the damping ratio  $\zeta$ , the mathematical model can be tuned to match the FRF calculated from the experimental data given in Figure 4-40. For this purpose, a MATHCAD script is used to iterate for the unknown variables and plot the mathematical function against the experimental FRF given above (details of this script can be found in Appendix A).

Investigating the experimental FRF and making several iterations with the model, the following parameters can be chosen,

$$f_0 = 450 \text{ Hz}$$

$$\zeta = 0.4$$

The mathematical model with the chosen parameters results in the FRF plot given below in Figure 4-41.

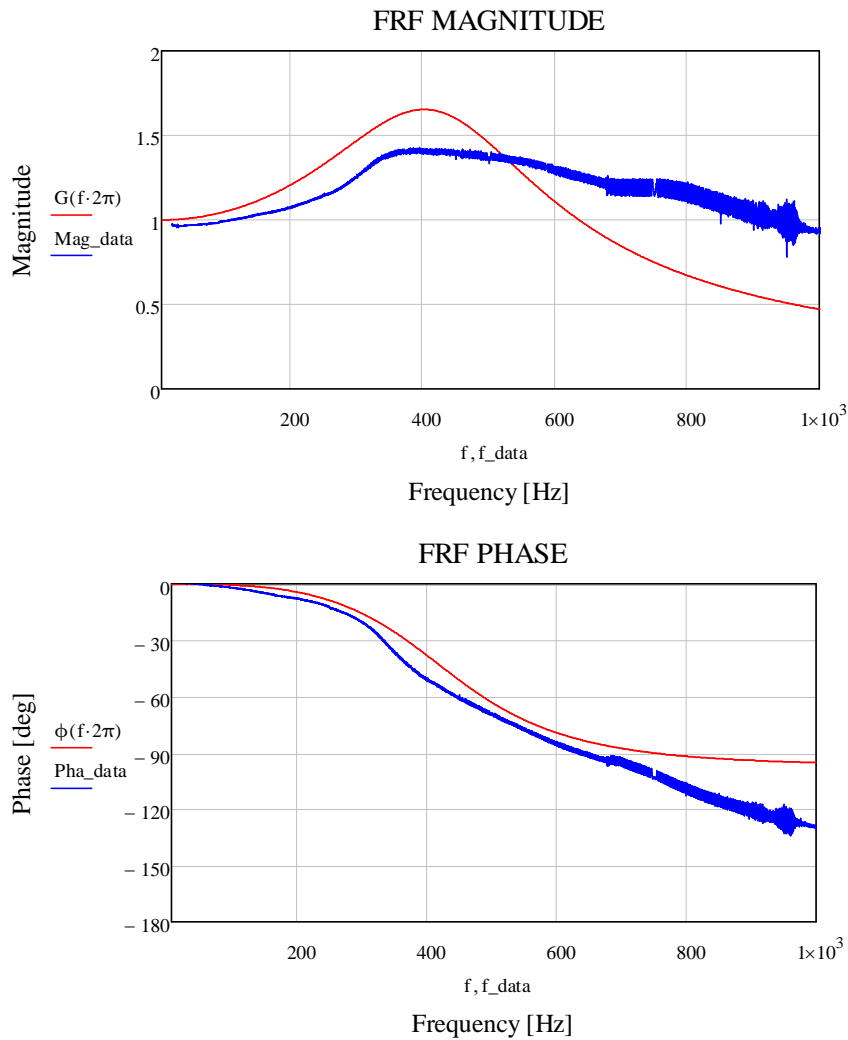


Figure 4-41: FRF Magnitude and Phase plots comparing the mathematical model (red) to the test results (blue).

Comparing the plotted mathematical model to the measured FRF, it can be concluded that the estimated modal parameters are representative of the system and from here, the stiffness coefficient can be calculated as

$$k = \omega_o^2 m = 2.8 \times 10^6 N/m$$

### 4.3.2 Extracting modal parameters by curve fitting

If due to the large acceleration imposed, exciting the natural frequency of the system is not possible, then this problem can be worked around by exciting the frequency band lower than the natural frequency and then using the mathematical model to extrapolate the rest of the response.

Below in Figure 4-42 is given an FRF of a single damper testing with a 20g sweep sine, a rather high level of excitation, within the frequency range 20-100 Hz.

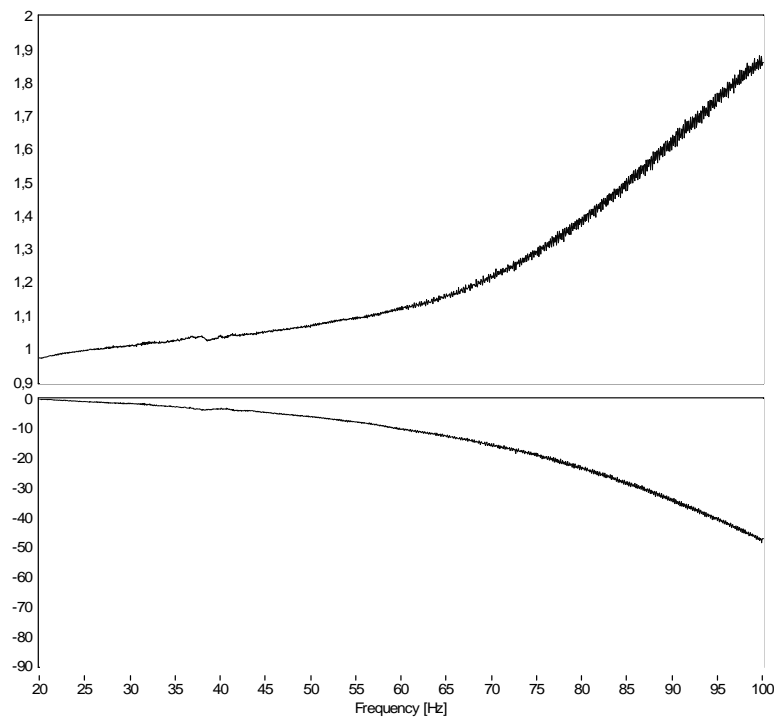


Figure 4-42: FRF from 20g sweep sine test of a damper in Config 3.

It is apparent from this plot that the damper does not undergo resonance and the natural frequency of the system is surely higher than 100 Hz. Then a solution of the modal parameters must be reached fitting the acquired data to the mathematical model given as

$$H(j\omega) = \frac{\omega_0^2 + j2\omega\zeta\omega_0}{(\omega_0^2 - \omega^2) + j2\omega\zeta\omega_0}$$

At 100 Hz, the experimental FRF has the following values:

$$|H(j2\pi 100)| = 1.9$$

$$\arg(H(j2\pi 100)) = -50^\circ$$

Using these two conditions, the mathematical model can be solved for the modal properties utilizing the MATHCAD script (see Appendix A). The script returns the following parameters as the result of the mathematical model:

$$f_0 = \frac{\omega_0}{2\pi} = 105 \text{ Hz}$$

$$\zeta = 0.32$$

$$k = \omega_0^2 m = 1.5 \times 10^5 \text{ N/m}$$

Then the frequency response of the mathematical model can be plotted together with the experimental FRF in order to compare the validity of such an approach.

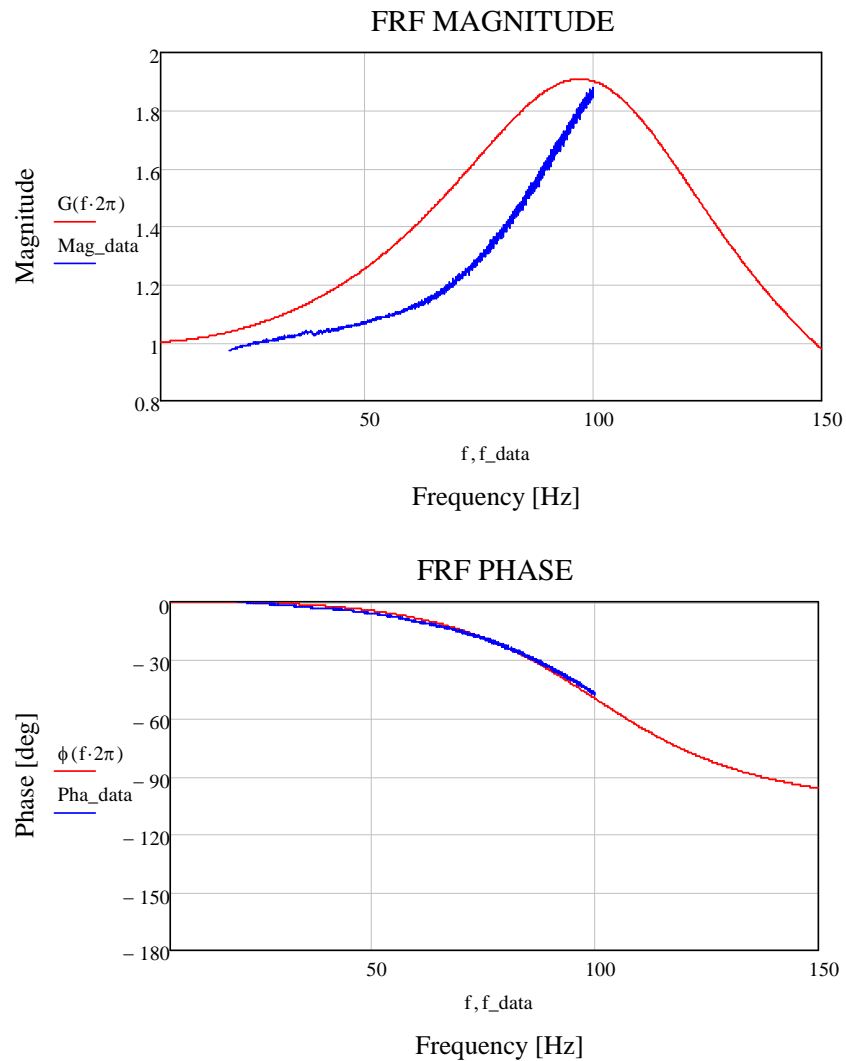


Figure 4-43: Comparison of the mathematical frequency response function (red) and the experimental FRF (blue).

Investigating these two plots it can be seen that there is an almost perfect representation of the FRF phase by the mathematical model while it acts poorly for the FRF Magnitude. Using just a single data point of the experimental FRF for the construction of the whole curve is therefore inefficient. To overcome this problem an adjustment of the

modal parameters can be performed to achieve a better curve fit. Starting from the previously calculated set of modal parameters and gradually adjusting them, the following fit can be obtained

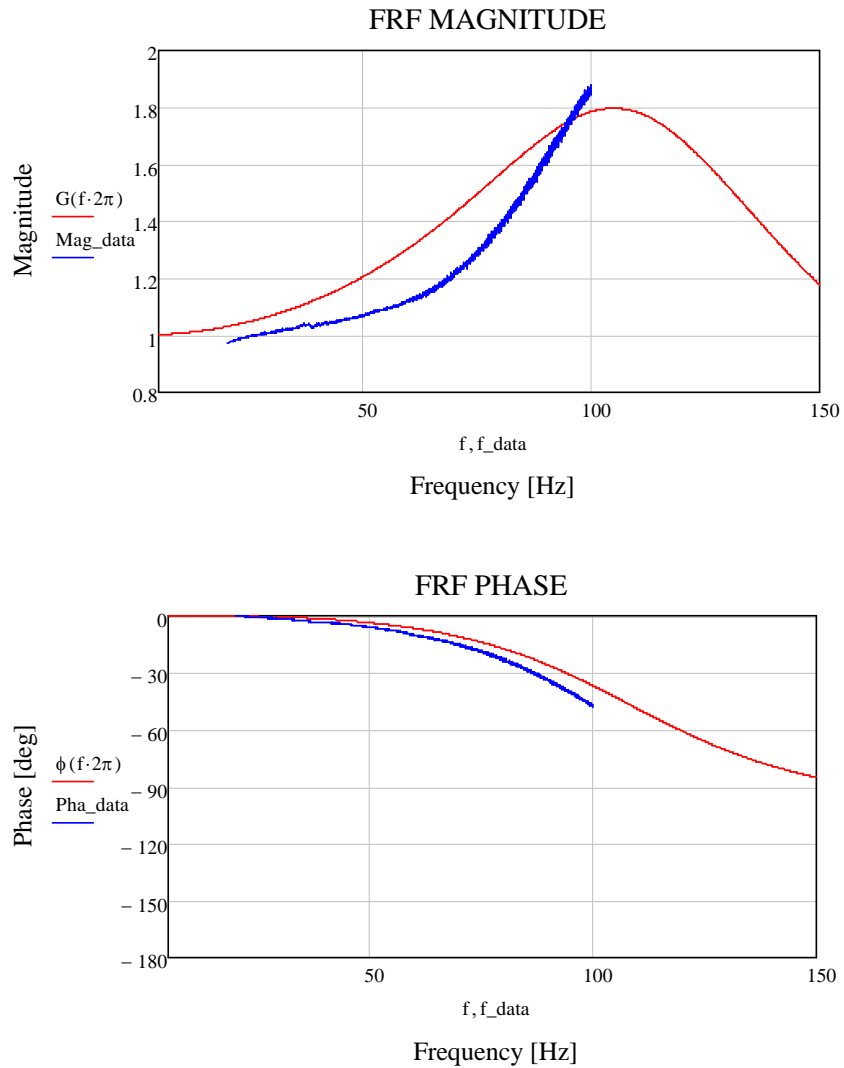


Figure 4-44: The mathematical FRF fit with the adjusted modal parameters with the following parameters

$$f_0 = 115 \text{ Hz}$$

$$\zeta = 0.35$$

and the stiffness coefficient can be estimated as

$$k = \omega_0^2 m = 1.8 \times 10^5 \text{ N/m}$$

After the suggested adjustment of the parameters, it is seen that the mathematically estimated system represents the experimental results more or less accurately in the excited region and moreover it gives a rough estimation of the region beyond it. The maximum deviation in the magnitude plot between the model and the experimental data points is calculated as 0.2 and for the phase plot this value is  $11^\circ$ , which are acceptable results.

#### **4.4 Estimating torsional properties from test data**

Besides the translational properties affecting the dampers, there is also a rotational motion in particular at the tip of the damper that somewhat originates from the very small deformations in the axial and the radial directions (see Figure 4-45).

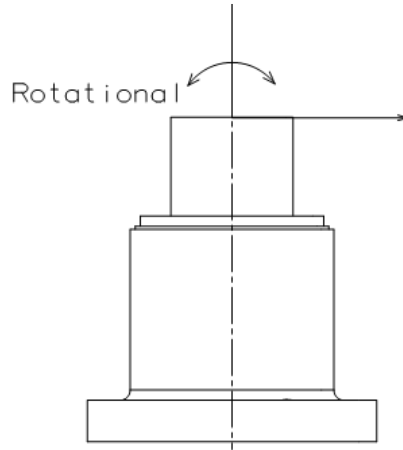


Figure 4-45: The rotational motion at the tip of the damper.

There is a rotational stiffness coefficient associated with this motion in units of [Nm/rad] and it must be numerically defined to achieve a complete model of the system together with the axial and the radial stiffnesses.

The presence of a torsional deformation at the tip of the damper was noted in most of the single degree of freedom test results. When performing various tests on the single damper in the axial loading configuration, a constantly appearing phenomenon was observed in most of the FRFs in which there has been a short period of phase shift between the accelerometers oriented in the same direction with a certain offset (see Figure 4-46, Figure 4-47).

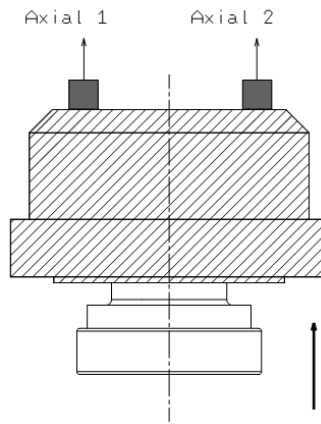


Figure 4-46: Accelerometer configuration for an axial low level sweep sine test.

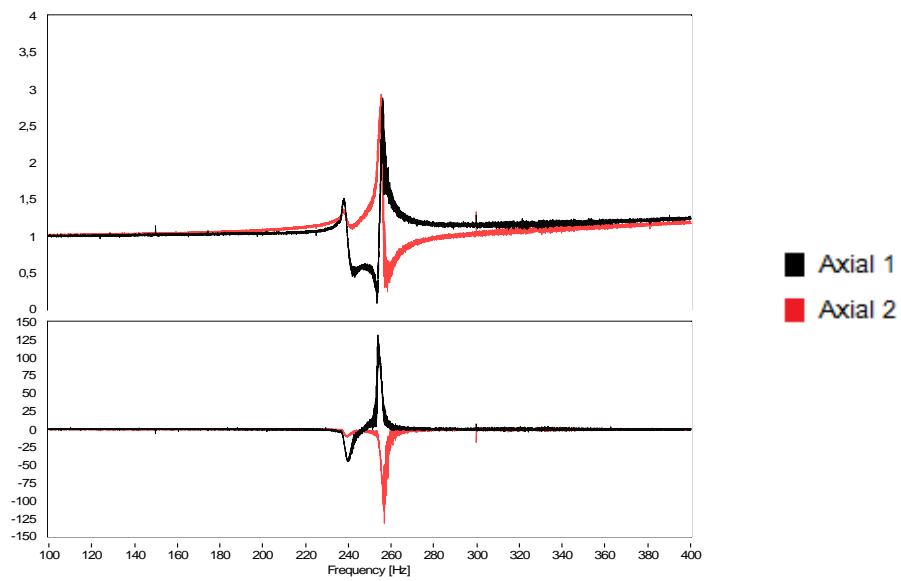


Figure 4-47: Low level sweep sine FRF in the region of the rotational resonance of the damper.

The spontaneous opposite phase shift of the axial accelerometers suggests a resonance due to a rotation at the damper tip, a deformation associated with the torsional stiffness parameter.

The torsional stiffness could be accurately determined if the eccentricity of the mass was known however, investigating the response to a 0.5g constant level loading FRF given in Figure 4-47, the torsional resonance is observed around 250 Hz. This value will be tremendously lower when the testing is performed at the actual test loading (20g), suggesting a very low torsional stiffness. The parameter is in practice of no interest for the modeling of the damper so, no additional effort was made to determine it.

## **4.5 Estimated properties of the final damper configuration**

Based on the experiences gained from the numerous single damper experiments, a final tuning and configuration of the damper was achieved, which was described in detail in the previous chapter. In order to model the behavior of the dummy mockup, the complete spring-like properties of the dampers have to be estimated, in the same manner discussed throughout this chapter.

### **4.5.1 Axial stiffness coefficient, $k_1$**

The axial stiffness coefficient is the property associated to the resistance of the damper to the deformations purely along its axis. The FRF plot of the axial sweep sine test at 20g suggested a natural frequency as

$$f_0 = 300 \text{ Hz}$$

Then the axial stiffness can be estimated as

$$k_1 = (2\pi f_0)^2 \cdot m = 1.24 \times 10^6 \text{ N/m}$$

#### 4.5.2 Radial stiffness coefficients, $k_2$ & $k_3$

The radial stiffness coefficient in the two transversal directions  $k_2$  &  $k_3$  correspond to translational deformations that are perpendicular to the damper's axis. The FRF plot of the transversal sweep sine test at 20g evidenced a natural frequency associated to the radial deformation mode as

$$f_0 = 350 \text{ Hz}$$

Then the radial stiffness coefficient becomes

$$k_{2,3} = (2\pi f_0)^2 \cdot m = 1.70 \times 10^6 \text{ N/m}$$

#### 4.5.3 Rotational stiffness coefficient, $k_{\theta,1}$

The dampers are free to rotate around their own axis, therefore there is no such stiffness regarding this motion. It is taken as 0, whenever it is deemed necessary.

#### 4.5.4 Rotational stiffness coefficients $k_{\theta,2}$ & $k_{\theta,3}$

For the purposes of modeling of the system, the torsional stiffness of the dampers are taken as

$$k_{\theta,2,3} \cong 250 \text{ Nm/rad}$$

This is an estimated value that is tuned and verified through the computational model and further mockup tests that will be described in detail in the following chapters.

## 4.6 Results & Discussion

The dynamic material properties of the dampers had to be described numerically in order to be used in an analytical or a Finite Elements model. With the help of the experimental modal analysis techniques, the modal parameters are extracted from the test data in terms of natural frequencies, damping ratios and mode shapes. From these modal parameters, the necessary stiffness coefficients are estimated using a suitable analytical model and mathematical formulas. The results of this procedure is summarized in Table 4-8 below

Table 4-8: Summary of the stiffness coefficients estimated for the final damper configuration.

Axial Stiffness, $k_1$	$1.24 \times 10^6$ N/m
Radial Stiffness, $k_2$	$1.70 \times 10^6$ N/m
Radial Stiffness, $k_3$	$1.70 \times 10^6$ N/m

At the end of all the single degree-of-freedom tests and the subsequent calculations, some very useful results are obtained regarding the characterization of the dampers. These results provide valuable insight and are crucial for the construction of the Finite Elements model which will be described in detail in the following chapter.

# Chapter 5: Finite Element Analysis of the Damper – Mockup system

## 5.1 The need for a Finite Elements Analysis

Even though experimental methods are accurate and reliable for the study of the dynamics of a system, they also come with certain restrictions that foster the use of computational methods along with them. As far as the shaker tests of this work are concerned, a comparison of the advantages and the disadvantages of the Experimental methods to the computational ones are given in the table below.

Table 5-9: Comparison of the advantages and the disadvantages involved in experimental methods of a shaker test to those of Finite Elements methods.

Experimental Methods	Finite Element Methods
Fast and accurate results	Accuracy depends on the complexity and the validity of the model
Requires a data processing stage before meaningful results can be extracted	Results are immediately clear and visually appealing
Long setup change time, slow modification of test parameters	Once the FE model is created, allows quick changing of parameters
Repeated testing may cause the damaging of the setup resulting in time and economic losses	There is no limit to the number of runs that can be performed. No risk of damage.

Such a comparison obviously exhibits the necessity of a Finite Elements Model to be used together with the experiments, exchanging useful information between them whenever possible.

## 5.2 Verification of the structural modes of the mockup using FEM

Before including the dampers in the Finite Elements model, the mockup structure should be checked in terms of its natural frequencies. This is to assure that the deformation modes of the mockup are much higher than the modes of the system when the three dampers are included. In this way, it can be stated that the mockup is behaving in the region of interest as an ideal rigid body.

### 5.2.1 Finite Element Modeling

In Chapter 2, the mockup to replace the actual MIMA for testing purposes was modeled and assembled in CATIA. This CAD model (see Figure 5-48) is identical to the mockup and therefore can be utilized for the Finite Element Analysis using the Generative Structural Analysis module of CATIA V5.

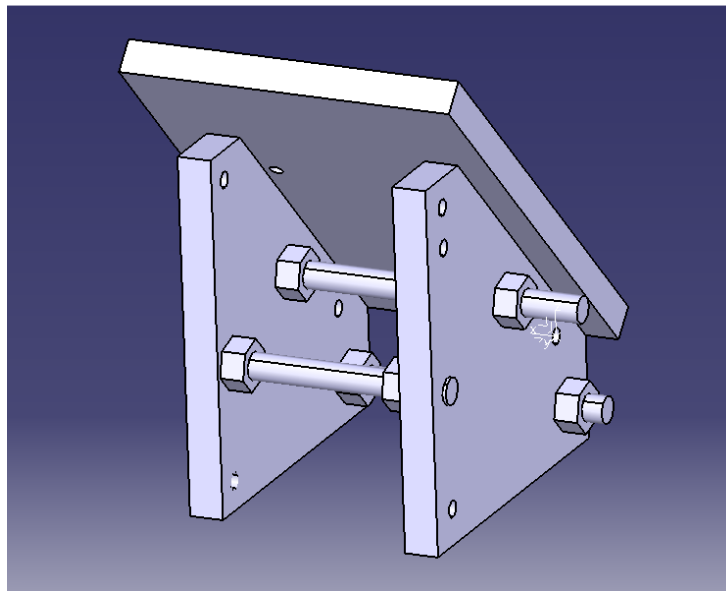


Figure 5-48: The CAD mockup assembled in CATIA.

The first step, once the CAD model is imported into the Generative Structural Analysis, is to define the connections of the various components making up the mockup assembly. This is done using General Analysis Connections in CATIA. Once all the necessary connections are defined, the model looks as depicted in the following figure:

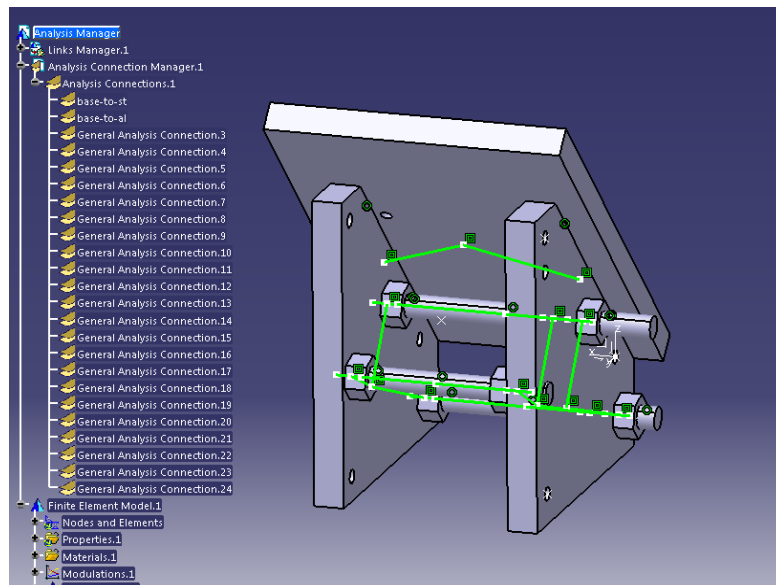


Figure 5-49: Mockup CAD model with the necessary connections defined.

The next step is to define the nature of the connection properties. This function allows the user to define how the different components of the assembly are fixed together. As far as the mockup is concerned, the connections are Fastened Connections.

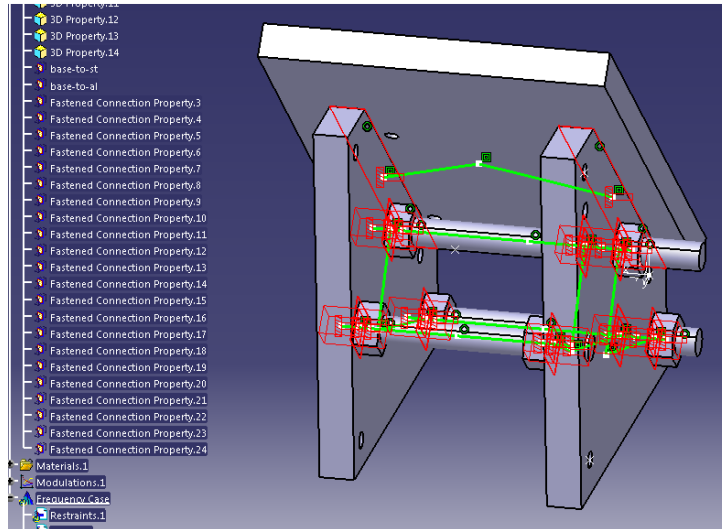


Figure 5-50: The model with fastened connection properties defined between the different components.

Once all the connections are defined between the components making up the mockup assembly, the model is ready to be meshed and computed.

### 5.2.2 Meshing

There are several factors that require special attention for the meshing of the model. The first is the type of Finite Element to be used for the meshing. Here, the simplest element, the Linear Tetrahedron is used (see Figure 5-51).

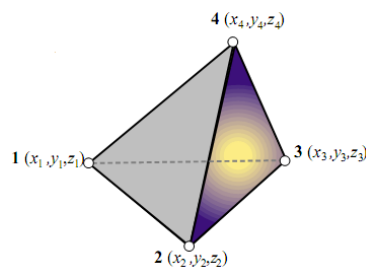


Figure 5-51: The linear tetrahedron. Its geometry is fully defined by giving the location of the four corner nodes with respect to the global coordinate system. [13]

Another important property of the mesh is the element size. This parameter sets the overall size of a single finite element and therefore directly affects the number of elements and the number of nodes in a mesh. Increasing the number of nodes in a mesh may result in more accurate results while on the other hand increasing the computation time significantly. Below in Figure 5-52 are demonstrated two the meshes, a course mesh with large element size and a fine one with smaller elements.

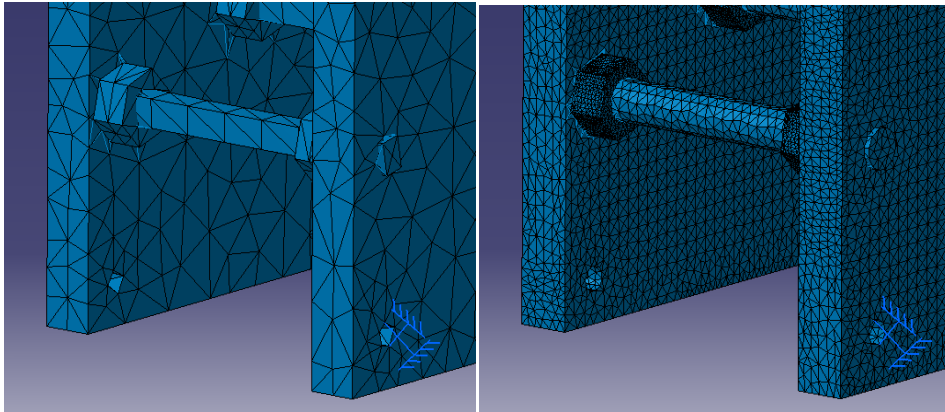


Figure 5-52: A course mesh compared to a fine mesh.

Once the meshing procedure is completed, the governing equations of the FE model can be computed to achieve the desired results.

### 5.2.3 Results and discussion

As previously discussed, the meshing done on the model can directly influence the results. Therefore it is a common approach to perform several computations gradually increasing the number of finite elements, i.e. using a finer mesh, until a single solution is converged. The decision on when to stop can be made by comparing the results of each iteration and checking the relative error between them. When the

percentage difference falls below a certain criteria, the mesh is said to be good enough and the results are assumed accurate.

The when performing the FEM analysis of the structural modes of the mockup, this same method is used. To start with, large finite elements are used (size 9mm) resulting in a course mesh. Then the mesh is made finer and finer until convergence to a single result occurs. The results of this procedure are summarized in Table 5-2 below.

Table 5-10: Summary of the results of the FEM analysis for the structural modes of the mockup.

Mode	Element type	Size [mm]	Nodes	Elements	Modes	Frequency [Hz]	Computation Time [s]
1	Linear Tetrahedron	9	2555	8238	1	805	7
					2	1205	
2	Linear Tetrahedron	7	3158	10262	1	751	10
					2	1112	
3	Linear Tetrahedron	5	5291	17806	1	689	14
					2	1007	
4	Linear Tetrahedron	3	20527	82636	1	601	53
					2	875	
5	Linear Tetrahedron	2	44446	178817	1	570	149
					2	832	
6	Linear Tetrahedron	1	203434	909090	1	561	1323
					2	804	

As it can be seen from the above table, the computation time increases significantly as the element size is decreased beyond a certain value. Therefore a mesh that is acceptable both in terms of accuracy and computation time must be selected. Mesh 5 is such a mesh with only a 1.5% of relative error in terms of the change in the first natural frequency compared to Mesh 6. Therefore it is said to be an optimum mesh with accurate results.

The computed structural modes of vibration of the mockup are given in the figure below.

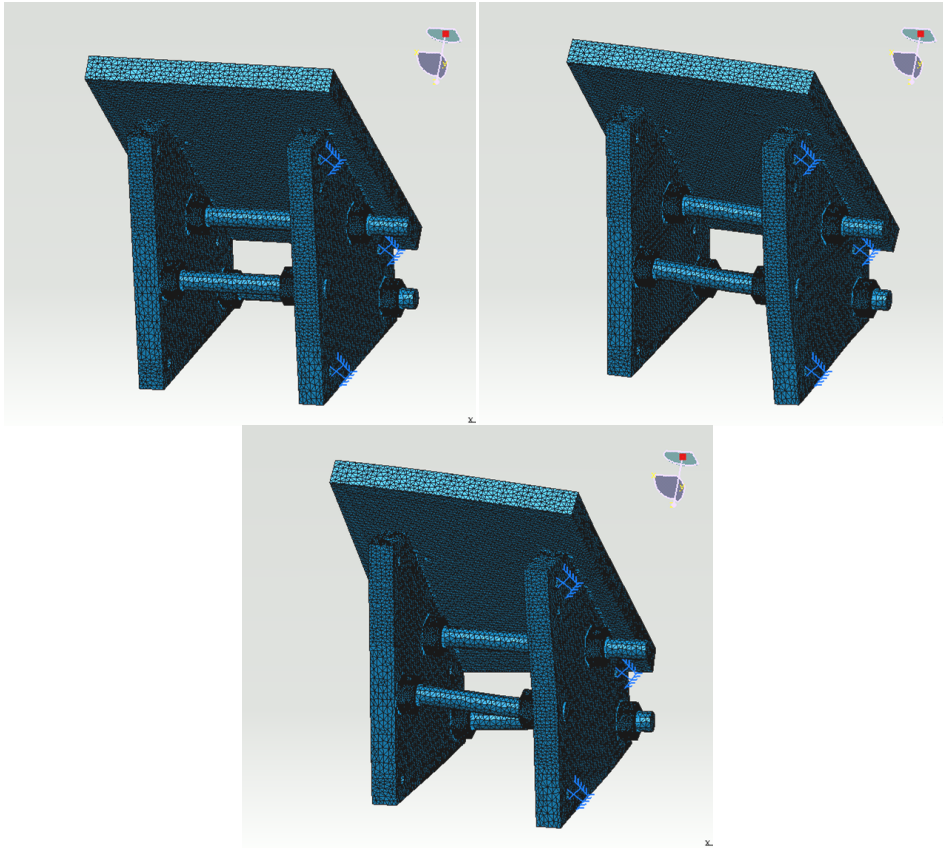


Figure 5-53: Structural modes of vibration of the mockup. (a) Undeformed mesh (b) first mode at 570 Hz (c) second mode at 830 Hz.

The FEM analysis of the mockup suggest that the first structural resonance of the mockup is quite high (above 550 Hz) with respect to the frequency band of interest for the actual mockup testing. The vibration modes related to the deformation of the dampers are expected to be around 100 – 200 Hz and so the structural deformations of the mockup should not interfere with these modes. Therefore at the end of the FEM analysis, the conclusion that the mockup is satisfactory for experimental purposes can be reached.

### 5.3 Analysis of the Damper-Mockup system using linear spring elements

The actual MIMA instrument is mounted on three dampers that are fixed at designated locations. The mockup that was designed inertially identical to the instrument requires a similar assembly for experimentation and such a test setup can be modeled as a Finite Elements model before any real experimentation is performed.

#### 5.3.1 Modeling of the dampers as spring elements

Since the mockup itself was already modeled in the previous section, here an appropriate representation of the dampers in the model must be defined. Considering that only the natural properties of the system is of interest, the dampers can be modeled as springs connected at the designated locations on the mockup. Rigid Spring Virtual Part feature of CATIA is used to model three springs with given stiffness coefficients as shown in Figure 5-54.

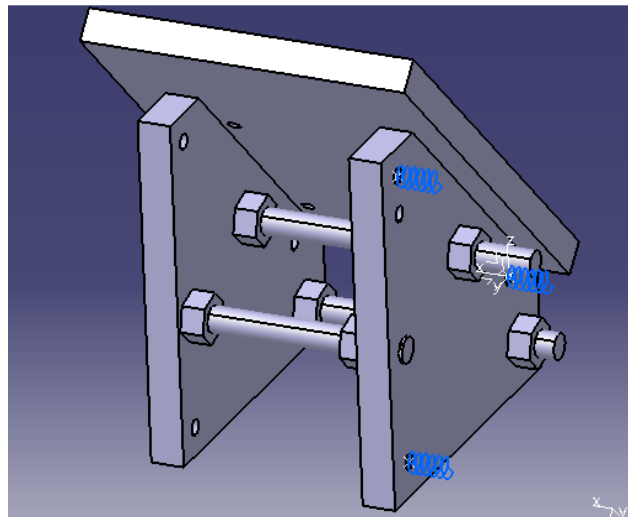


Figure 5-54: Spring Virtual Parts connected at three point on the mockup.

As far as the boundary conditions are concerned, this time it is the dampers that must be restraint. Therefore all the three Virtual Spring elements are clamped (see Figure 5-55).

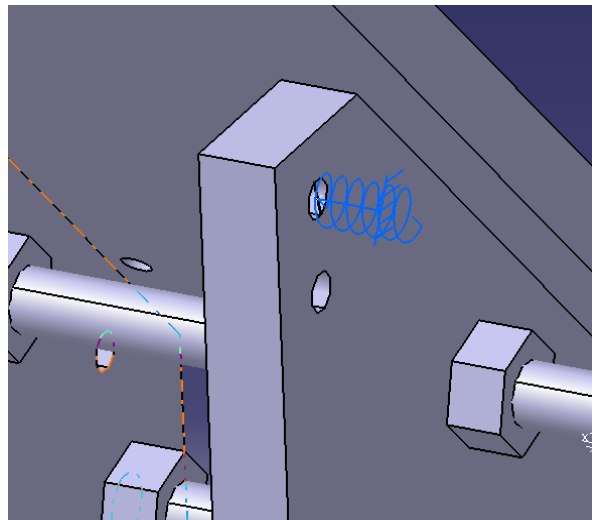


Figure 5-55: Clamped boundary condition for the spring elements.

### 5.3.2 Defining Virtual Spring stiffness coefficients

The Virtual Spring Parts have a set of directional stiffness coefficients that must be defined before any computation can be made. Here, in order to analyze the behavior of the system with the damper at their ultimate configuration and tuning, the estimated stiffness parameters of Chapter 4 are used. These stiffness properties are defined for all the three dampers as shown in the below figure.

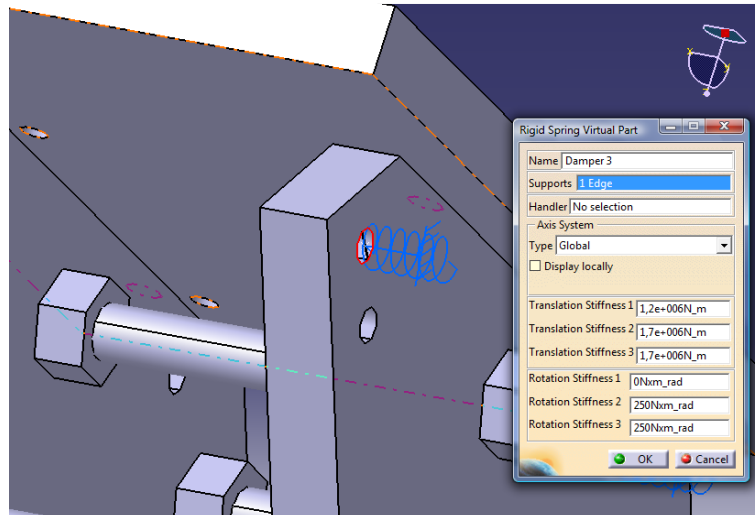


Figure 5-56: Stiffness coefficients estimated from single degree of freedom tests defined for the virtual spring parts.

Once all three dampers are defined in this manner, the model is defined completely and using the optimum mesh parameters of the previous section, computations can be performed.

### 5.3.3 Resulting behavior of the system

There are several important results that can be obtained from this analysis including the natural frequencies and the modes of vibration of the system.

#### 5.3.3.1 Natural frequencies

The computed first three natural frequencies of the system are reported as follows

Table 5-11: Natural frequencies of the system corresponding to the first three modes of vibration.

Mode	Natural frequency [Hz]
1)	131
2)	151
3)	264

Here only the first three natural frequencies are given since the remaining ones are of a much higher frequency and correspond to trivial modes not significant for the scope of this analysis.

### ***5.3.3.2 Mode shapes***

Besides the natural frequencies of the model, the mode shapes at these frequencies require special attention. A visualization of the first three modes of the whole system is given in the next page.

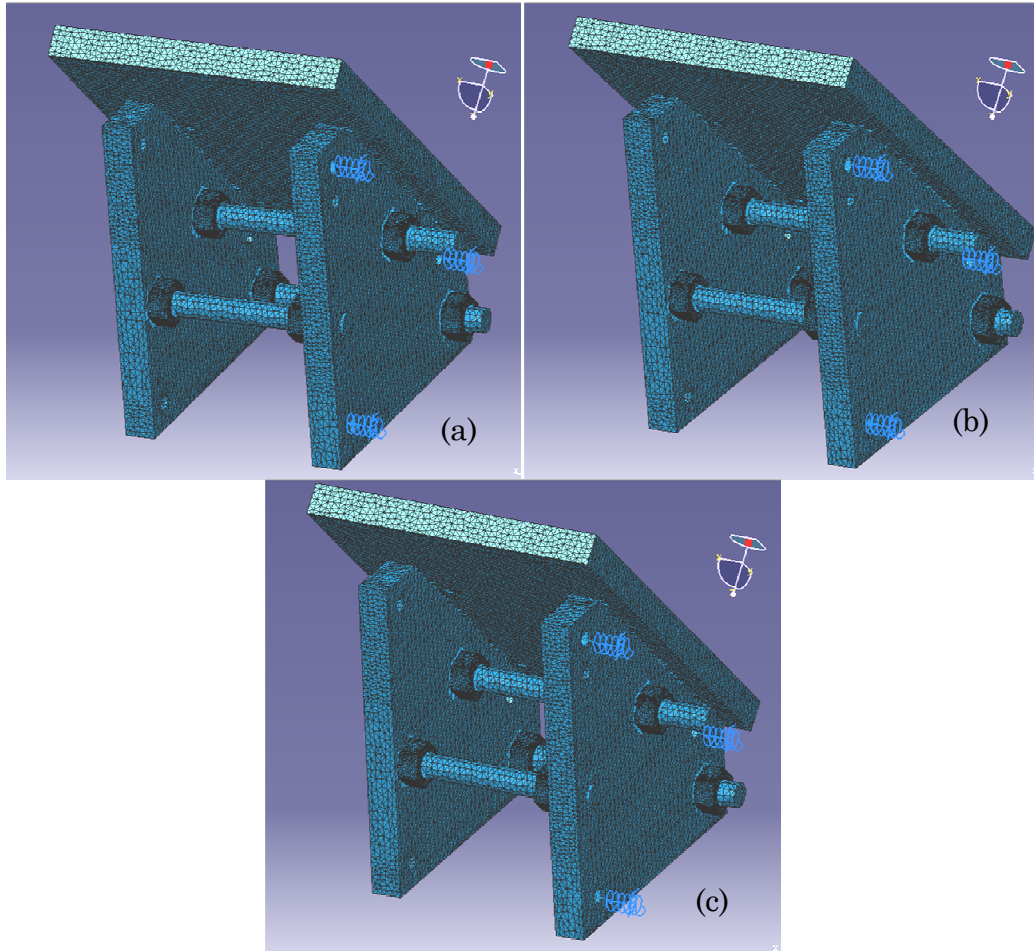


Figure 5-57: First three modes of vibration at (a) 131 Hz (b) 151 Hz (c) 264 Hz.

A close investigation of Figure 5-57 reveals some important information about the nature of these modes. The first two modes at low frequency exhibit a rotational motion of the mockup while the third higher frequency mode seems to be almost purely translational.

The rotational mode at low frequencies is primarily due to the out-of-phase axial deformation of the spring elements. This phenomenon results in a rotation axis on the vertical mockup plate where there is almost no displacement. This axes around which the mockup rotates can be better visualized from the Translational Displacement Vector plot.

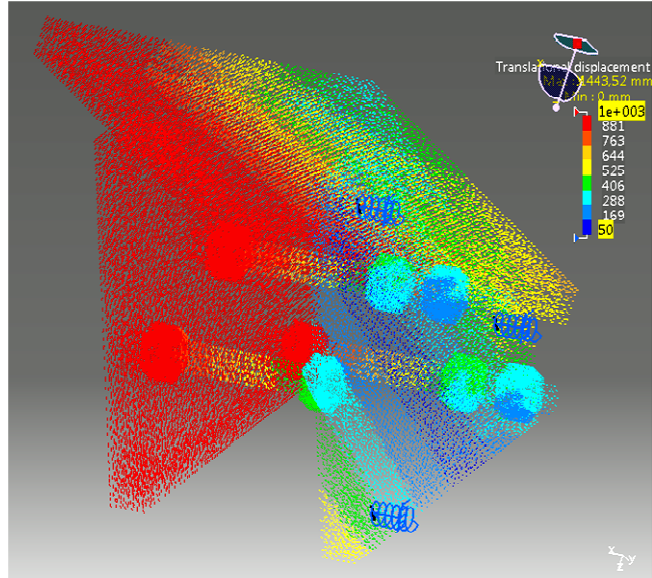


Figure 5-58: Displacement Vector plot of the vibration mode 1 at 131 Hz.

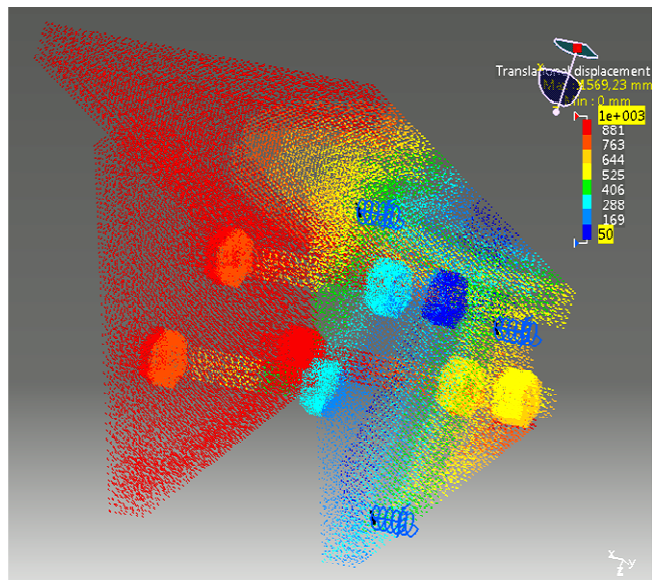


Figure 5-59: Displacement Vector plot of the vibration mode 2 at 151 Hz.

In these plots, there is a clear region (in shades of blue) where there is almost no displacement while the areas on the opposite sides of this line display large displacements. This fact proves the existence of a rotational axis passing through this region. These rotational axes for the first two modes are schematically illustrated below in Figure 5-60.

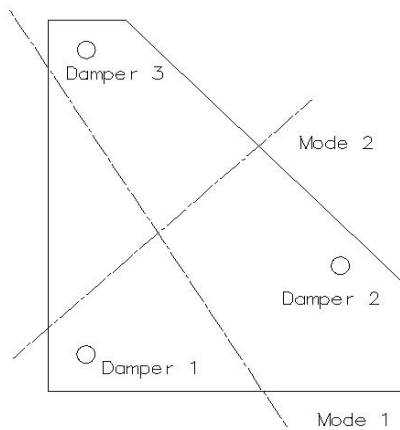


Figure 5-60: The axes of rotation for the first two modes of vibration.

Being this the case for the first two modes, the high frequency third mode results from the in-phase deformation of the spring elements producing an almost purely translational motion (see Figure 5-61).

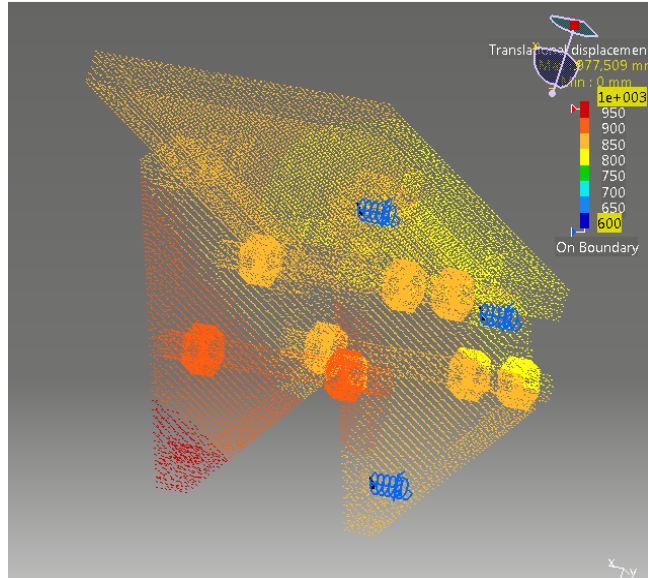


Figure 5-61: Displacement Vector plot of the vibration mode 3 at 264 Hz.

### 5.3.4 Evaluation of the results for the ultimate damper configuration

The FEM analysis of the system with the damper properties estimated previously was performed and the returned results are positive in terms of several aspects. To start with, there are no natural frequencies of the damper-mockup assembly below 100 Hz. Furthermore, the first three modes that are of interest do not occur at very high frequencies. These are favorable results as far as the environmental conditions of the MIMA are concerned.

As predicted, the first modes of vibration are rotations around a certain axis. This expectation can be supported by comparing the COG position of the mockup to the center of the Damper Moment Triangle, as shown in Figure 5-62. The COG position is shifted due to the presence of the perpendicular plate. In fact when superimposed, the rotational axes of the first two modes intersect close to this center of moments, which is a result of these two mentioned points not being coincident.

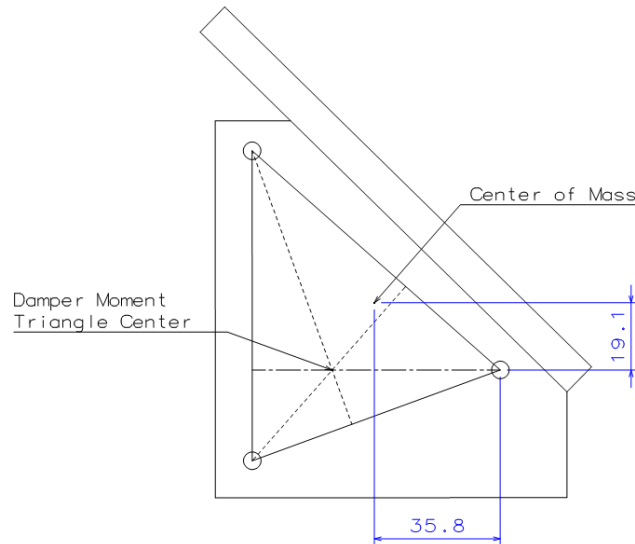


Figure 5-62: Mockup COG position vs. Damper Triangle Moment Center.

Unlike the first two, a third mode is observed at a higher frequency which is almost purely translational in shape.

Considering all these results of the FEM analysis, the damper tuning performed through the single DOF tests leads to an acceptable dynamic behavior on the dummy mockup.

## 5.4 Results and discussion

In this chapter, Finite Element Modeling techniques were used since having a computational model alongside an experimental study has numerous advantages, including the ease of parametric modifications, visually appealing results and the elimination of failure risks.

As a first task, the mockup that was designed and manufactured for testing purposes was verified in terms of its structural vibration modes. Since the resonant deformations of the mockup did not occur until above

550 Hz, a frequency which is representative of the MIMA behavior if fully constrained.

Furthermore the complete test setup with the damper-mockup assembly was modeled and analyzed with the estimated stiffness properties of the ultimate damper configuration. The resulting natural frequencies and mode shapes were investigated and found to be acceptable when compared to the environmental requirements.

Besides providing foresight for the mockup testing procedures, the Finite Elements Model also has the purpose of giving tuning feedback for the dampers. If a certain behavior of the FE model is stated, then the stiffness parameters that produce this behavior is attempted to be achieved using the previously described damper tuning methods. This is a valuable tool for the mode optimization of the system and is utilized many times during this study.

# Chapter 6: Testing of the dummy model

The MIMA instrument will be mounted through three dampers to the rover. The dampers have the task of isolating and reducing the transmitted vibrations arising during the launch and landing phases. In this part of the study, a suitable shaker test setup and procedures were designed to simulate the vibration environments expected at the instrument-rover interface. The dummy mockup was designed and described in chapter 2; it is used to represent the actual MIMA in these tests to avoid any risk of damaging due to repeated testing. The previously tuned and evaluated dampers are used to constraint the mockup and reduce the transmitted vibrations.

## 6.1 Test methodology

Considering the environmental conditions of the MIMA instrument given in Chapter 1, appropriate testing procedures are designed and applied for the damper-mockup assembly in order to analyze its behavior.

### 6.1.1 Test setup

Having studied the environmental conditions, it is apparent that all three axes of the mockup need to be tested separately. Therefore three different test setups are utilized to evaluate the three different directional behaviors of the system as notated below in Figure 6-63.

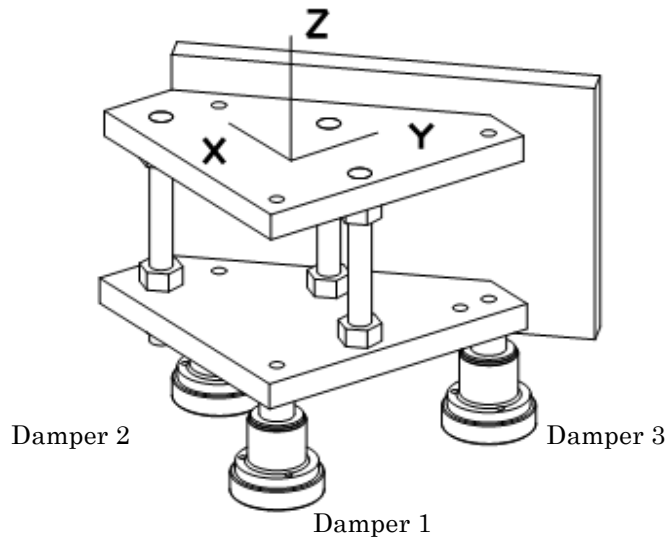


Figure 6-63: The three testing directions shown on the mockup and damper designations.

All the tests use a similar signal acquisition and processing layout schematically described in Figure 6-64.

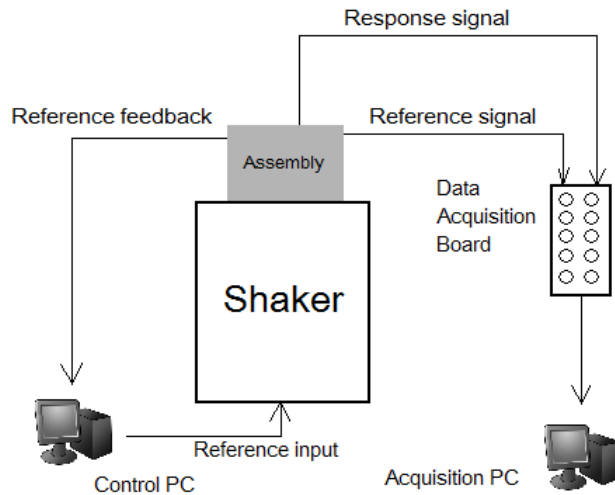


Figure 6-64: Signal acquisition and feed schematics for the dummy model testing.

#### **6.1.1.1 Z axis**

The Z axis testing primarily includes the axial excitation of the dampers supporting the mockup. A typical test setup used for this axis is given below in Figure 6-65.

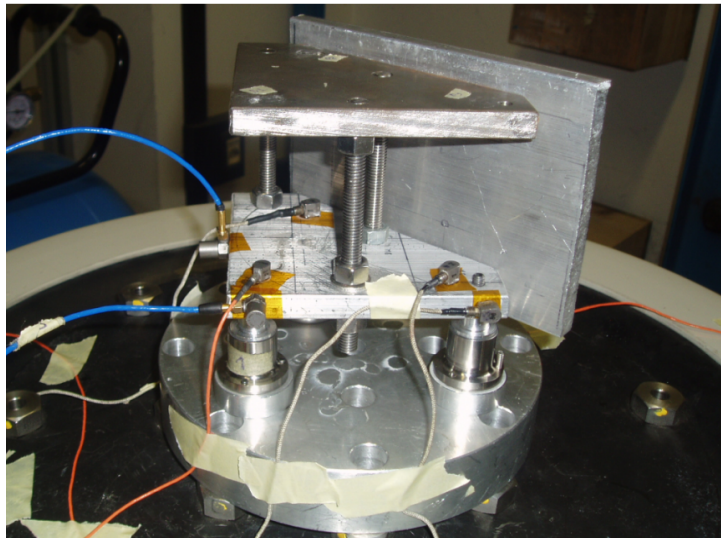


Figure 6-65: Z axis testing setup with the accelerometer positions.

As seen in the above figure, several accelerometers are utilized for the complete measurement of the stimulus and the response. Similar to the single damper-mass test setup, one accelerometer is used to measure the reference input and feed it back to the control PC and one accelerometer is used to measure this same reference for storage. At least three accelerometers are mounted immediately above each damper to measure the response of the mockup, However it is reasonable to include more accelerometers facing other directions to check for some transversal vibrations of the mockup.

### **6.1.1.2 X axis**

In X axis testing, the dampers are mainly excited in the transversal direction, therefore the damper-mockup assembly must be rotated with respect to the excitation direction of the shaker. A large metallic cube is used for this purpose as shown in Figure 6-66.

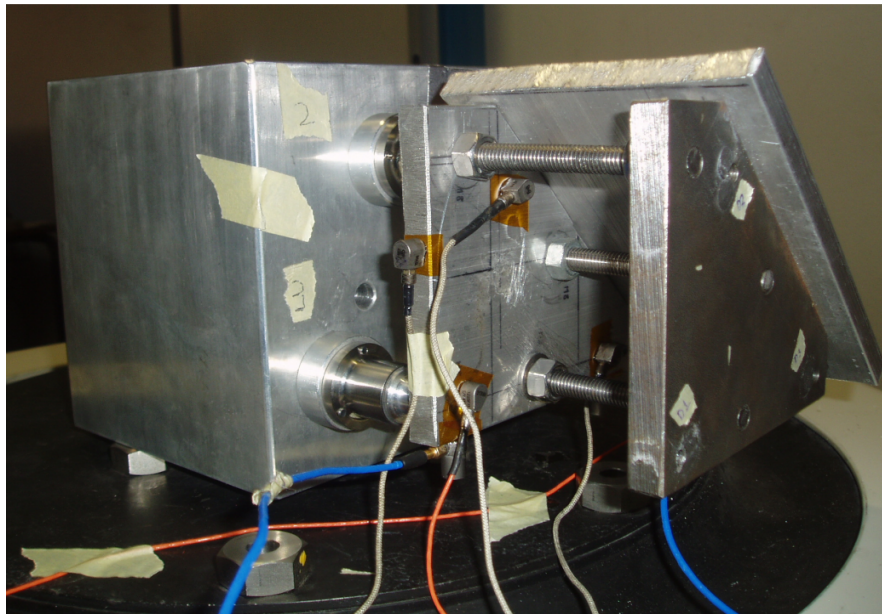


Figure 6-66: X axis testing setup with the accelerometer positions.

Similar to the Z axis testing, two accelerometers are used to measure the reference excitation, one for control and one for storage and further analysis. Three accelerometers facing the horizontal are used to measure the axial deformation responses of the dampers. Others measure the accelerations of the mockup in the direction of excitation and also the out-of-plane vibrations.

### **6.1.1.3 Y axis**

The Y axis mockup testing is very similar to the X axis testing with the only difference being a 90° rotation of the mockup. The dampers are again stressed in the transversal direction (see Figure 6-67).

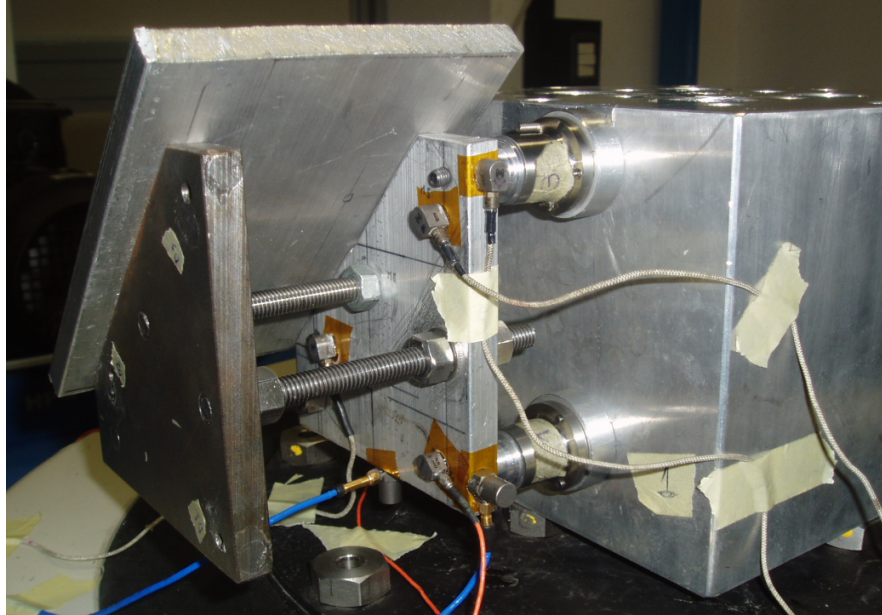


Figure 6-67: Y axis testing setup with accelerometer positions.

The configuration of the accelerometers is more or less the same as the previously described test setup with enough attention paid to having enough of them for a complete understanding of the system behavior.

### **6.1.2 Reference stimulus**

For the testing of the mockup, some well-defined reference excitations are required. These given excitation profiles are generated as signals using the Control PC and are realized by the shaker as vibrations.

#### ***6.1.2.1 Resonance search***

The resonance search is a low amplitude sweep sine in a wide frequency band. The resonance search signal profile used for the mockup testing is given below.

Table 6-12: Resonance search profile properties.

Frequency [Hz]	Amplitude
20	0.5g
2000	0.5g

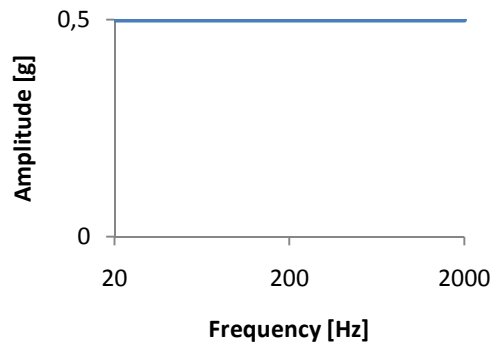


Figure 6-68: Resonance search reference input profile plot.

The low amplitude level of such an excitation allows the wide frequency range testing of the mockup, even passing through its resonances. However due to the high non-linearity of the dampers, the results of this test is not significant for the dynamic parameter estimation. The main purpose of such an excitation is to perform it before and after each strong level test and compare the results of these two tests to state whether the system was altered by the test performed in between.

### 6.1.2.2 Sweep sine

The environmental conditions of MIMA foresee a low frequency sine environment with high acceleration amplitudes. Therefore an appropriate reference excitation for the mockup testing must be defined in order to test and characterize the system concerning such an environment. The reference input used to simulate the sine environment is given below.

Table 6-13: Sweep sine excitation profile.

Frequency [Hz]	Amplitude [g]
5	1
20	20
100	20

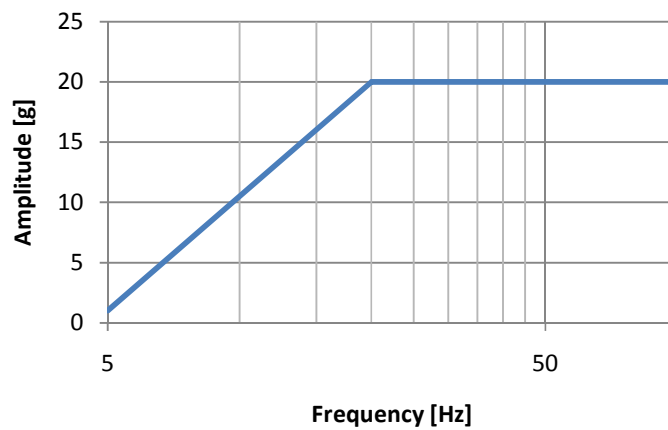


Figure 6-69: Sweep sine reference input profile plot.

Recalling the environmental conditions of the MIMA, the sweep amplitude used here is different than the one reported. Here the amplitude is lower since the aim of the study is to characterize and have an understanding of the damper system response rather than to test the endurance of the system. With this approach, failure risks due to repeated testing are reduced significantly.

### **6.1.2.3 Random**

The random vibrations of the MIMA environmental conditions are simulated for the mockup shaker testing as follows

Table 6-14: Random reference excitation

Frequency [Hz]	PSD [ $g^2/Hz$ ]	
	Z axis	X,Y axes
20	0,0174	0,007
100	0,43	0,172
400	0,43	0,172
2000	0,0174	0,007

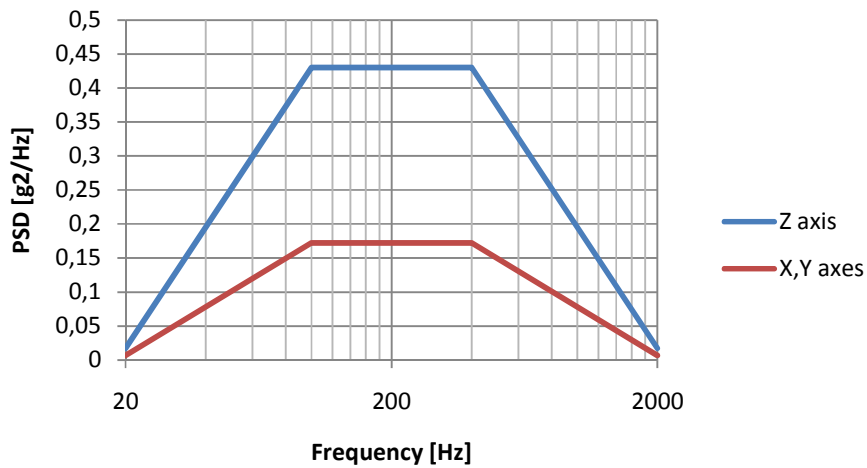


Figure 6-70: Random reference input profile plot.

For the random test, the time of excitation can be more freely selected. A too short excitation time may result in poor data because the number of averages does not allow to well estimate the parameters means while prolonging the excitation increases the risk of damaging. For the purposes of characterization of the dampers supporting the mockup, an excitation time of 45 seconds has been chosen as a compromise.

## **6.2 Mockup testing and results**

This procedure aims to test with the shaker the behavior of the three tuned dampers supporting the dummy mockup. The responses to the previously defined excitations in all three axes will be measured using systematically placed accelerometers. These measurement channels then will be used for the evaluation of various performance criteria.

All the testing directions utilize the following excitation procedure:

1. Resonance search (0.5g)
2. Sweep sine
3. Resonance search (0.5g)
4. Random
5. Resonance search (0.5g)

So the basic idea is to perform the strong tests followed and preceded by the resonance search tests. The resonance search provides some useful insight about the behavior of the system and also it is used to prove that the system at the start of the testing procedure has not been dramatically altered at the end.

### **6.2.1 Z axis testing**

The test setup shown in Figure 6-65 is excited using the given excitation profiles and the following results are obtained.

### 6.2.1.1 Z axis sweep sine

The time histories of the acquired accelerations are given below.



Figure 6-71: Z axis sweep sine test time history.

A better visualization can be achieved using FRFs between the reference acceleration and each response channel

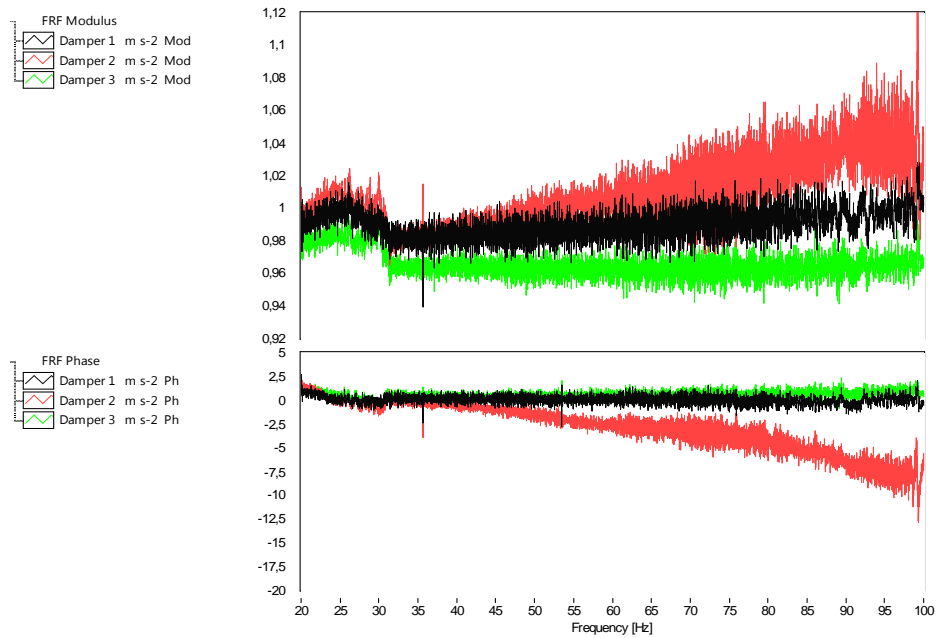


Figure 6-72: Z axis FRFs between the reference acceleration and the accelerations just at the tip of each damper.

For this testing axis, the remaining out-of-plane vibrations (channels *X down left*, *X down right* and *Y*) are very small and are not demonstrated here (see Appendix B for these plots).

### 6.2.1.2 Z axis random

A random excitation 45 seconds of random vibration with the previously defined profile is given to the system for a time of 45 s. The acquired time history of data is given below in Figure 6-73.

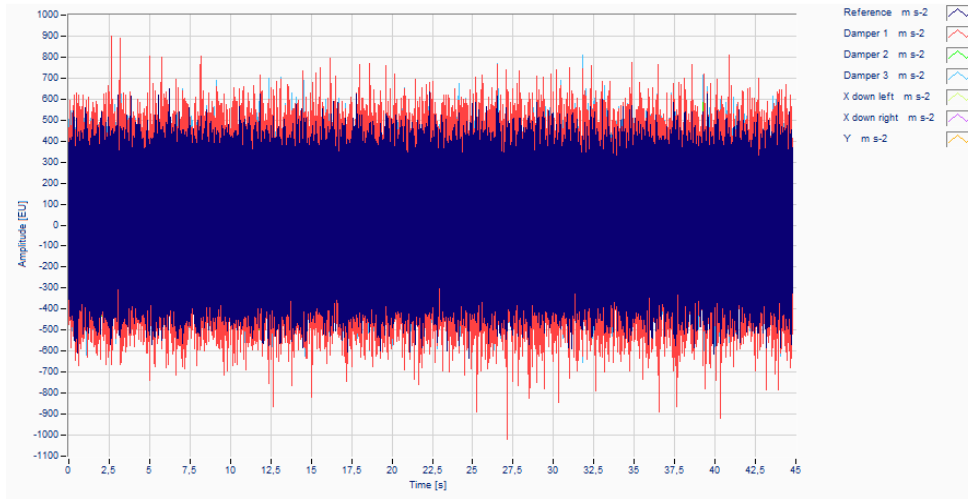


Figure 6-73: Z axis random test time history.

As far as the random environment is concerned, having a good transfer function is critical. Therefore the FRFs are also calculated.

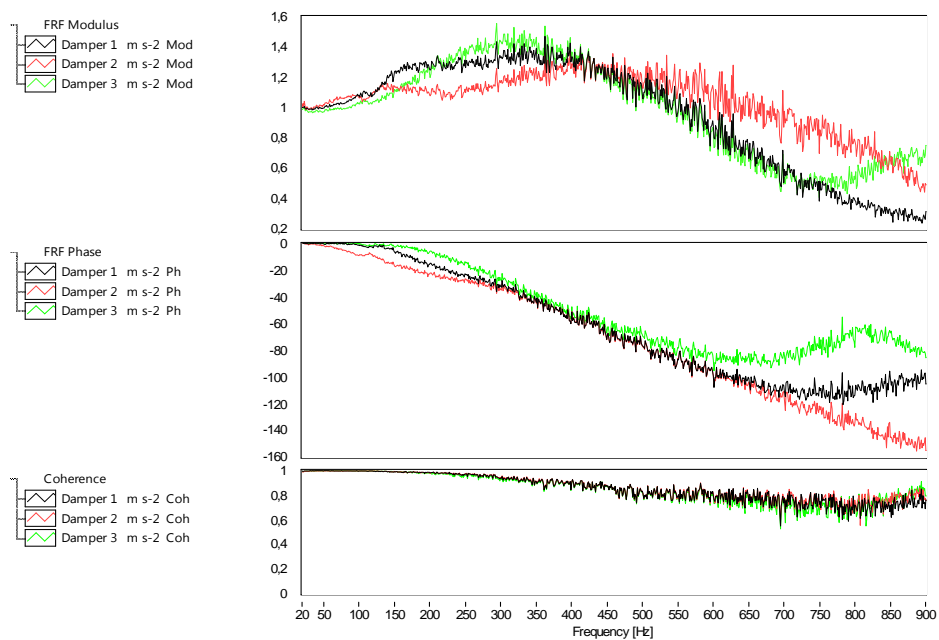


Figure 6-74: Z axis random FRF plot.

## 6.2.2 X axis testing

The dampers for this testing direction are excited transversally using the setup shown in Figure 6-66; with the given excitation profiles. In this test, the *X* accelerometer measures the response in the same direction as the excitation while the damper accelerometers measure the horizontal acceleration at the tip of each damper.

### 6.2.2.1 *X* axis sweep sine

The 20g sweep sine excitation is given to the system within the defined frequency band and the resulting time history data is given in Figure 6-75.

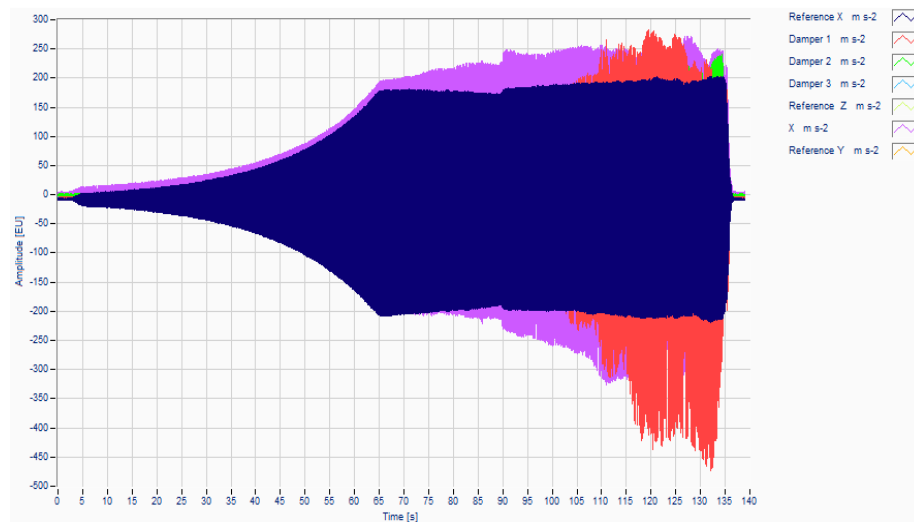


Figure 6-75: X axis sweep sine test time history.

This data can also be evaluated in terms of FRFs between the reference input and each response channel

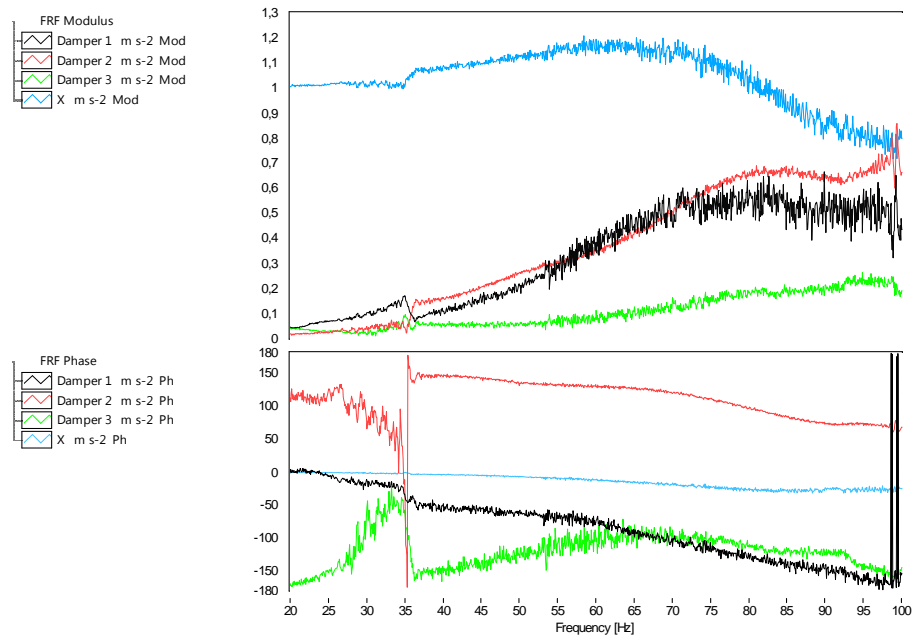


Figure 6-76: X axis sweep sine FRF plot.

### 6.2.2.2 X axis random

The time history data for a 45 seconds random vibration test for the X axis is given below in Figure 6-77.

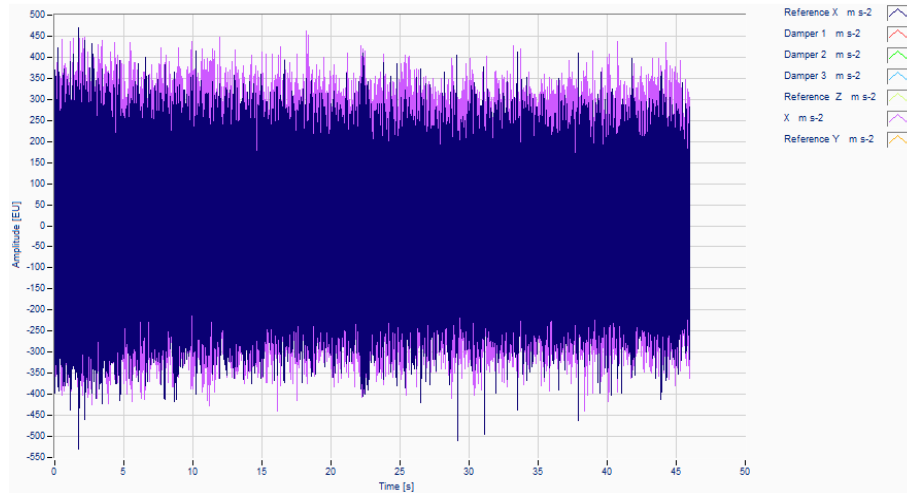


Figure 6-77: X axis random test time history.

For the evaluation of the transfer function, the FRF plot is also given

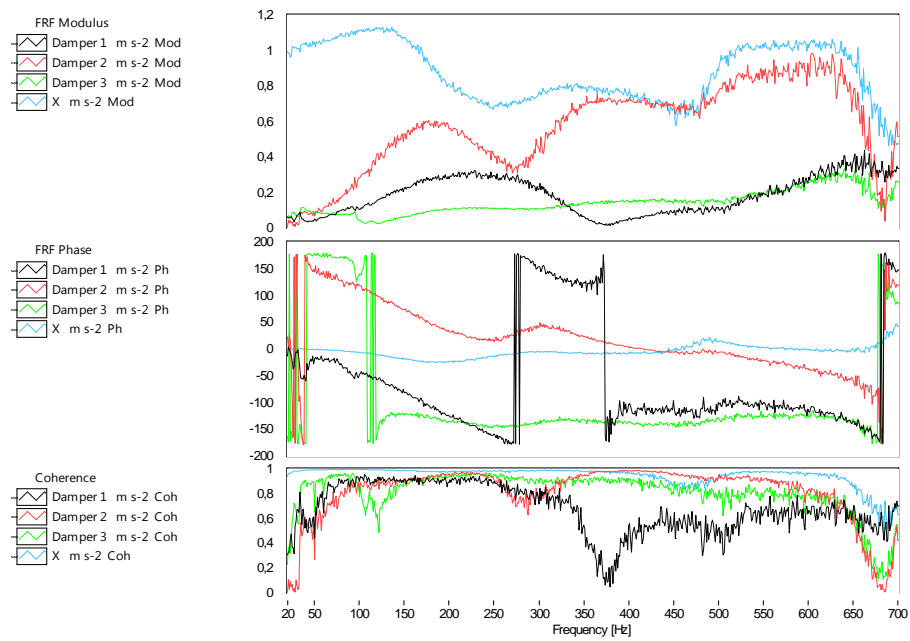


Figure 6-78: X axis random FRF plot.

### 6.2.3 Y axis testing

Recalling the setup of Figure 6-67, the excitations along the Y axis are acting transversally on the dampers, similar to the previous X axis tests. Therefore a number of acceleration channels measuring the response both in the direction of excitation (Y) and in the axial direction of the dampers (*Damper 1*, *Damper 2* and *Damper 3*) are necessary.

#### 6.2.3.1 Y axis sweep sine

The acquired time history data for the 20g sweep sine excitation in the Y axis is shown below.

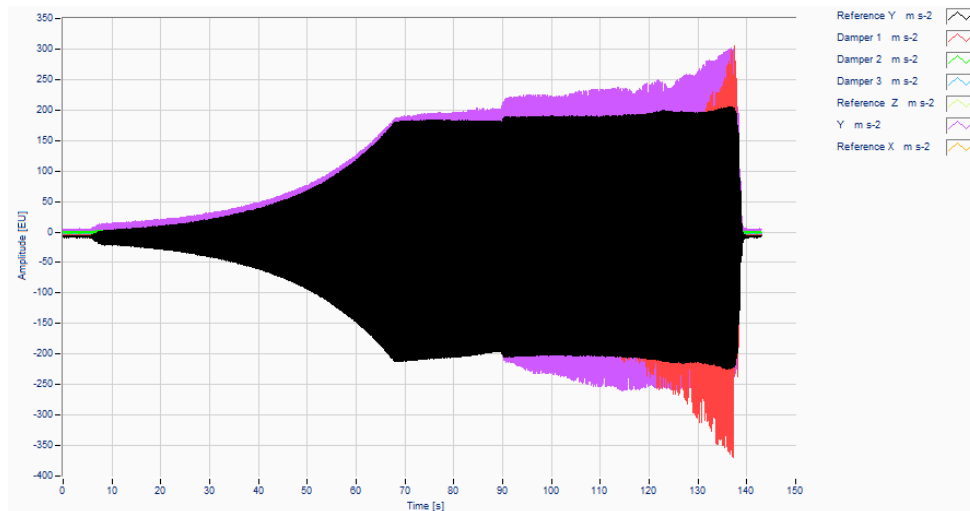


Figure 6-79: Y axis sweep sine test time history.

For a more detailed visualization, the acquired data is given in terms of FRFs in Figure 6-80.

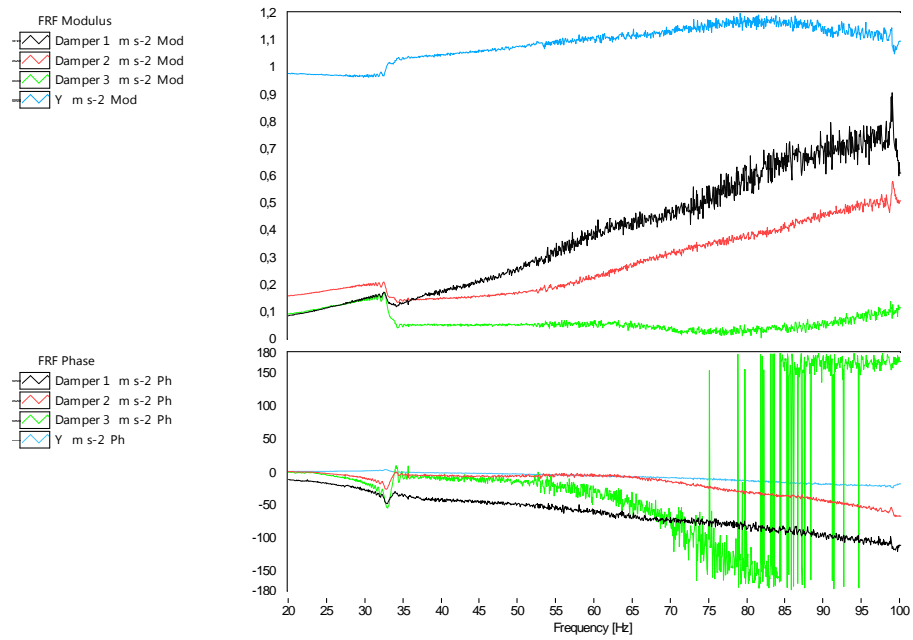


Figure 6-80: Y axis sweep sine FRF plot.

### 6.2.3.2 Y axis random

The time history data for a 45 seconds random vibration test for the Y axis is given below.

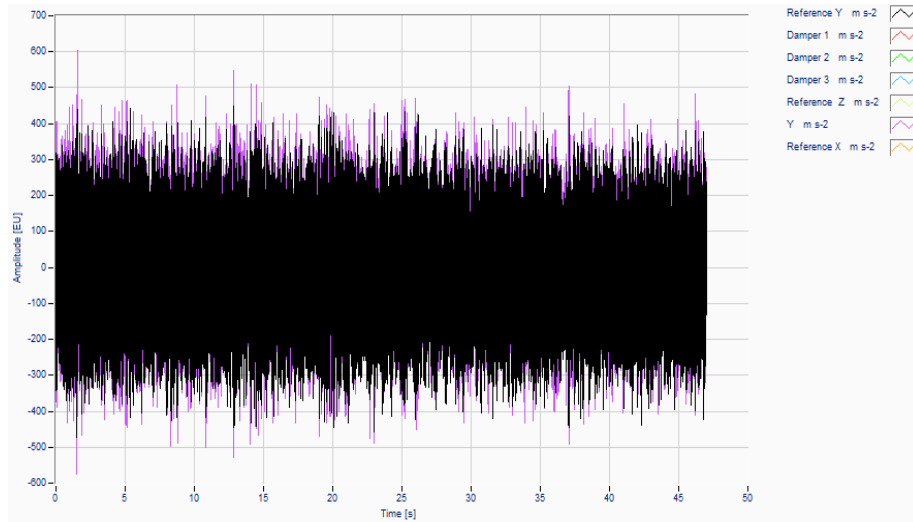


Figure 6-81: Y axis random test time history.

As done previously, the FRF between the stimulus and the response is calculated in order to assess the transfer function of the system.

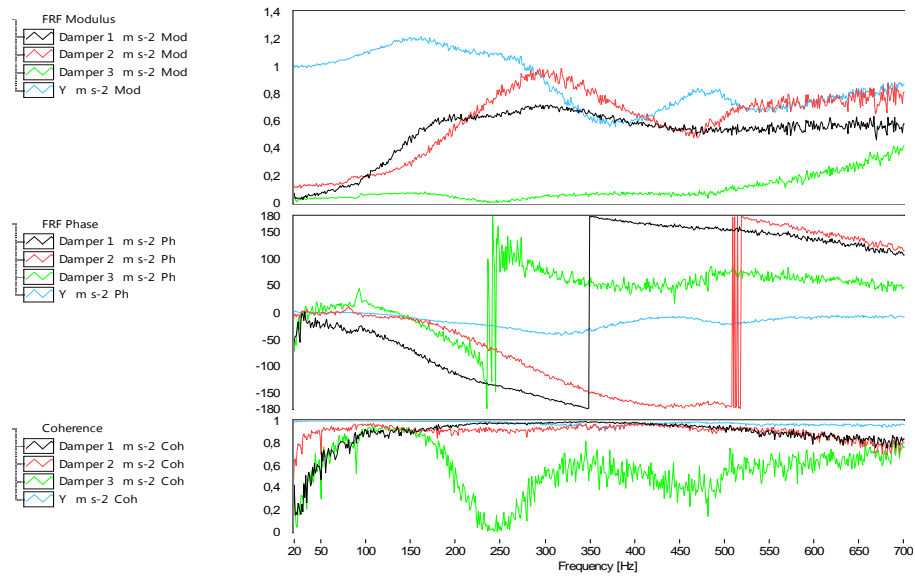


Figure 6-82: Y axis random FRF plot.

## 6.3 Evaluation of the damping system characteristics from the test results

With the results of the mockup testing acquired, an evaluation of the damping system can be performed in each testing direction. This evaluation will be performed in terms of the measured modal parameters of the system, i.e. natural frequencies, damping and mode shapes and the maximum amplifications present both for the sine and the random environment.

### 6.3.1 Performance in Z axis

Recalling the sweep sine response FRF of the system given in Figure 6-72, the first observation that can be made is the fact that there are no large amplifications in the response (maximum amplification equal to 1.05 i.e. 5%). This is a positive result as far as the sine environment is concerned. In fact, the dampers excited in this direction seem to be acting quite stiff. To support this point, the phase diagrams of the three accelerometers can be examined. The phase diagram of the signals from the three accelerometers at the top of the dampers shows almost no change. This suggests that the resonance is actually quite far away from this region.

In the random environment, the system is expected to have a good transfer function with a certain cutoff frequency, above which there are no further large amplifications of the response.

Then from the calculated FRF of the random test, the cutoff frequency can be derived as

$$f_c = 300 \text{ Hz}$$

with an amplification of

$$|H(\omega_c)| = 1.4$$

This given maximum amplification of the random transfer function is a positive result since it is not so high.

### 6.3.2 Performance in X axis

The time history and the Frequency Response plots (Figure 6-75 & Figure 6-76) for the sweep sine testing in the X axis do not exhibit high amplifications of the response (maximum amplification 1.2) and there are no significant resonances in this region of interest. These are favorable results regarding the sine environment.

In order to evaluate the transfer function regarding the X axis random behavior, the FRF between the stimulus and the response in the same direction as the excitation is given below in Figure 6-83.

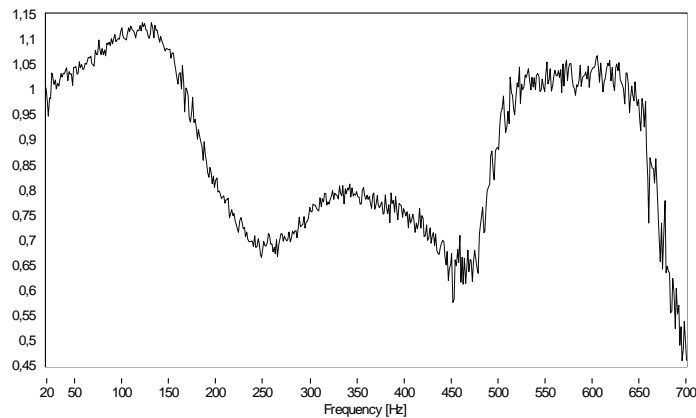


Figure 6-83: FRF Magnitude plot between the reference and the response in the same direction as the excitation.

From this plot of the transfer function, the following cutoff frequency and amplification can be defined as

$$f_c = 130 \text{ Hz}$$
$$|H(\omega_c)| = 1.15$$

The random transfer function of the system in the X axis is not as good as the transfer function in the Z direction. Even though the presence of a cutoff frequency is obvious, the amplifications beyond this value are not reduced significantly. This is an unfavorable result in terms of the damping performance. However, overall the amplifications in the FRF are small, which should compensate this unfavorable condition.

### 6.3.3 Performance in Y axis

Similar to the X axis test results, investigating the FRF plot given in Figure 6-80, it can be observed that the system does not have large amplifications (maximum amplification is 1.2) and there is no significant presence of a resonance within the sine frequency region. These are all positive results concerning the sine environment.

Studying the transfer function shown in Figure 6-84, regarding the random test, it can be stated that a slightly better performance is observed compared to the X axis testing.

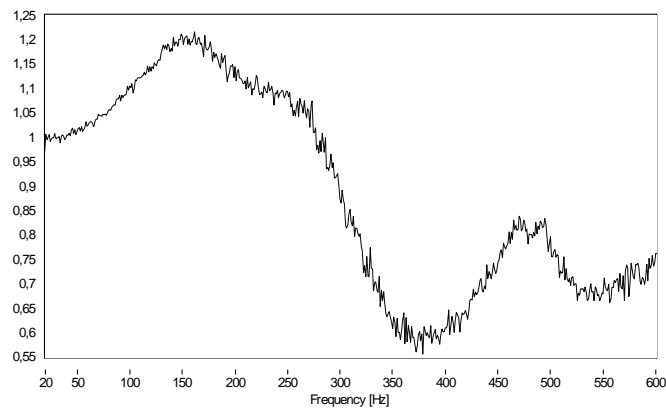


Figure 6-84: FRF Magnitude plot for the Y axis testing between the reference and the response in the same direction as the excitation.

From this plot, the cutoff values are estimated as

$$f_c = 150 \text{ Hz}$$

with,

$$|H(\omega_c)| = 1.2$$

Beyond this point, the amplifications are significantly reduced.

## 6.4 Results and discussion

Considering the mechanical environment conditions of the actual MIMA instrument, appropriate test setup and procedures were applied to test and evaluate the behavior of the previously designed and manufactured mockup mounted on the tuned dampers in the ultimate configuration. Due to the directional behavior of the system, each of the three axes was tested with the sine and the random profiles defined.

The results of the mockup testing provided useful information for the performance assessment of the tuned damping system. For all the testing directions, the sweep sine test did not reveal large amplifications of the response (maximum amplification of 20% in X and Y axes) and there were no critical resonances within the frequency range of interest. A wider frequency band could be tested using the random excitation and the corresponding cutoff frequencies above which the amplifications are dampened down were found. Overall, the transfer function for the random testing was satisfactory. All these results of the mockup testing suggest that the performance tuning performed on the dampers was on the whole satisfactory.

Considering all the testing directions and excitations, a number of critical resonances of the system were found. The first one occurred during the Z axis testing at around 300 Hz with the in-phase axial deformation of the three dampers. The second one was during X axis transversal testing at 130 Hz with the dampers deforming out-of-phase causing a rotational motion of the mockup. The third and the final one

was present during Y axis testing at 150 Hz again with the out-of-phase deformation of the damper resulting in a rotational motion.

Besides assessing the performance of the tuned damper system with three dampers in their ultimate configuration, the mockup testing also has the objective of verifying the FE model and analysis performed in Chapter 5. This can be done by comparing the results of the experimental procedure to those of the FEM analyses.

Table 6-15: Experimental modes compared to those of the FEM analysis.

	<b>Experimental</b>		<b>FEM</b>	
<b>Mode</b>	<b>Frequency [Hz]</b>	<b>Mode</b>	<b>Frequency [Hz]</b>	<b>Mode</b>
1	130	out-of-phase	131	out-of-phase
2	150	out-of-phase	151	out-of-phase
3	300	in-phase	265	in-phase

The above table clearly shows that the FEM model is accurate in estimating the natural frequencies of the system, except for a slight deviation in the third mode which is 13% lower than the measured one. Besides the frequency values of the modes, examining the phase plots from the tests show that the mode shapes are also similar to those of the FEM analysis results. Therefore it can be stated that the created Finite Elements Model is correct and accurate.

Having verified the computational model simulating a test setup, one achieves a powerful tool that can be used for optimization purposes. In the following chapter, such a study will be performed on improving the system's response using the validated FEM model.

# **Chapter 7: Finite Element Methods for the response improvement of the dampers**

## **7.1 Introduction**

In Chapter 5, a Finite Element model of the damper-mockup assembly test setup was designed. Using this model, the natural frequencies and the modes of vibration could be computed and visualized. Then in Chapter 6, comparing the data from the mockup testing on the shaker to the results of the FEM analysis, the accuracy of the model was verified.

Having an accurate and tuned computational model simulating the characteristics of the real application, acts as a strong tool for the performance improvement. Parameters of the computational model can easily be modified, unlike the experimental setup, and the resulting behavior of the system can be obtained. This procedure performed systematically in a trial and error fashion allows for the optimization of the response of the system in a fast and efficient way.

The damper name designation that will be used throughout this chapter is shown in Figure 7-85 below.

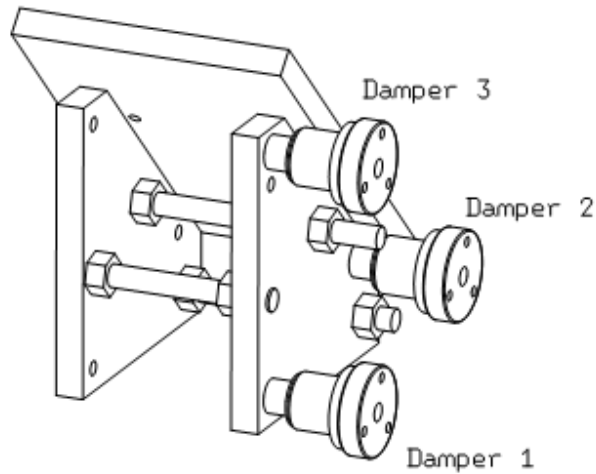


Figure 7-85: Damper name designation given.

## 7.2 Objectives of response improvement

Before actually changing any parameters of the FE model, what is meant by the possible improvements on the system response should be clarified. Recalling the natural frequencies of the damper-mockup assembly computed using the FE model

Table 7-16: Computed first three natural frequencies of the FE model

Mode	Natural frequency [Hz]
1)	131
2)	151
3)	265

From Table 7-16, it can be seen that the third mode occurs at a higher frequency than the other modes of vibration. Remembering the environmental conditions of the MIMA, it is required to have a system without any resonances below 100 Hz (for sine environment concerns)

and instead have them only slightly above this value (random environment concerns). Therefore reducing the third natural frequency can be stated as an improvement of the response. In fact having all these three critical modes at around the same frequency around 150 Hz is the ideal case and will be the main objective of the Finite Elements response improvement procedure.

There are mainly two approaches for the response improvement using the FE model depending on the parameters that will be modified to obtain an optimum. The first approach is the experimentally feasible one. Due to the limitation of the damper design, in this approach an improvement of the response will be attempted by only changing the axial stiffness of the three dampers. The second approach is more theoretical in which all the properties, be it axial or radial, of the dampers will be modified to obtain an ideal response. Of course the resulting optimum dampers cannot be achieved with this particular design, so this approach will only provide insight for the future damper designs.

### **7.3 Response improvement by modifying the axial spring properties of the dampers**

As it was investigated in the single degree-of-freedom tests of Chapter 2, the dampers' axial stiffnesses can be changed by increasing or decreasing the tightening preload on the dampers. Starting from this point, the first idea is to use different axial stiffness coefficients for each of the three dampers to obtain an improved response of the system. In this method, only the axial stiffnesses will be varied while the other radial and rotational parameters will be left untouched.

#### **7.3.1 Initial damper tuning**

In Table 7-17 is recalled the estimated spring properties of the dampers in their ultimate configuration.

Table 7-17: Stiffness values estimated and used in the FE model

Axial Stiffness, $k_1$	$1.24 \times 10^6$ N/m
Radial Stiffness, $k_2$	$1.70 \times 10^6$ N/m
Radial Stiffness, $k_3$	$1.70 \times 10^6$ N/m
Rotational Stiffness, $k_{\theta,1}$	0 Nm/rad
Rotational Stiffness, $k_{\theta,2}$	250 Nm/rad
Rotational Stiffness, $k_{\theta,3}$	250 Nm/rad

The FE model with these parameters for all the three dampers resulted in the modes given in Table 7-16. Now by only changing the axial stiffness,  $k_1$ , the third mode which is at a higher frequency with respect to the others will be decreased with the primary objective of having the first three modes of vibration occurring around 150 Hz.

### 7.3.2 Effects of individual dampers on the overall system response

In order to systematically analyze the outcome of modifying the dampers' stiffness parameters, initially the effect of having only one damper different with respect to the initial configuration is studied. Since the purpose is to decrease the occurring frequency of the third mode, which is almost a pure translation of the mockup due to the in-phase axial deformations of the dampers, the  $k_1$  value for each damper is decreased one at a time with the results summarized below in Table 7-18.

Table 7-18: Results of the various FE analysis runs with different damper properties.

Iteration	$k_1$ [N/m]			Natural Frequency [Hz]		
	<i>Damper 1</i>	<i>Damper 2</i>	<i>Damper 3</i>	<i>Mode 1</i>	<i>Mode 2</i>	<i>Mode 3</i>
Initially	1,2E+06	1,2E+06	1,2E+06	130	150	264
1	5,0E+05	1,2E+06	1,2E+06	107	149	237
2	1,2E+06	5,0E+05	1,2E+06	103	143	243
3	1,2E+06	1,2E+06	5,0E+05	112	133	241

There are several conclusions that can be drawn from the above results. The first observation is the fact that when the stiffness of any single damper is decreased, all the resulting modes are reduced in terms of their occurring frequencies. This poses some problems for the reducing of a natural frequency with respect to the others.

Another observation would be the individual effects of the dampers on the resulting modes. From Table 7-3, it can be seen that Mode 1 is most dramatically affected by the change in Damper 2, Mode 2 by Damper 3. This is a useful conclusion since it provides some instructions for the modification of each natural frequency.

It is seen however from the above results that the response improvement objective cannot be reached by modifying any single damper only. A combination of these modifications on the dampers' stiffness coefficients must be attempted for the optimum outcome of the response.

### 7.3.3 Combination of different axial stiffnesses to achieve an optimum response (Opt 1)

A systematic approach to modify the stiffnesses of individual dampers must be formulated in order to find the optimum combination of the values. The previous study showed the following results about the mode characteristics

- Mode 1 most affected by Damper 2
- Mode 2 most affected by Damper 3

However, even though this is the case, all the modes are drastically affected by the changes in the axial stiffness of an individual damper since all the vibration modes are mostly axial deformations of the dampers.

A systematic trial-and-error analysis is performed on the model with the results summarized below in Table 7-19.

Table 7-19: Systematic study of the effect of damper stiffnesses and the results

Iteration	$k_1$ [N/m]			Natural Frequency [Hz]		
	<i>Damper 1</i>	<i>Damper 2</i>	<i>Damper 3</i>	<i>Mode 1</i>	<i>Mode 2</i>	<i>Mode 3</i>
Initially	1,2E+06	1,2E+06	1,2E+06	<b>130</b>	<b>150</b>	<b>264</b>
1	7,0E+05	7,0E+05	7,0E+05	108	123	205
2	6,0E+05	6,0E+05	6,0E+05	103	116	190
3	5,0E+05	5,0E+05	5,0E+05	97	109	174
4	5,0E+05	8,0E+05	5,0E+05	101	117	188
5	5,0E+05	8,0E+05	7,0E+05	<b>103</b>	<b>125</b>	<b>198</b>

To start with, in order to reduce the natural frequency of the third mode of vibration as much as possible, all the  $k_1$  values for the three dampers are decreased equally until at some point the first mode slightly falls below 100 Hz. This is an undesired condition due to the sine environment conditions discussed before. Therefore this is a minimum limit for the stiffnesses of the dampers. Then, to increase the first natural frequency, Damper 2 is made stiffer, since this is the damper most critical for the first mode. Furthermore the second natural frequency is also increased by slightly increasing the stiffness of Damper 3. Doing this, the third natural frequency is also increased so this is said to be a maximum limit for the stiffness of the dampers.

The damper tunings obtained at the end of Iteration 5 seem to give the result that are the closest possible to the ones desired. All the natural frequencies corresponding to the first three modes of vibration were reduced, the third one more while the first two less, suggesting some convergence. Still, the results of the suggested tuning of dampers are far

from the objectives since the first natural frequency became too low in the process of optimization and the third mode is still too large.

Considering all these results, at the end it can be stated that the response improvement objectives cannot be met only by changing the axial stiffness of the dampers. The remaining radial and rotational parameters of the dampers should also be modified, even though it requires a principal design change.

## **7.4 Response optimization of the system with theoretical dampers**

In this section of the study, it is attempted to meet the response improvement objectives using any possible modifications on the damper stiffness parameters, not only the axial one but also the radial one.

### **7.4.1 Effect of the radial stiffness coefficient**

Recalling the mode shapes of the original system utilizing the dampers in their ultimate configuration, the modes of vibration obtained were mostly due to the axial deformation of the dampers, either in-phase with each other or out-of-phase. From the previous analyses, it was observed that these modes were strictly dependent on the axial stiffnesses of the damper and it was quite hard to achieve a perfect optimization modifying only these values. Therefore in this section the effect of changing the radial stiffnesses of the dampers are investigated.

Below in Table 7-20 are given some analyses performed with different radial stiffnesses at a constant axial stiffness and the corresponding results.

Table 7-20: Various analyses changing the radial stiffness and the results

$k_1 = 7e+05 \text{ N/m}$						
	$k_{2,3} \text{ [N/m]}$			<b>Natural Frequency [Hz]</b>		
Iteration	<i>Damper 1</i>	<i>Damper 2</i>	<i>Damper 3</i>	<i>Mode 1</i>	<i>Mode 2</i>	<i>Mode 3</i>
1	1.0E+06	1.0E+06	1.0E+06	105	119	203
2	5.0E+05	5.0E+05	5.0E+05	99	109	200
3	1.5E+06	1.5E+06	1.5E+06	109	123	204

From the results given above, it can be observed that changing the radial stiffness mainly affects the natural frequencies that correspond to the first two modes of vibration while the third natural frequency is not so dramatically affected. The maximum deviations of the first, second and the third natural frequencies between the 2<sup>nd</sup> and the 3<sup>rd</sup> iterations are 9%, 11% and 2% respectively.

#### 7.4.2 Effect of axial stiffness coefficient

Recalling the conclusions from the previous sections, it can be stated that the radial stiffness mainly affects the first two modes while the axial stiffness affects all three critical modes of the system. Therefore a reasonable approach would be to increase the radial stiffness to increase the first two natural frequencies and then decrease the axial stiffness to reduce all the modes, resulting in some convergence. Such a procedure is described with the obtained result in the table below.

Table 7-21: Various analyses changing the axial stiffness for a given radial stiffness

$k_{2,3} = 6e+06 \text{ N/m}$						
	$k_1 \text{ [N/m]}$			<b>Natural Frequency [Hz]</b>		
Iteration	<i>Damper 1</i>	<i>Damper 2</i>	<i>Damper 3</i>	<i>Mode 1</i>	<i>Mode 2</i>	<i>Mode 3</i>
1	1.2E+06	1.2E+06	1.2E+06	136	159	268
2	9.0E+05	9.0E+05	9.0E+05	122	141	233
3	7.0E+05	7.0E+05	7.0E+05	111	127	206
<b>4</b>	<b>5.0E+05</b>	<b>5.0E+05</b>	<b>5.0E+05</b>	<b>101</b>	<b>112</b>	<b>175</b>

As seen from these results, choosing a high enough radial stiffness and gradually decreasing the axial one, an improvement could be reached in terms of the natural frequencies of the system.

### 7.4.3 Resulting modes of vibration of the optimal system (Opt 2)

At the end of the analysis, the following vibration modes shown in Figure 7-86 are obtained from the FE model in CATIA.

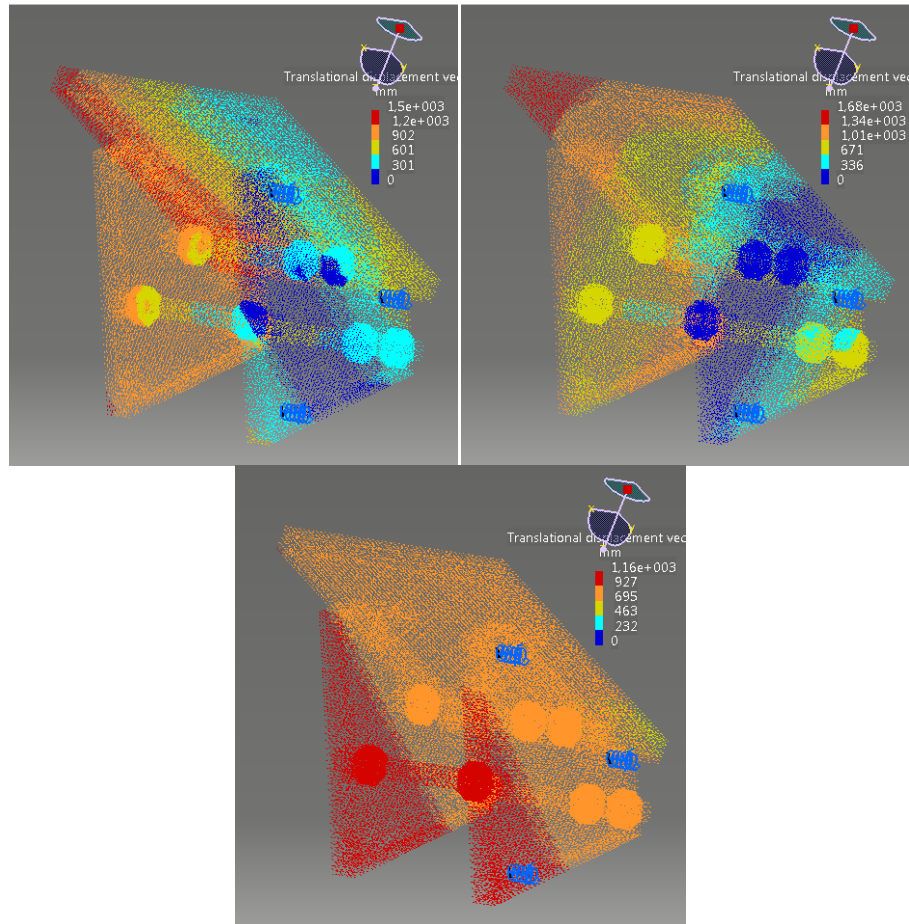


Figure 7-86: Vibration mode shapes clockwise at (a) 101 Hz (b) 112 Hz (c) 175 Hz

## 7.5 Performance comparison of the damper tunings using FE methods

In this section, more detailed FE analyses will be performed to compare the performances of the damper tunings suggested previously.

### 7.5.1 Method of performance assessment

The objectives of the response improvement using FRM were defined previously and the following analyses were conducted to achieve these objectives. However, in order to give a more quantitative assessment on whether the system response is improved or not, further simulations have to be performed.

This method of performance assessment makes use of an advanced FE model of the MIMA and the tuned dampers to simulate the system's random environment behavior. The details of the FE analysis of the MIMA will not be included in the scope of this work, however what is critical is that the tuned damper parameters can be input to this advanced model to obtain the resulting FRFs at any critical point on the MIMA (for this application, the optical elements).

Once the FRF is obtained from the FE analysis of the MIMA in terms PSD (FRF squared), it is multiplied by a weighting profile to emphasize the more critical portions of the frequency band. This profile is given below in Figure

Table 7-22: Weighing profile to be multiplied by the FRF squared profile

Frequency [Hz]	Factor
20	1.7
500	20
2000	20

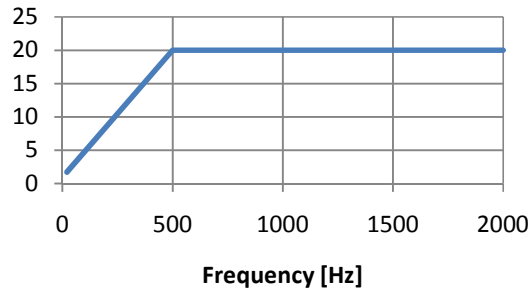


Figure 7-87: Weighing profile plotted.

The result of the multiplication of the  $FRF^2$  profile with the weighing function returns a Weighed  $FRF^2$  profile, whose RMS value can be used to compare the performance of each tuning configuration. In principle the function should be multiplied with the PSD one to get the accelerations RMS. However, the PSD at this stage is still not well defined, so it has been preferred not to link the result to this uncertain input; the result will still be valid as long as the profile is quite flat in the frequency range of interest.

## 7.5.2 Assessment of the test configuration

The above described procedure is applied using the dampers in their testing configurations for loading conditions in all the three axes.

### 7.5.2.1 Test X loading

The computed FRF squared profile of the response to a random loading in the X direction is given by

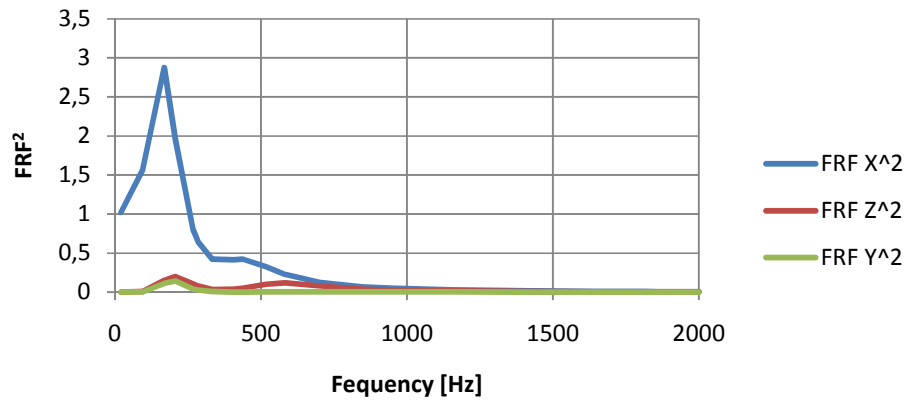


Figure 7-88: Evaluated FRF<sup>2</sup> profile for the three axes in X loading

Multiplying the above profile with the weighing function shown in Figure 7-87, one gets

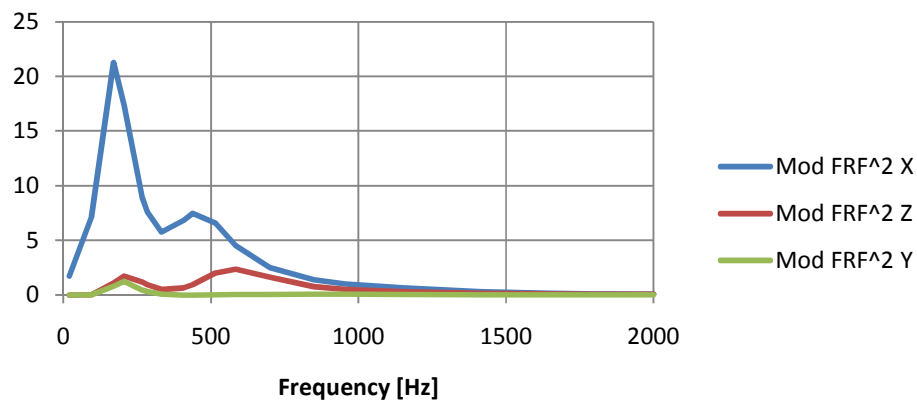


Figure 7-89: Weighed FRF<sup>2</sup> profiles for X loading

Then the RMS value for each of these discrete profiles can be calculated using the formula

$$RMS = \sqrt{\frac{\sum_{i=1}^n x_i^2}{n}}$$

Performing this simple calculation, the RMS values are found and are summarized in the Table 7-23 below.

Table 7-23: RMS values for the weighed FRF<sup>2</sup> profiles for the X loading condition

<b>RMS X</b>	7.234
<b>RMS Y</b>	0.341
<b>RMS Z</b>	0.988

### 7.5.2.2 Test Y loading

The FRF squared profile resulting from the loading in the Y direction is shown below.

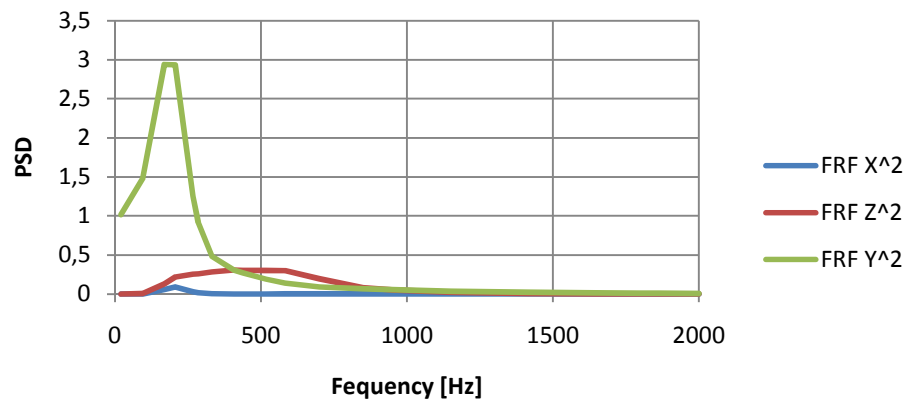


Figure 7-90: FRF<sup>2</sup> profile for the three axes in Y loading

Once this profile is weighed by the weighing function it becomes

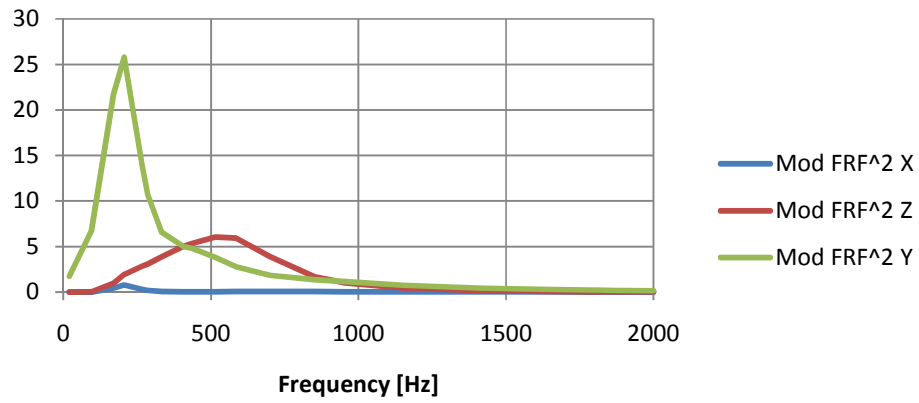


Figure 7-91: Weighed FRF<sup>2</sup> profiles for Y loading

The RMS values calculated for the weighed FRF<sup>2</sup> profile are given in the table below.

Table 7-24: RMS values for the weighed FRF<sup>2</sup> profiles for the Y loading condition

<b>RMS X</b>	0.213
<b>RMS Y</b>	8.570
<b>RMS Z</b>	2.880

### 7.5.2.3 Test Z loading

The FRF<sup>2</sup> response to a random loading in Z direction is computed as

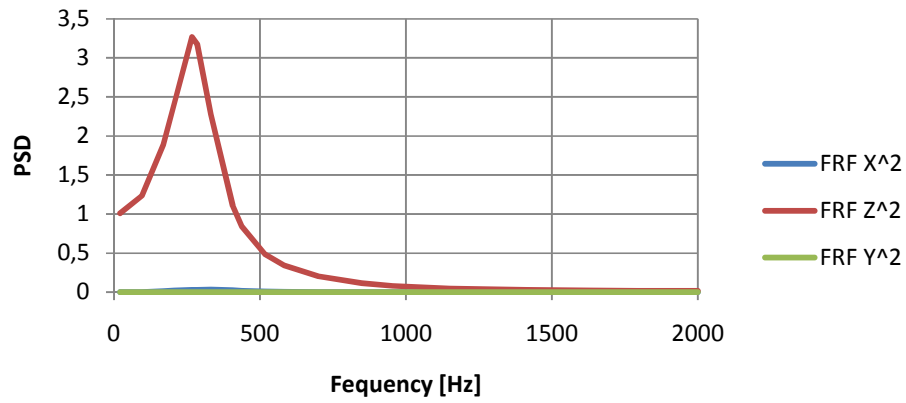


Figure 7-92: Evaluated FRF<sup>2</sup> profile for the three axes in Z loading

Once multiplied by the weighing function given in Figure 7-87, the weighed FRF<sup>2</sup> profile becomes

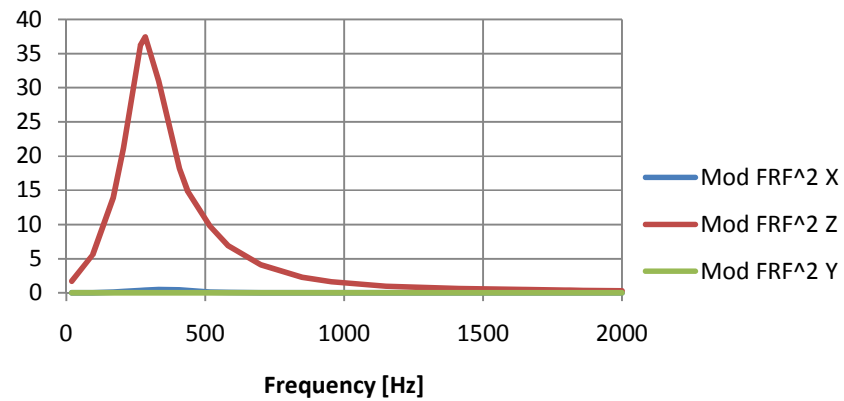


Figure 7-93: Weighed FRF<sup>2</sup> profiles for Z loading

Similarly, the RMS value is calculated for the three measurement axes as

Table 7-25: RMS values for the weighed FRF<sup>2</sup> profiles for the Z loading condition

<b>RMS X</b>	0.193
<b>RMS Y</b>	0.004
<b>RMS Z</b>	15.178

### 7.5.3 Assessment of the optimization performed through changing axial stiffnesses (Opt 1)

The performance assessment procedure is applied using the suggested dampers modified in terms of their axial stiffnesses for loading conditions in all the three axes.

#### 7.5.3.1 Opt 1 X loading

The FRF squared profile resulting from a loading in the X direction is shown below in Figure 7-94

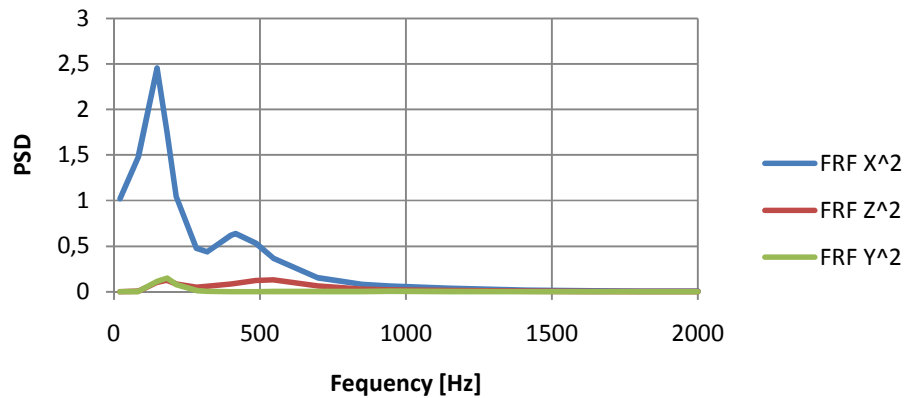


Figure 7-94: FRF<sup>2</sup> profile measured for the three axes in X loading

When multiplied by the weighing function, this plot becomes

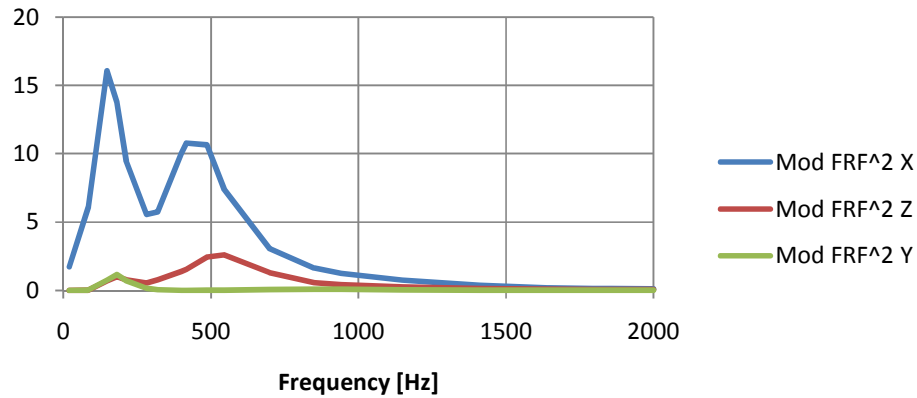


Figure 7-95: Weighed FRF<sup>2</sup> profile for X loading

Then the RMS values corresponding to each measured axis can be calculated. These results are given in the table below.

Table 7-26: RMS values for the weighed FRF<sup>2</sup> profiles for the X loading condition

<b>RMS X</b>	6.872
<b>RMS Y</b>	0.336
<b>RMS Z</b>	1.006

### 7.5.3.1 Opt 1 Y loading

The computed FRF squared profile resulting from a loading in the Y direction is given by

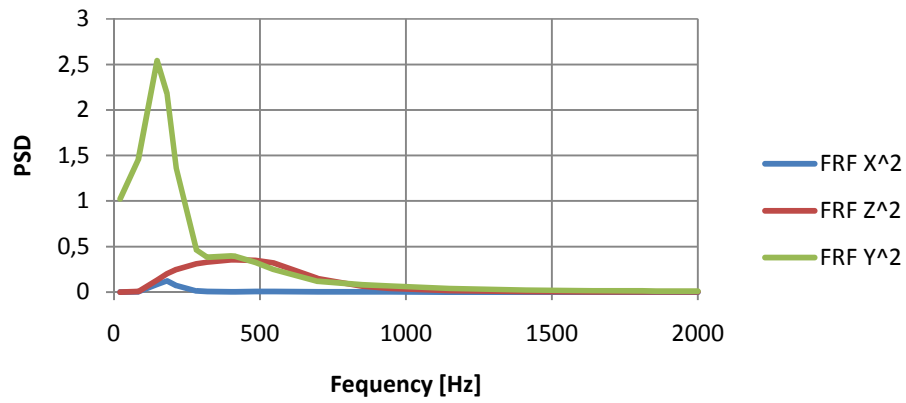


Figure 7-96: FRF<sup>2</sup> profile measured for the three axes in Y loading

When weighed using the defined function, this profile becomes

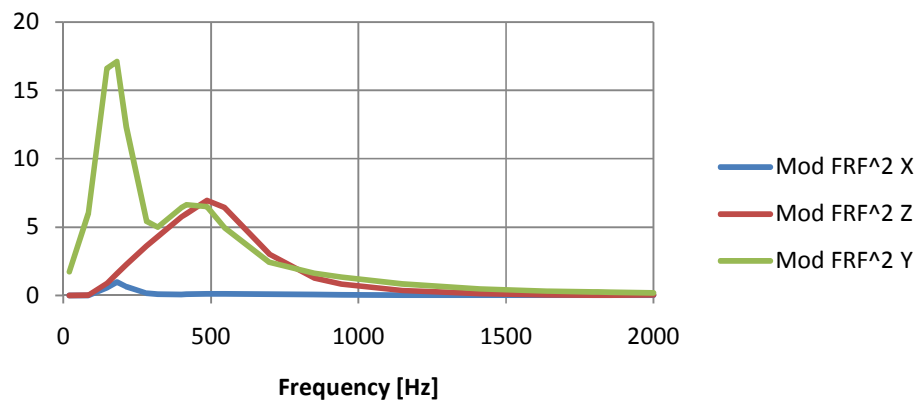


Figure 7-97: Weighed FRF<sup>2</sup> profile for Y loading

Then the corresponding RMS values to each measured axis can also be calculated as

Table 7-27: RMS values for the weighed FRF<sup>2</sup> profiles for the Y loading condition

<b>RMS X</b>	0.283
<b>RMS Y</b>	6.668
<b>RMS Z</b>	3.086

### 7.5.3.3 Opt 1 Z loading

When the system is loaded in the Z direction, the resulting FRF squared profile on the pint defined is computed and it is plotted below in Figure 7-98

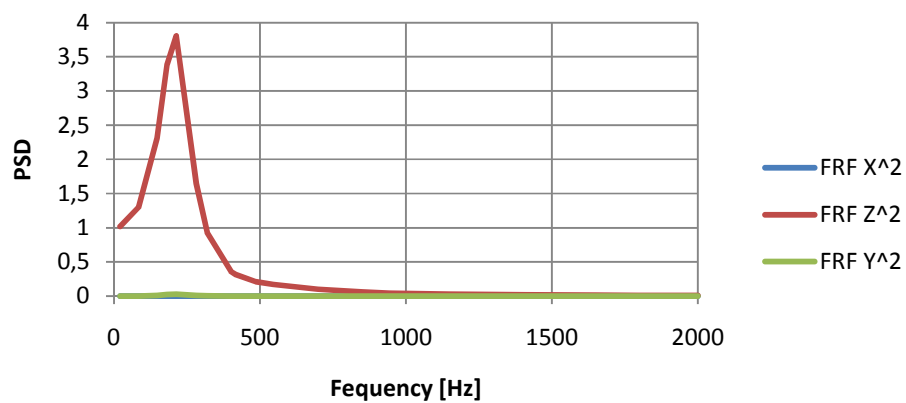


Figure 7-98: FRF<sup>2</sup> profile measured for the three axes in Z loading

Similarly, the weighed FRF<sup>2</sup> profile can be plotted as

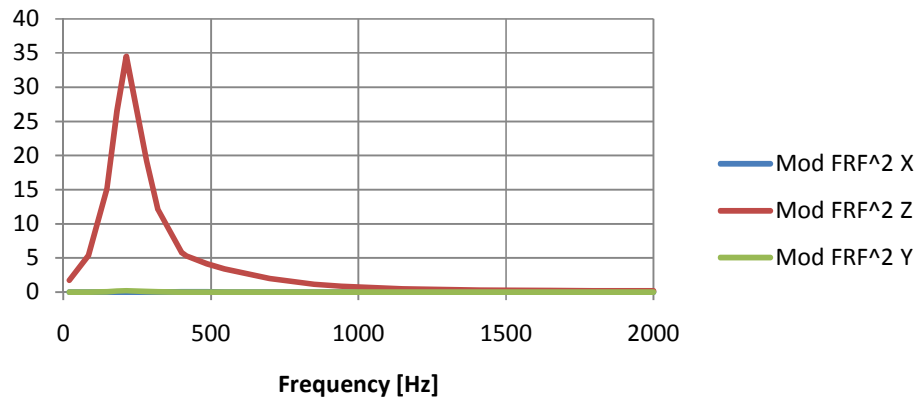


Figure 7-99: Weighed FRF<sup>2</sup> profile for Z loading

And the corresponding RMS values for the three measurement axes are given by

Table 7-28: RMS values for the weighed FRF<sup>2</sup> profiles for the Z loading condition

<b>RMS X</b>	0.012
<b>RMS Y</b>	0.064
<b>RMS Z</b>	11.221

#### 7.5.4 Assessment of the optimization performed through changing both the axial and the radial stiffnesses (Opt 2)

In section 7.4, an optimization of the response was suggested through changing both the radial and the axial stiffnesses of the dampers in the described manner. Here, these stiffness parameters are input to the FE simulation for the assessment of the tuning performance.

### 7.5.4.1 Opt 2 X loading

The FRF squared profile computed at the designated location on the MIMA for the X loading condition is given by

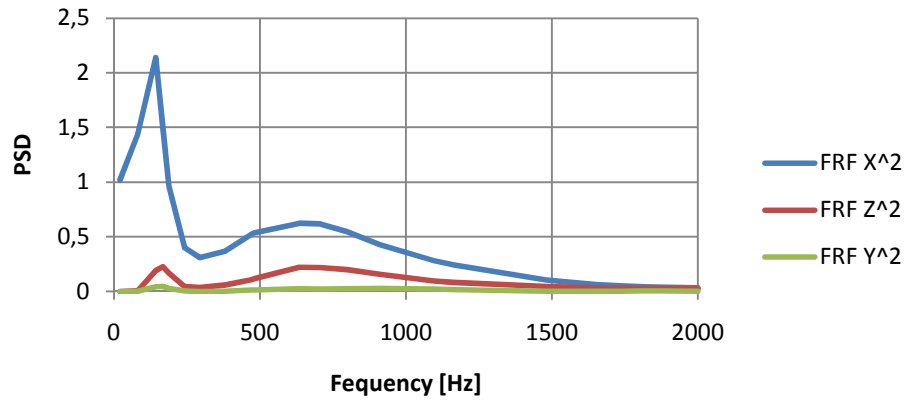


Figure 7-100: FRF<sup>2</sup> profile measured for the three axes in X loading

Once this plot is multiplied by the weighing function, it becomes

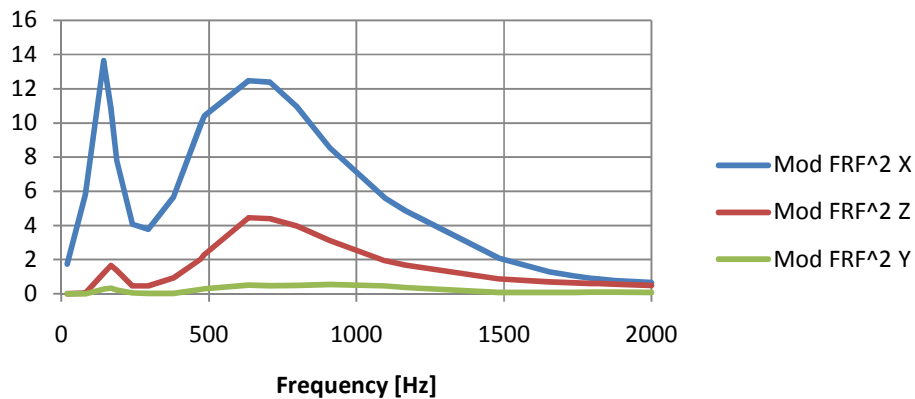


Figure 7-101: Weighed FRF<sup>2</sup> profile for X loading

The RMS values of each axis for this profile is calculated as

Table 7-29: RMS values for the weighed FRF<sup>2</sup> profiles for the X loading condition

<b>RMS X</b>	7.334
<b>RMS Y</b>	0.279
<b>RMS Z</b>	1.985

#### 7.5.4.2 Opt 2 Y loading

The FRF squared profile computed for the Y loading condition is shown in the figure below.

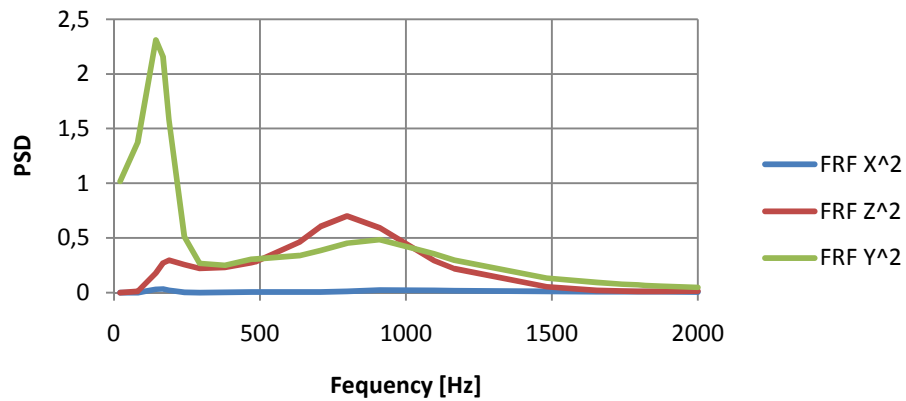


Figure 7-102: FRF<sup>2</sup> profile measured for the three axes in Y loading

The weighed form of this profile is shown in the figure below.

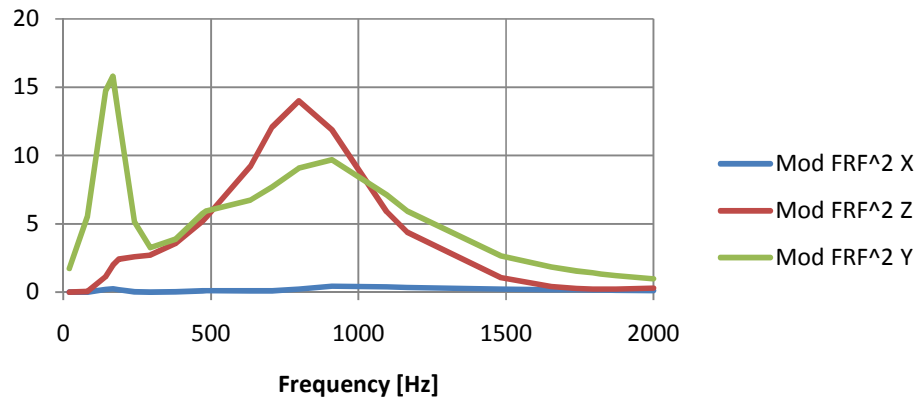


Figure 7-103: Weighed FRF<sup>2</sup> profile for Y loading

And the corresponding RMS values are

Table 7-30: RMS values for the weighed FRF<sup>2</sup> profiles for the Y loading condition

<b>RMS X</b>	0.196
<b>RMS Y</b>	7.135
<b>RMS Z</b>	5.587

#### 7.5.4.3 Opt 2 Z loading

The FRF squared profile from the simulation with a loading in the Z direction is computed as

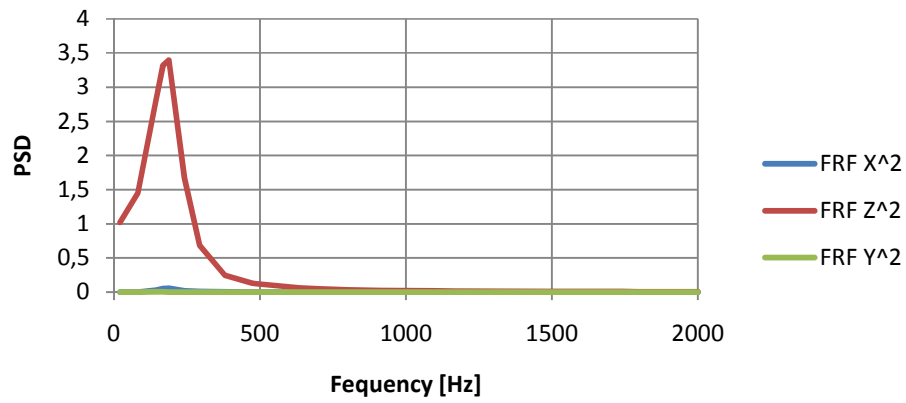


Figure 7-104: FRF<sup>2</sup> profile measured for the three axes in Z loading

The above profile is multiplied by the weighing function to obtain the weighed FRF<sup>2</sup> profile as

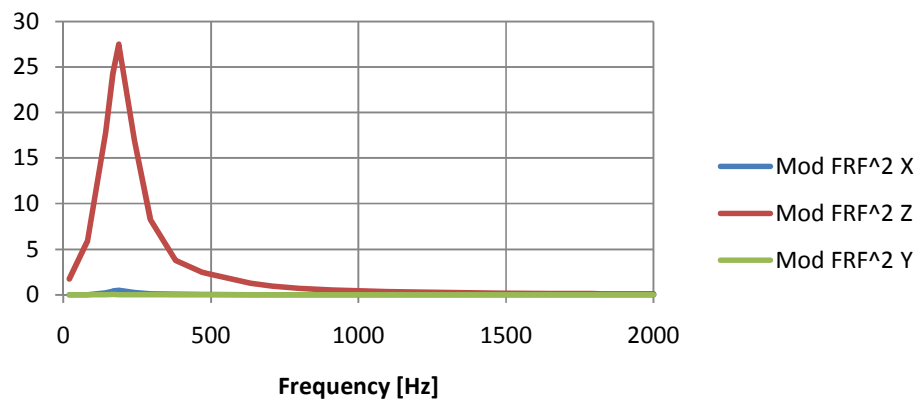


Figure 7-105: Weighed FRF<sup>2</sup> profile for Z loading

with the following calculated RMS values

Table 7-31: RMS values for the weighed FRF<sup>2</sup> profiles for the Z loading condition

<b>RMS X</b>	0.148
<b>RMS Y</b>	0.006
<b>RMS Z</b>	9.520

### 7.5.5 Performance comparison of the optimal damper tunings

Once all the calculations have been performed to assess the performance of the initial test configuration and the improvements suggested, a comparison between them is possible. The Table below summarizes all the results of the previous performance computations for the test configuration, the optimization performed by axial stiffness modifications (*Opt 1*) and the radially and axially modified dampers (*Opt 2*).

Table 7-32: Results of the performance assessment summarized

		RMS		
		Test	Opt 1	Opt 2
<b>X loading</b>	X	7.234	6.872	7.334
	Y	0.341	0.336	0.279
	Z	0.988	1.006	1.985
<b>Y loading</b>	X	0.213	0.283	0.196
	Y	8.570	6.668	7.135
	Z	2.880	3.086	5.587
<b>Z loading</b>	X	0.193	0.012	0.148
	Y	0.004	0.064	0.006
	Z	15.178	11.221	9.520

The first observation that can be made looking at these results is the fact the both the optimizations resulted favorably as far as the RMS in the Z axis is concerned (axial direction of the dampers). The critically high initial value of 15.2 experienced a fall of 26% with the *Opt 1*

configuration and 38% with the *Opt 2* configuration. This is an expected result since the natural frequency corresponding to the Z translational mode was the main objective of response improvement. Looking at this data, it can be said that this objective was fulfilled.

However, there are other critical observations regarding these final RMS results. The *Opt 1* configuration obtained by only modifying the axial stiffnesses did not cause much change in the transversal loading cases. On the other hand the radially modified *Opt 2* configuration suffers from some increase in the final RMS for the transversal excitations up to 90% in the Z axis when loaded in Y direction. This result can be attributed to some high frequency torsional modes caused by the increased radial stiffness of the dampers.

Finally it can be stated that both the optimizations suggested have their advantages when compared to the testing configuration. However, there is a certain trade-off between these two configurations. If the axial performance of the system is desired to be increased further, a compromise should be made from the transversal performance.

## **7.6 Results and discussion**

In this final part of the study, the designed and verified Finite Elements model of the mockup testing setup was used to suggest some improvements on the response of the system. This is done by getting the optimal response from the FEM analysis by varying the individual damper properties and using this information as damper tuning feedback.

The objectives of response improvement were defined considering the proximity of the first three critical modes of vibration of the system.. For this purpose, the third mode of vibration at a higher natural frequency compared to the others should be shifted to a lower frequency. This is attempted by two different approaches.

The first approach to the response improvement was to use the capabilities of the current damper design which allows changes in the axial stiffness. Therefore just by varying the individual axial stiffness coefficients of the three dampers, various runs of the FE model were made to optimize the response. However in the end it was not actually possible to meet the objectives of the response improvement since all the modes were strictly dependent on the axial spring parameters.

The second approach was to assume a theoretical design of the dampers that allows for any changes in the stiffness parameters. Through a systematic modification procedure of the radial and the axial stiffnesses, the optimum response of the system was obtained.

The two suggested damper configurations and the resulting modes of vibration are summarized in Table 7-33.

Table 7-33: Suggested optimum spring properties and the resulting modes of vibration.

	$k_{\text{axial}}$ [N/m]			$k_{\text{radial}}$ [N/m]	Natural Frequency [Hz]		
	Damper 1	Damper 2	Damper 3		Mode 1	Mode 2	Mode 3
Init	$1.2 \times 10^6$	$1.2 \times 10^6$	$1.2 \times 10^6$	$1.7 \times 10^6$	131	151	265
Opt 1	$5.0 \times 10^5$	$8.0 \times 10^5$	$7.0 \times 10^5$	$1.7 \times 10^6$	103	125	198
Opt 2	$5.0 \times 10^5$	$5.0 \times 10^5$	$5.0 \times 10^5$	$6.0 \times 10^6$	101	112	175

Furthermore, the performance study of the two suggested optimizations in the damper configuration is performed using an advanced FE model of the MIMA instrument. After various calculations, the load transmissibility on the instrument was obtained and its RMS value was used as the basis of comparison for performance. At the end of this study, both the suggested optimizations were proved to be advantageous. *Opt 2* configuration was more efficient than *Opt 1* in reducing the excitations in the axial direction while it had poorer performance in the transversal loading conditions. The choice between these two optimizations involve some compromise and is strictly application dependent.

## Chapter 8: Conclusion and final remarks

In this study, the characterization and optimization process for a vibration damping system designed for an instrument, devoted to a space mission, was realized through experimental and computational methods. In order to achieve this goal, several integrated objectives were pursued simultaneously.

The first objective of the study was to design and manufacture a test mockup to be used in place of the actual instrument for vibration testing purposes. To achieve this, software tools were used to design an inertially equivalent dummy simple enough for easy and cheap manufacturing.

The second task to be performed was the individual testing and tuning of the dampers to be used in the mission. For this purpose, a shaker based test setup was implemented in which the single damper and a representative dummy mass were assembled together as a single degree of freedom system. Using this test setup, several characteristics of the dampers were investigated and some important conclusions were reached. To start with, the non-linear characteristics of the dampers were investigated, observing different responses of the same damper to different types of input or amplitudes of the excitation. Furthermore, the effect of changing the tightening preload on the response of the dampers was studied extensively and it was concluded that a wide range of stiffness values could be achieved with a single damper design by utilizing this regulation capability. Another useful study was performed to characterize the effect of including additional ring elements in the damper assembly and the result was found to be positive due to an increased stiffness and stability of the dampers. Finally having tested and investigated all these aspects, an ultimate damper tuning could be achieved to achieve the optimum performance with respect to the given environmental conditions of the mission.

The shaker testing procedures were adopted inspired from Experimental Modal Analysis techniques which allow the description of a system through its modal properties such as the natural frequencies, damping ratio and mode shapes. Having obtained these parameters for the ultimate damper configuration through single DOF testing, various analytical calculation methods and mathematical models were utilized to estimate the numerical properties of the individual dampers.

One of the most important objectives of this study was the implementation of a Finite Elements model of the experimental setup involving the damper-mockup assembly. A FE modeling was established in CATIA software using spring elements to replace the dampers in order to analyze the natural properties of the system. The various directional stiffness coefficients of these virtual springs were estimated using the previously calculated modal parameters from the single DOF tests. Running the FE model, three significant modes of vibration were observed at frequencies above 100 Hz, a positive result regarding the environmental conditions. Besides the natural frequencies, the mode shapes of the system were also investigated, showing two rotational modes at lower frequencies caused by the out-of-phase deformation of the springs and an almost purely translational mode at higher frequency caused by the in-phase deformation of all the three springs.

With a mockup inertially equivalent to the actual MIMA instrument and three dampers tuned at their ultimate configuration, the complete system was assembled and tested on the shaker along the three axes using sweep sine and random excitations considering the environmental conditions of the real application. The response of the system was measured and the results were analyzed using various signal processing techniques. Considering the desired response of the system, the resulting performance of the dampers was found to be satisfactory. There were no significant resonances or amplifications in the sweep sine region (5-100 Hz) that is a requirement for the sine environment. Furthermore, the resulting transfer function in the random environment was satisfactory with low amplifications that were cutoff after a certain frequency. From the dummy model test results, this cutoff frequency was found to be 300 Hz for the Z axis loading and around 150 Hz for the

X and Y axis loadings. All these results suggest that the damper tuning performed initially was successful.

Besides providing invaluable information about the working behavior of the system, the mockup testing also provided feedback data to check the accuracy of the FE model implemented. The natural frequencies and the mode shapes of the mockup tests were compared to the results of the FEM analysis and the model was found to be acceptable because the errors in the predicted natural frequency was less than 12%.

The final objective of the study was to suggest some improvements on the response of the system rather than accepting the results coming out of the tests. For this purpose, the previously verified FE model has been used to find the optimal damper parameters that result in an improved response in terms of the modes of vibration. Two optimizations were suggested for the damper parameters, one including changes in the axial stiffness therefore being applicable for the current damper design, the second assuming a theoretical design which allows changes both in the axial and the radial parameters. In order to support these optimizations with a more quantitative approach, an advanced FE model of the actual MIMA was used to calculate the FRFs and the corresponding RMS values resulting from a random excitation on the most critical part of the instrument. In the end, both these optimizations were found to be advantageous, one having better performance in axial loading conditions and the second acting more favorably when loaded transversally. The choice of the optimization to be used surely requires some compromise and is strictly 'application dependent'. This could be the objective of a further study regarding the optimization of the damping system as well as the mechanical design of new damper elements having more versatile stiffness parameters.

## References

[1] Bellucci G.; Saggin B.; Fonti S.; Biondi D.; Cerulli P.; De Luca M.; Altieri F.; Mattana A.; Alberti E.; Marzo G.; Zasova L.

MIMA, a miniaturized Fourier infrared spectrometer for Mars ground exploration: part I, concept and expected performance, *Proceedings of SPIE, the International Society for Optical Engineering* 2007

[2] Marzo, G. A.; Bellucci, G.; Fonti, S.; Saggin, B.; Alberti, E.; Altieri, F.; Politi, R.; Zasova, L.; The Mima Team

MIMA: Mars Infrared MApper - The Fourier spectrometer for the ESA Pasteur/ExoMars rover mission, *36th COSPAR Scientific Assembly 2006, Beijing, China*

[3] ESA – ExoMars – The ExoMars Instruments

[http://www.esa.int/SPECIALS/ExoMars/SEMSZIAMS7F\\_0.html](http://www.esa.int/SPECIALS/ExoMars/SEMSZIAMS7F_0.html)

Last visited on: April 2010

[4] ESA ExoMars Mission Information Sheet

[5] CNES, Centre National d'Études Spatiales, *ExoMars Rover*

[http://smc.cnes.fr/EXOMARS/GP\\_rover.htm](http://smc.cnes.fr/EXOMARS/GP_rover.htm)

Last visited on: April 2010

[6] The MIMA Team – POLIMI, MIMA Environmental Conditions, *MIMA Thermomechanical Design documents* 2009

[7] Patrick L. Walter, Pyroshock Explained, *Technical Note PCB Piezotronics, Inc.*

[8] ENDEVCO 27A11 Product Data Sheet

[9] David J. Ewins - Modal Analysis And Modal Testing  
*Handbook of Noise and Vibration Control - Chapter 47, Wiley 2007*

[10] Peter Avitabile, Experimental Modal Analysis (A Simple Non-Mathematical Presentation), *University of Massachusetts Lowell*

[11] Kelly, S. Graham, Fundamentals of Mechanical Vibrations, 2nd ed.  
*McGraw-Hill 2000*

[12] Robert B. Randall, Noise and Vibration Data Analysis, *Handbook of Noise and Vibration Control - Chapter 46, Wiley 2007*

[13] Carlos A. Felippa, Advanced Finite Element Methods, *Aerospace Engineering Sciences - University of Colorado at Boulder, Spring 2009*

# Appendix A

## A.1 MATLAB scripts

### *1.3 The need for a damping system*

```
% Can Ozer
% The need for a damping system

% Parameters
f01 = 150; %[Hz]
f02 = 250; %[Hz]
w01 = 2*pi*f01;
w02 = 2*pi*f02;
xsi = 0.3;

f = 20:2000;
w = 2*pi*f;

H1 = (w01^2+j*2*w.*xsi*w01)./((w01^2-w.^2)+j*2*w.*xsi*w01);
G1 = abs(H1);
Phi1 = angle(H1)*180/pi;
H2 = (w02^2+j*2*w.*xsi*w02)./((w02^2-w.^2)+j*2*w.*xsi*w02);
G2 = abs(H2);
Phi2 = angle(H2)*180/pi;

% FRF squared
PSD1=G1.^2;
PSD2=G2.^2;

% Weighing profile
for i=20:500
    factor(i-19)=(20-1.7)/(500-20)*i+1.7-(20.17)/(500-20)*20;
end
for i=501:2000
    factor(i-19)=20;
end

% Weighed PSD
PSD_w1 = PSD1.*factor;
PSD_w2 = PSD2.*factor;

RMS_PSD1=norm(PSD1)/sqrt(length(PSD1))
RMS_PSD2=norm(PSD2)/sqrt(length(PSD2))
```

```

RMS_PSD_w1=norm(PSD_w1)/sqrt(length(PSD_w1))
RMS_PSD_w2=norm(PSD_w2)/sqrt(length(PSD_w2))

figure(1)
subplot(2,1,1)
plot(f,G1,f,G2);
title('FRF Magnitude');
xlabel('frequency [Hz]');
ylabel('Magnitude');
grid on
legend('System 1','System 2')
subplot(2,1,2)
plot(f,Phi1,f,Phi2);
title('FRF Phase');
xlabel('frequency [Hz]');
ylabel('Phase [deg]');
grid on
legend('System 1','System 2')

figure(2)
plot(f,factor);
title('Weighing Profile');
xlabel('frequency [Hz]');
ylabel('Factor');
grid on;

figure(3)
plot(f,PSD1,f,PSD2);
title('FRF^2 vs frequency');
xlabel('frequency [Hz]');
ylabel('PSD');
grid on;
legend('System 1','System 2')

figure(4)
plot(f,PSD_w1,f,PSD_w2);
title('Weighed FRF^2 vs frequency');
xlabel('frequency [Hz]');
ylabel('Weighed PSD');
grid on;
legend('System 1','System 2')

```

## Mathcad Scripts

### 4.3.1 Estimation of the Modal Parameters from the Experimental Data

$$j := \sqrt{-1}$$

$$m := 0.35 \quad [\text{kg}]$$

$$f_0 := 450 \quad [\text{Hz}]$$

$$\omega_0 := f_0 \cdot 2\pi = 2.827 \times 10^3 \quad [\text{rad/s}]$$

$$k := \omega_0^2 \cdot m = 2.798 \times 10^6 \quad [\text{N/m}]$$

$$\zeta := 0.4$$

$$H(\omega) := \frac{\omega_0^2 + j \cdot 2 \cdot \omega \cdot \zeta \cdot \omega_0}{(\omega_0^2 - \omega^2) + j \cdot 2 \cdot \omega \cdot \zeta \cdot \omega_0}$$

$$G(\omega) := |H(\omega)|$$

$$\phi(\omega) := \arg(H(\omega)) \cdot \frac{180}{\pi}$$

f\_data :=

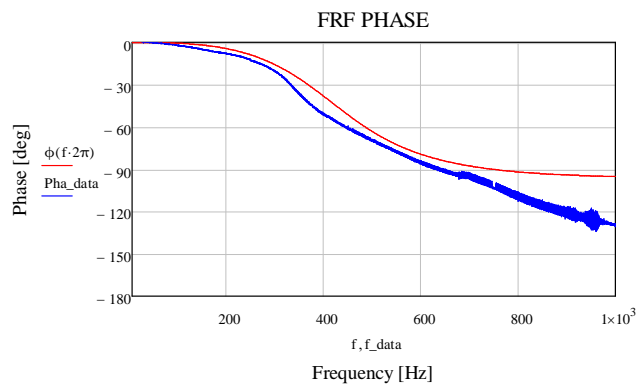
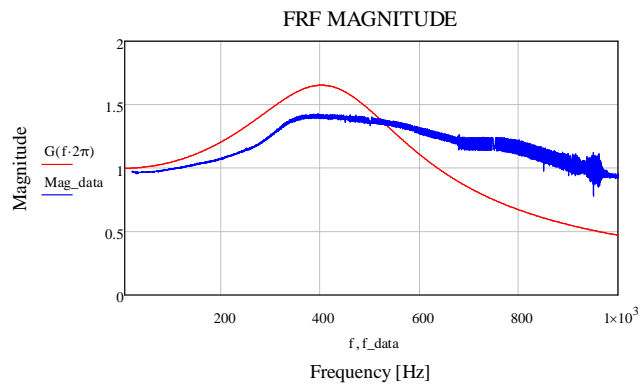
	0
0	20.009
1	20.083
2	20.157
3	20.231
4	20.305
5	20.379
6	20.454
7	20.528
8	20.602
9	20.676
10	20.75
11	20.824
12	20.898
13	20.972
14	21.046
15	...

Mag\_data :=

	0
0	0.976
1	0.975
2	0.975
3	0.974
4	0.973
5	0.975
6	0.977
7	0.978
8	0.978
9	0.978
10	0.977
11	0.976
12	0.975
13	0.975
14	0.974
15	...

Pha\_data :=

	0
0	1.201
1	1.021
2	1.029
3	1.199
4	1.189
5	1.136
6	1.22
7	1.244
8	1.135
9	1.049
10	1.004
11	0.97
12	0.951
13	0.943
14	0.954
15	...



### 4.3.2 Estimation of the Modal Parameters by Curve Fitting

$$j := \sqrt{-1}$$

$$m := 0.35$$

From FRF calculated using test data:

$$f_1 := 100 \quad [\text{Hz}]$$

$$\text{Mag}_1 := 1.9$$

$$\text{Pha}_1 := -50 \quad [\text{deg}]$$

$$\omega_1 := f_1 \cdot 2\pi = 628.319 \quad [\text{rad/s}]$$

Initial guess:

$$f_0 := 150 \quad [\text{Hz}]$$

$$\zeta := 0.3$$

$$\omega_0 := f_0 \cdot 2\pi = 942.478$$

Solving the mathematical model:

Given

$$\left| \frac{\omega_0^2 + j \cdot 2 \cdot \omega_1 \cdot \zeta \cdot \omega_0}{(\omega_0^2 - \omega_1^2) + j \cdot 2 \cdot \omega_1 \cdot \zeta \cdot \omega_0} \right| = \text{Mag}_1$$

$$\arg \left[ \frac{\omega_0^2 + j \cdot 2 \cdot \omega_1 \cdot \zeta \cdot \omega_0}{(\omega_0^2 - \omega_1^2) + j \cdot 2 \cdot \omega_1 \cdot \zeta \cdot \omega_0} \right] \cdot \frac{180}{\pi} = \text{Pha}_1$$

$$\begin{pmatrix} \omega_0 \\ \zeta \end{pmatrix} := \text{Find}(\omega_0, \zeta) = \begin{pmatrix} 659.615 \\ 0.32 \end{pmatrix}$$

### Getting the modal parameters

$$\omega_0 = 659.615$$

$$\zeta = 0.32$$

$$f_0 := \frac{\omega_0}{2\pi} = 104.981$$

$$k := \omega_0^2 \cdot m = 1.523 \times 10^5$$

### Mathematical Model:

$$H(\omega) := \frac{\omega_0^2 + j \cdot 2 \cdot \omega \cdot \zeta \cdot \omega_0}{(\omega_0^2 - \omega^2) + j \cdot 2 \cdot \omega \cdot \zeta \cdot \omega_0}$$

$$G(\omega) := |H(\omega)|$$

$$\phi(\omega) := \arg(H(\omega)) \cdot \frac{180}{\pi}$$

### Maximum Deviation

$$\text{max\_dev} := \max (\text{Pha\_data} - \phi(f\_data \cdot 2\pi)) = 3.253$$

$$\text{maxdev\_pha} := \max \left[ \left| (\text{Pha\_data} - \phi(f\_data \cdot 2\pi)) \right| \right] = 11.649$$

f\_data :=

	0
0	20.008
1	20.057
2	20.107
3	20.157
4	20.207
5	20.256
6	20.306
7	20.356
8	20.406
9	20.455
10	20.505
11	20.555
12	20.605
13	20.655
14	20.704
15	...

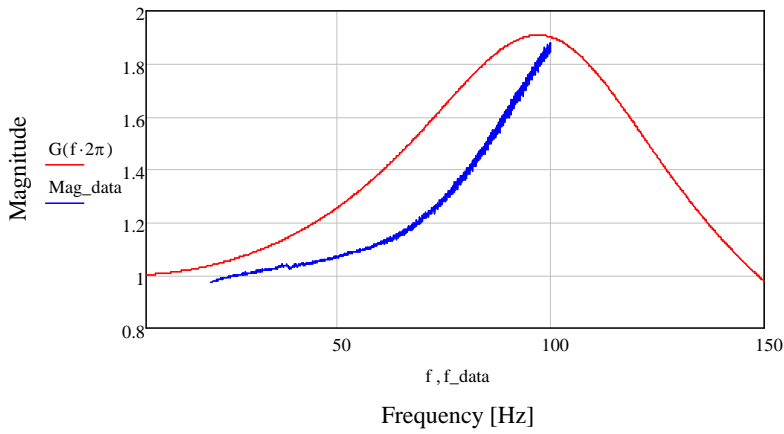
Mag\_data :=

	0
0	0.975
1	0.974
2	0.973
3	0.974
4	0.974
5	0.975
6	0.973
7	0.975
8	0.975
9	0.976
10	0.975
11	0.976
12	0.976
13	0.977
14	0.977
15	...

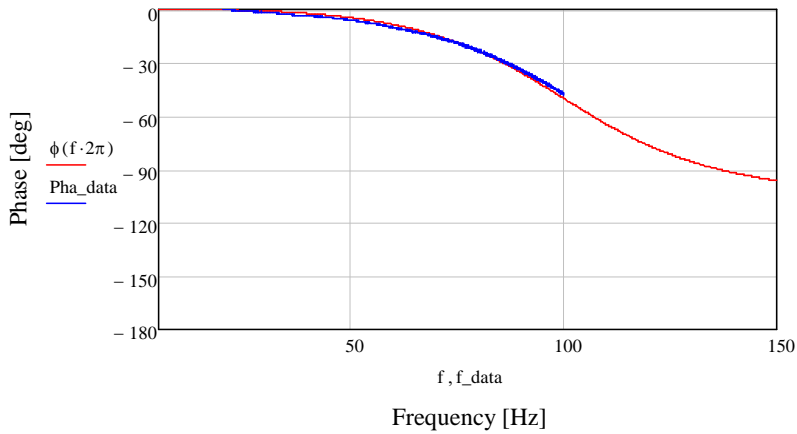
Pha\_data :=

	0
0	0.033
1	0.017
2	-2.08·10 <sup>-3</sup>
3	-0.043
4	-0.067
5	-0.235
6	-0.052
7	-0.174
8	-0.182
9	-0.184
10	-0.117
11	-0.098
12	-0.13
13	-0.129
14	-0.119
15	...

FRF MAGNITUDE



FRF PHASE



# Appendix B

## Further Dummy Testing Plots

### B.1 Z axis sweep

The out-of-plane vibrations given as time history and FRFs

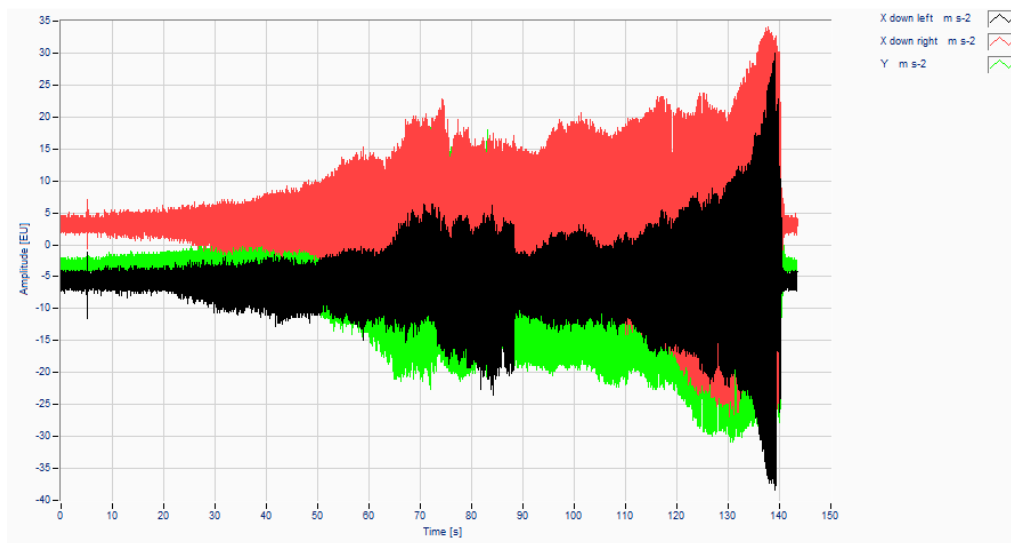


Figure B-106: Time history of out-of-plane vibrations for the Z sweep sine testing

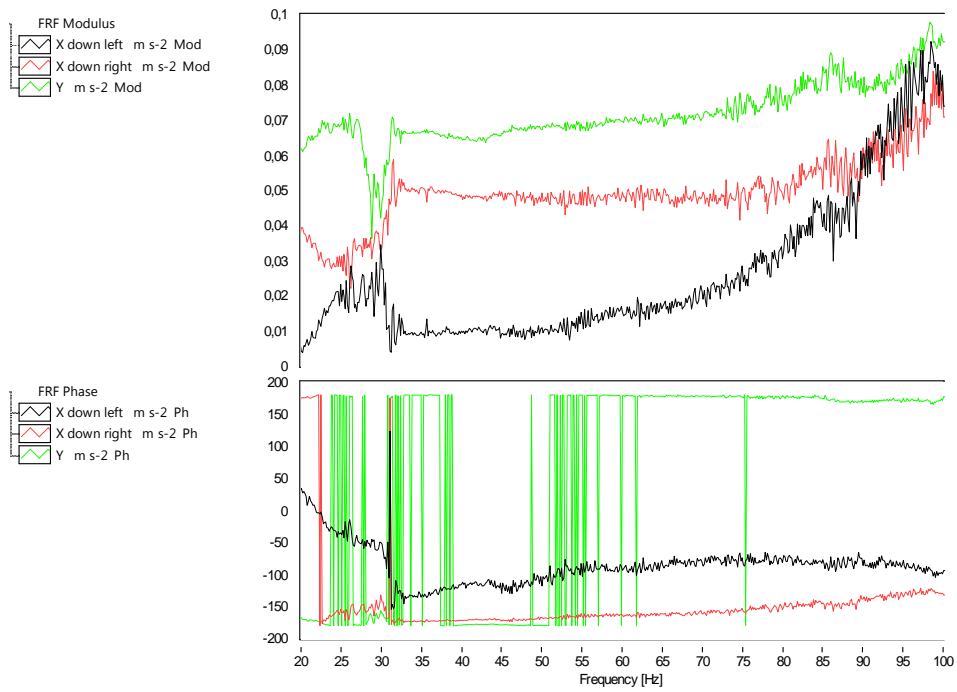


Figure B-107: FRF of out-of-plane vibrations for the Z sweep sine testing

## B.2 Z axis random

The out-of-plane vibrations for the random testing in Z are as follows

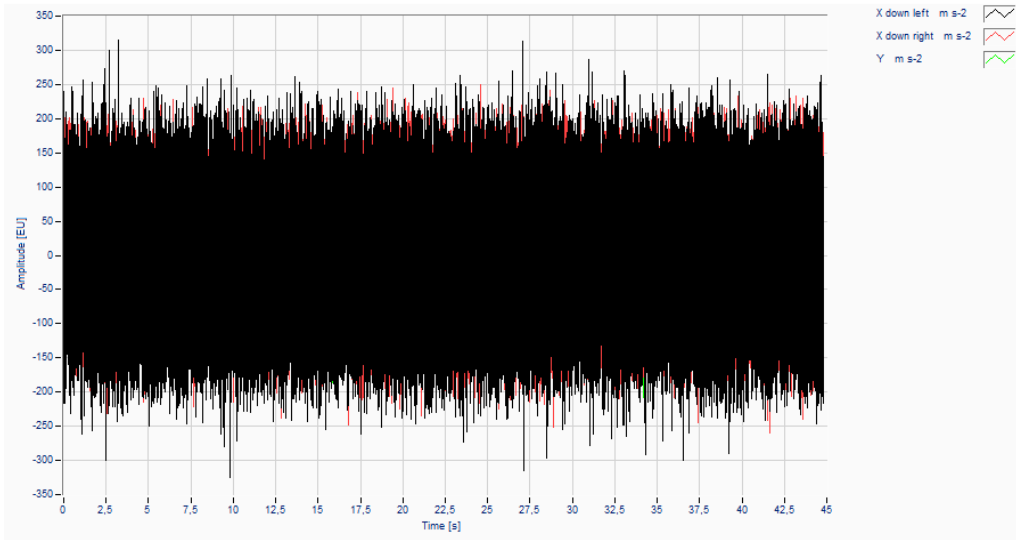


Figure B-108: Time history of out-of-plane vibrations for the Z random testing

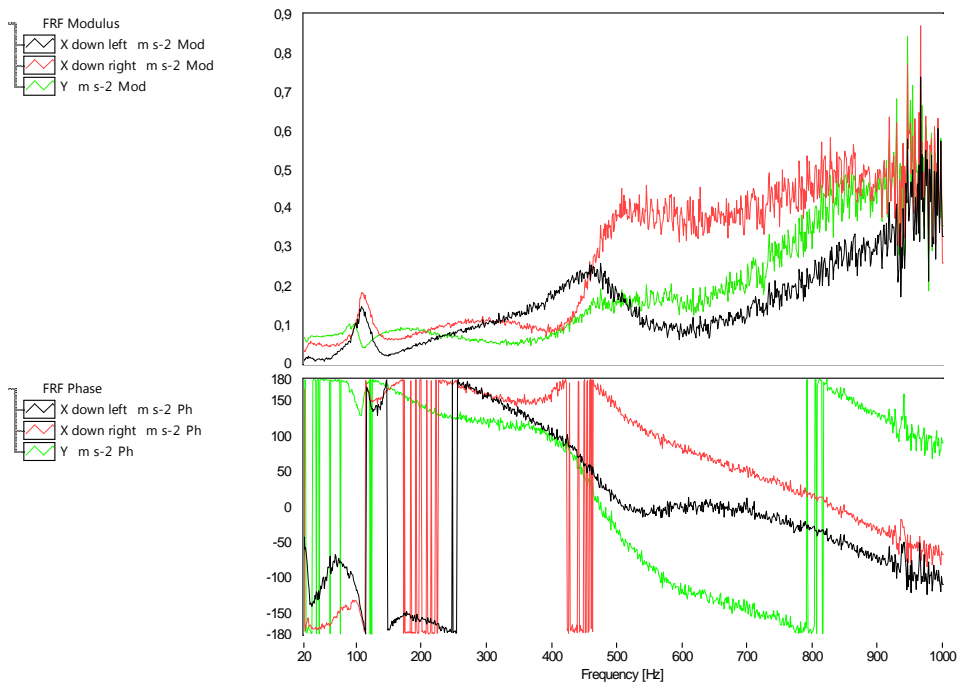


Figure B-109: Time history of out-of-plane vibrations for the Z random testing